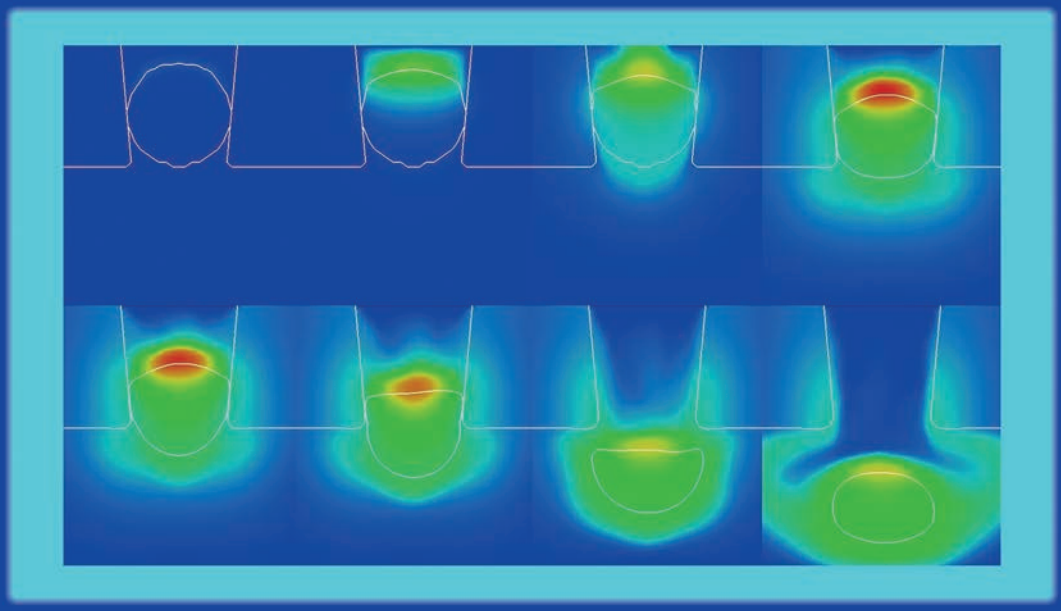

FAU Studien aus dem Maschinenbau 388

Stefan Stein

Laser drop on demand joining as bonding method for electronics assembly and packaging with high thermal requirements

FAU University Press

Stefan Stein

Laser drop on demand joining as bonding method for electronics assembly and packaging with high thermal requirements

FAU Studien aus dem Maschinenbau

Band 388

Herausgeber der Reihe:

Prof. Dr.-Ing. Jörg Franke
Prof. Dr.-Ing. Nico Hanenkamp
Prof. Dr.-Ing. habil. Tino Hausotte
Prof. Dr.-Ing. habil. Marion Merklein
Prof. Dr.-Ing. Michael Schmidt
Prof. Dr.-Ing. Sandro Wartzack

Stefan Stein

Laser drop on demand joining as bonding method for electronics assembly and packaging with high thermal requirements

Dissertation aus dem Lehrstuhl für Photonische Technologien (LPT)

Prof. Dr.-Ing. Michael Schmidt

Erlangen
FAU University Press
2022

Bibliografische Information der Deutschen Nationalbibliothek:
Die Deutsche Nationalbibliothek verzeichnet diese Publikation in der Deutschen Nationalbibliografie; detaillierte bibliografische Daten sind im Internet über http://dnb.d-nb.de abrufbar.

Autoren-Kontaktinformation:
Stefan Stein, Lehrstuhl für Photonische Technologien,
ORCID: https://orcid.org/0000-0002-8389-3267

Bitte zitieren als
Stein, Stefan. 2022. *Laser drop on demand joining as bonding method for electronics assembly and packaging with high thermal requirements.* FAU Studien aus dem Maschinenbau Band 388. Erlangen: FAU University Press.
DOI: 10.25593/978-3-96147-508-7

Der vollständige Inhalt des Buchs ist als PDF über den OPUS-Server der Friedrich-Alexander-Universität Erlangen-Nürnberg abrufbar:
https://opus4.kobv.de/opus4-fau/home

Verlag und Auslieferung:
FAU University Press, Universitätsstraße 4, 91054 Erlangen

Druck: docupoint GmbH

ISBN: 978-3-96147-507-0 (Druckausgabe)
eISBN: 978-3-96147-508-7 (Online-Ausgabe)
ISSN: 2625-9974
DOI: 10.25593/978-3-96147-508-7

Laser drop on demand joining as bonding method for electronics assembly and packaging with high thermal requirements

Der Technischen Fakultät
der Friedrich-Alexander-Universität
Erlangen-Nürnberg

zur
Erlangung des Doktorgrades Dr.-Ing.

vorgelegt von

Stefan Stein, M.Sc.

aus Würzburg

Als Dissertation genehmigt
von der Technischen Fakultät
der Friedrich-Alexander-Universität Erlangen-Nürnberg

Tag der mündlichen
Prüfung: 8.11.2021

Gutachter: Prof. Dr.-Ing. Michael Schmidt
Prof. Dr.-Ing. Welf-Guntram Drossel, TU Chemnitz

Preface

During the last several years at the Bayerisches Laserzentrum, I worked intensively on the development of a joining process, which can combine the advantages of soldering with those of wire bonding. A thorough investigation of this topic required a holistic approach to process development. Fundamental knowledge of optics and laser technology as well as electrical engineering, computer science, physics and system development were necessary. In order to be able to develop such a broad knowledge base, a creative environment is a prerequisite to allow a high degree of self-responsibility and also to support the constant exchange of knowledge with colleagues.

Thus, I want to thank both, the manager of the Bayerisches Laserzentrum, Dr.-Ing. Stephan Roth, as well as the professor of the Chair for Photonic Technologies Prof. Dr.-Ing. Michael Schmidt for providing such an environment. Further, I would like to emphasise the support from and fruitful discussions with Michael Dobler and Johannes Heberle of the Chair for Photonic Technologies. I would also like to thank Tim Radel from the Bremer Institut für angewandte Strahltechnik for his help in determining the wetting angle of a liquid medium at a temperature of 1000°C. In addition, closely collaborating with the Process Technology Metals group at the blz was highly productive and laid the foundations for my successful work. A substantial part of the present work is experimental. These experiments would not have been possible without the support of the technical staff, especially Benjamin Steffan and Udo Müller. Without the active support of many student and academic assistants, as well as numerous studies and diplomas, masters' and bachelors' theses, the success of this work would not have been possible.

Since some of the presented investigation involved interdisciplinary collaboration, the author would like to thank the Fraunhofer Institute for Ceramic Technologies and Systems IKTS, in particular Dr. Sylvia Gebhardt and Sebastian Rhein, as well as the Chair of Materials Science and Engineering for Metals at the University Erlangen, namely Prof. Dr. Carolin Körner and Jonathan Wedler. Furthermore, I want to emphasise my gratitude towards the Deutsche Forschungsgemeinschaft (DFG) for founding substantial parts of this work in the context of the Collaborative Research Centre/Transregio 39 PT-PIESA, subproject A04. Finally, I want to thank my family, especially my wife, who supported me with words and deeds during this undertaking. Without her, this document would not exist.

Table of Contents

List of Symbols and Abbreviations

Symbol	Unit	Description
σ		standard deviation
σ_{ST}	$N\ m^{-1}$	surface tension
$\varnothing$	m	diameter
∇	-	gradient
A	m^2	area
A_{el}	%	elongation at break
A_F	m^2	horizontal contact surface
$A_{Failure}$		area of fracture
Ag		silver
Al_2O_3		aluminium oxide
AlN		aluminium nitride
Aq	m^2	cross sectional area
A_{sl}	m^2	solid-liquid contact surface
B_2O_3		boron trioxide
CAD		computer aided design
CaO		calcium oxide
CCD		charge coupled device
c_d	-	drag coefficient
c_p	$J\ kg^{-1}\ K^{-1}$	specific heat capacity
Cu		copper
EPA		electronics packaging and -assembly
E_{pulse}	J	pulse energy
ETP		electrolytic-tough-pitch
f	Hz	frequency
F	N	force
f_{foc}	m	focal length
F_{Max}		maximum force at failure
$FPGA$		field programmable gate array
FPS	Hz	frames per second
FSS		full scale span

H_{melt}	*J*	enthalpy of fusion
HTCC		high temperature cofired ceramics
k	-	extinction coefficient
L	*J*	latent heat
l	*m*	length
LDJ		laser droplet joining
LPM		LTCC Piezo Module
LTCC		low temperature cofired ceramics
m	*kg*	mass
M^2		beam quality factor
MgO		magnesium oxide
Nd:YAG		neodymium-doped yttrium aluminium garnet
n_{Frames}		number of frames
PbO		lead (II) oxide
P_L	*W*	optical output power
P_{max}	*W*	maximum optical output power
PO2	*Pa*	partial oxygen pressure
P_{Pulse}	*W*	pulse power
p	*Pa*	pressure
PZT		lead zirconate titanate
R^2		coefficient of determination
Ra	*m*	arithmetic average roughness of a profile
Rz	*m*	average maximum peak to valley roughness
SAC-solder		tin-silver-copper solder
Si_3N_4		silicon nitride
SiO_2		silicon dioxide; silica
SrO		strontium oxide
STEP		standard for the exchange of product model data
T	*K*	temperature
t	*s*	time
TiO_2		titanium dioxide

T_{liquid}	K	liquidus temperature
t_{Pulse}	ms	pulse duration
T_R	K	room temperature (293 K)
T_{solid}	K	solidus temperature
T_{vapor}	K	evaporation temperature
USP		ultra-short pulse
V	m^3	volume
V_{ac}		acceleration voltage
$v_{droplet}$	$m\ s^{-1}$	droplet velocity
V_{Ps}	V	output voltage pressure sensor
w(z)	m	Gaussian beam waist radius
w_o	m	collimated beam waist diameter
WC/Co		tungsten carbide cobalt
w_f	m	minimum beam waist radius in focus
x_o		Cartesian coordinate system origin in x-direction
y_o		Cartesian coordinate system origin in y-direction
$Yt:YAG$		ytterbium: yttrium aluminium garnet
z_o		Cartesian coordinate system origin in z-direction
z_R	m	Rayleigh range
α		absorptance
α_{Exp}	K^{-1}	coefficient of linear thermal expansion
γ	$N\ m^{-1}$	surface tension
γ_{Kin}	$m^2\ s^{-1}$	kinematic viscosity
γ_{lg}	$N\ m^{-1}$	surface tension liquid-gas interface
γ_{sg}	$N\ m^{-1}$	surface tension solid-state gas interface
γ_{sl}	$N\ m^{-1}$	surface tension solid-liquid interface
ΔH_f	$J\ g^{-1}$	enthalpy of fusion
ΔH_s	$J\ g^{-1}$	heat of solidification
θ	°	wetting angle
λ	m	wavelength

λ_{therm}	$J\ g^{-1}K^{-1}$	specific thermal conductivity
ρ_{dens}	$kg\ m^{-2}$	density
σ		standard deviation
σ_{el}	$S\ m^{-1}$	electrical conductivity
τ_{Shear}		shear strength

1 Introduction

Social development, particularly in industrialised countries, is characterised by climate change and resource depletion. A significant contribution to securing sustainability and mobility as well as competitive energy supply approaches can be provided by the development of innovative, cost- and energy efficient production processes. This resulted in production research being focused on the challenges of a resource- [1] and energy-efficient [2] production. The required solutions need to enable minimal consumption of resources and energy throughout the product production process and lifecycle.

A major priority for high-performance components in the fields of mechanical engineering and transport technology is lightweight construction [3; 4], which is increasingly being emphasised due to the stringent laws regarding environmental protection. As a result, lightweight construction is currently regarded as an unconditional necessity and priority in the field of vehicle construction [3; 5], e-mobility [6], aviation [7] and other applications [8]. In addition, lightweight construction can also be a key approach to achieve performance improvements of the final product, since a reduction, e.g. in vehicle weight, enables an improvement in dynamics and a reduction in fuel consumption. However, a requirement for light, stiff, secure and reliable components, while maintaining a high level of comfort in the passenger compartment, inevitably leads to a target conflict in component design [9].

Currently, these conflicts are not completely solvable by elaborate conception, production and testing of lightweight constructions, since lightweight construction must still be viewed as a compromise of optimal properties and minimum component weight as indicated by [3] and [7]. The integration of sensors, actuators and piezoelectric generators into the load path of such a passive lightweight structure creates an active structural component with unique properties.

An example of this is Active Noise Control [10], which is an approach to counteract the increase in the structural stiffness and thus acoustic emissions of vibrating structural components. These vibrations can be suppressed by the application of active vibration dampening. In addition, the application areas of such smart structures are not restricted to noise control. Another field of application is condition also known as structural health monitoring, which particularly gains relevance in the aerospace

sector [11]. One further area of application of smart structures is the construction of networks enabling the recovery of energy from vibrating structural components [8]. By integrating sensor-actuator modules directly into structural components during their manufacturing process the placement of the actuator module precisely at the final structures' load path enables to obtain the highest yield for the desired application. Thus, enabling the integration of sensor-actuator modules during the manufacturing process of the load bearing structure is the ultimate goal of all of the following investigations.

2 State of the art and methods

In the past years, extensive investigations were carried out on the integration of piezoelectric sensors into structural components as shown in [12]. A particularly interesting and promising approach was the integration of piezoceramic modules into casted aluminium components, which has been investigated in [13]. In addition, the integration of active elements into fibre-reinforced plastic (FRP) components is of interest due to the high lightweight potential of FRP-structures. Figure 1 shows two possible approaches of embedding piezo-active modules into lightweight structures by aluminium die casting (left) and laminating piezo modules into FRP structural components (right).

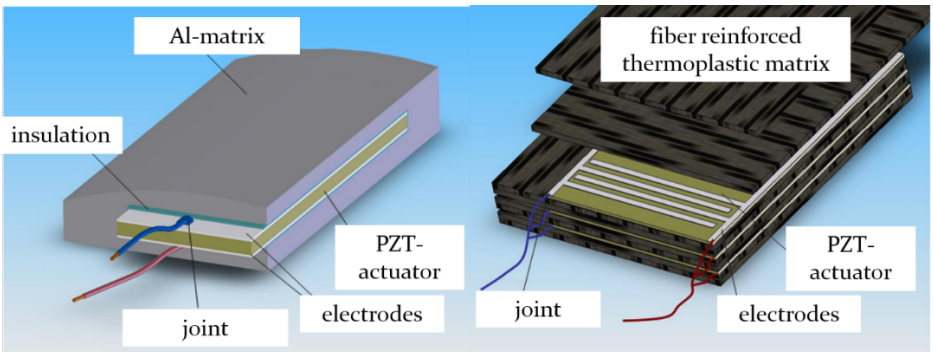

Fig. 1: Schematics of the approaches for the integration of piezo actuators in Al castings and fibre-composite structures (based on [14])

The motivation to develop a process suitable to join copper wires to electrode structures of piezo actuators arises from two main downstream integration processes. These processes are Al die casting and hot pressing and will be described in the following section. These processes define the thermal and mechanical load collectives, and thus requirements that the joints between the module's electrode structure and the wire need to fulfil. The integration of such piezoceramic transducers into load bearing structures is currently limited by the fact that the whole actuator needs to withstand the mechanical and thermal loads that occur during the integration processes.

Thus, in order to show the feasibility of integrating sensors and actuators at any desired position of the lightweight structure, several tailored processes need to be developed. Additionally, since these processes must be fused into a process chain, they extend far beyond the current state of the art. In this work, the challenge of providing a suitable joining method of

the piezo module's electrode structure and the wire is addressed. A particular emphasis was put on taking the prevailing boundary condition, namely the electrode material and thickness, as well as the wire thickness into account, since the electrode exhibits a thickness of just 20 µm and consists of sintered Ag paste. The Cu wire to be joined to the electrode has a thickness of between 100 and 200 µm, thus both joining partners not only have very low thicknesses with respect to their diameters, but are also made from elements which are challenging to join with conventional processes, e.g. welding.

2.1 Al die casting

In order for the joining process to generate joints able to withstand a downstream integration of the piezo in casted Al structures, it is first necessary to investigate all manufacturing steps from the manufacturing of the piezo module until its integration into the Al casting to derive the necessary properties of a suitable joint. This in turn will define a suitable joining approach to be pursued. Particularly, the significant temperatures occurring during the Al casting process pose a challenge for both the piezo module itself as well as for the joining interface between the module's electrode structure and the conductive wire. To achieve such a high thermal stability of the piezo module, a low temperature cofired ceramic (LTCC)-based module was designed as shown by [15]. This piezo module will be referred to as an LPM. The LPM structure is shown as an explosion image in figure 2.

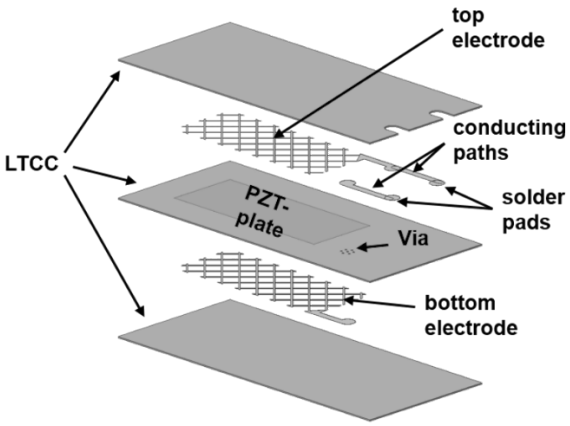

Fig. 2: Schematic layout of an LPM (enhanced explosion image) [24]

Due to its dielectric LTCC matrix, the LPM exhibits a significantly higher thermal stability than standard polymer based piezo modules [15]. Low temperature cofired ceramics are composed of glass frits of SiO_2, CaO, B_2O_3, MgO, SrO, TiO_2 and PbO [16]. The individual ceramic particles are embedded in an organic bonding agent, by which the viscosity of the resulting green body can be adjusted. Details regarding the composition of the discrete components of the piezo module can be found in [17–19; 15; 20–22] and [23]. Firing is carried out to remove the organic constituents of the green body, which would otherwise decompose and evaporate during the casting process.

LTCC was chosen as the ceramic carrier material because it allows 3D wiring. In addition, it is expected to show good chemical adhesion to the aluminium melt due to its aluminosilicate content which shows metallurgical compatibility with the Al melt [16]. Therefore, a pre-sintered piezoceramic plate based on a PZT formulation (CeramTec, Sonox® P53) was metallised on both sides by screen-printed silver electrodes (DuPont 6160) and cut to a size of 26 mm x 10 mm x 0.2 mm. A detailed description of the fabrication process can be found in [15]. The grid-like electrode structure is screen-printed using the Ag conductor paste Heraeus TC0307, whereas the vias are filled with the Ag conductor paste Heraeus TC0308. This enables the inner wiring of the LPM and thus the application of electric fields to the piezoceramic plate, necessary to exploit the piezoelectric effect of the module. For outer contacts, 20 µm thick contact pads were screen-printed using the Ag conductor paste Heraeus TC0306. The thickness of those Ag interfaces is 20 µm.

Casting is carried out using the aluminium casting alloy 226 D (AlSi9Cu3Fe) with a solidus temperature of $T_{Solidus}$ = 521°C and a liquidus temperature of $T_{Liquidus}$ of 593°C [25]. This alloy has been chosen due to its good pouring properties [26]. According to [25], a plunger velocity of 4.5 m/s, results in a form filling speed with a maximum flow rate of 25.7 m/s. However, simulations carried out at the Chair of Materials Science and Engineering for Metals in Erlangen indicated that the flow velocities could reach up to 100 m/s. Considering the density of the aluminium melt of 2.4 g/cm³, the drag force of the melt acting on the solder pads can be estimated using equation 1:

$$F_d = \frac{1}{2}\rho v^2 c_d A \qquad (1)\ [25]$$

In which F_d is the drag force which is acting in the direction of the flow velocity. ρ is the mass density of the fluid and v is the flow velocity of the Al melt relative to the joining area. In addition, A is the reference area, which is typically defined as the area of the orthographic projection of the object on a plane perpendicular to the direction of the fluids' respective melt flows motion; c_d represents the drag coefficient [27]. Assuming the worst-case scenario of a melt flow velocity of 100 m/s and an exposed area of 1 mm² for the joint, the force acting on the joint is 6 N, meaning that on a joining area of 1 mm², a pressure of 6 MPa is applied. A 100% safety margin thus would require a mechanical strength of the joints of 12 MPa against the shear forces, to withstand the Al casting process.

This value thus represents one of the major requirements that a suitable joint must be able to achieve. The corresponding joining process must be developed in a way to fulfil this requirement. Further requirements on the joining process can be derived by the second integration process of piezo modules into lightweight structures, the hot-pressing process.

2.2 Hot-pressing process

Due to the increasingly widespread use of fibre reinforced plastic (FRP) components in automotive and aerospace industries [28], it is expedient to design a joining process which enables integration of active modules in FRP systems. The requirements on the joints during the manufacturing of active FRP structures is different, but equally demanding. Currently, the application of transducers is carried out by attaching them to the structural component by a gluing process [29]. Using this approach, the ductility of the adhesive layer decreases the efficiency of the transducer. To be able to integrate the piezo actuator directly into the matrix of the structural component, thermoplastic-compatible piezo modules (TPMs) were developed, in which the piezo-active element is laminated into a thermoplastic carrier film. This film consists of the same polymer as the matrix of the FRP structure [29–31; 28]. The material-homogenous integration of the piezoceramic modules into the fibre-reinforced composite structures, based on thermoplastic matrices, is carried out by an adapted hot-pressing process, which was conceptualised by Hufenbach [31]. During this process, the thermoplastic matrix material of the structural FRP-component is consolidated with the TPM's carrier film. Figure 3 shows the conceptual manufacturing process of fibre-reinforced thermoplastic composites as proposed by [29].

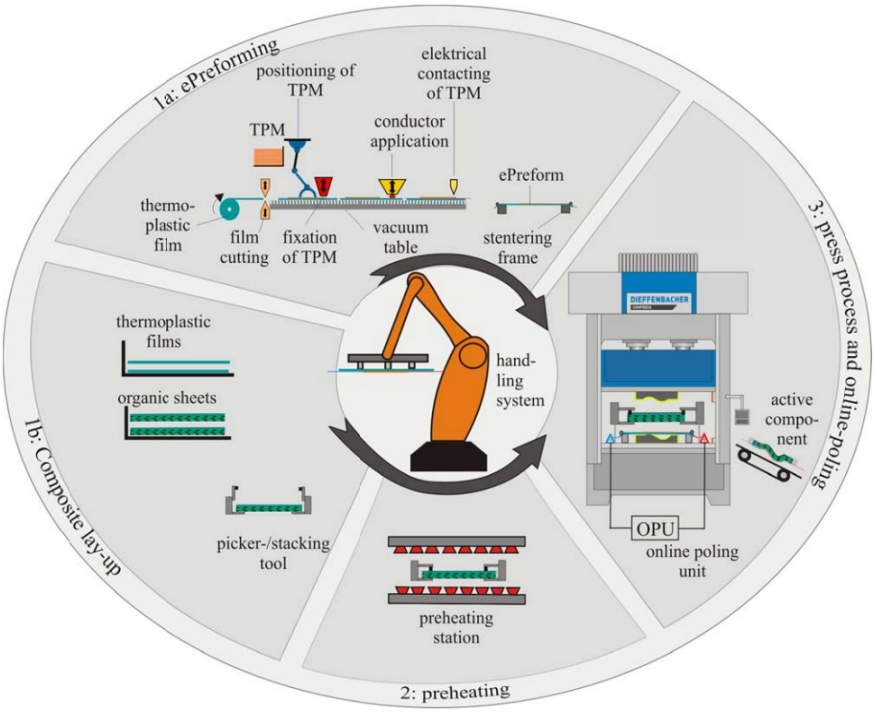

Fig. 3: The manufacturing process for active fibre-reinforced thermoplastic composites according to [29]

The process for a material-homogeneous integration of TPM in composite structures with thermoplastic matrices is shown in figure 3, and consists of four sub-processes. First, a thermoplastic film is equipped with a TPM and subsequently joined with Cu wires to generate a functionalised interface, referred to as ePreform (figure 3 sub-process la) [29]. Then the ePreform is transferred into the pressing die. The composite lay-up of the structural component is generated by stacking organic sheets and additional thermoplastic films into a frame (figure 3 sub-process lb). This is then transferred to the infrared-heating station, preheated over the glass transition temperature (see figure 3 sub-process 2), and finally transferred into the pressing die. The press closes and the ePreform forms a material-to-material bond with the thermoplastic matrix of the structural component [29]. Consolidation is carried out by applying forces of 5 kN and temperatures up to 240°C. This translates to a pressure of 0.05 MPa for the tool geometry used [32]. The dwell time is 10 minutes.

The result is a firm bond between the matrix material of the FRP structure and the TPM's carrier film [32]. Both the thermal and mechanical load must be endured by the electrical joint during consolidation of the structure.

Again, these requirements form hard boundary conditions which a joint must be able to fulfil.

2.3 Synopsis

To ensure the highest yield of the adaptronic system, it is necessary to introduce the piezo actuator directly into the flux of forces of the structural component. A suitable electrical joining method thus must fulfil the requirements of thermal and mechanical stability during subsequent integration processes. If the joint between an electrode and a wire is to withstand the Al die casting process, the joining interface cannot deteriorate at temperatures of up to 593°C, and a shear strength of higher than 12 MPa must be endured. This must be achieved by exploiting a 20 µm thick Ag-electrode structure as joining interface. In addition, the integration of piezo modules in a hot-pressing process exposes the joints to 240°C at a pressure of 0.05 MPa, both of which need to be withstood by the joint for ten minutes [29]. These demands are challenging for conventional joining methods.

It must also be stated that there are several topics covered within the scope of this thesis that must be considered state of the art. Those topics include some basics about Gaussian beam propagation, determination and interpretation of wetting angles and joint shear strengths, as well as some basic procedures in the fields of image processing and fluid dynamics simulation. However, in order to not impair the flow of reading, these basics are briefly introduced in the respective chapters and original sources are quoted respectively.

2.4 Conventional joining methods in electronics packaging

To assess the mentioned requirements, it is necessary to evaluate the predominant methods currently used in electronics packaging and assembly (EPA) technology. The predominant connection processes in electronics packaging are:

- Soldering
- Micro welding
- Wire bonding
- Generation of electrically conductive droplets

In the following section, the abovementioned joining methods are evaluated regarding the requirements arising due to the integration processes described in sections 2.1 and 2.2.

2.4.1 Soldering

The most common method for producing electrical joints between a conductor and a device electrode, is soldering. In the past, various processes such as vapour phase soldering, furnace soldering, wave soldering or laser beam soldering have been established in academia and industry [33]. The solder can hereby be provided in liquid form (wave soldering) or in solid form, for instance as solder wire or solder preform as well as a paste which can be applied by dispensing or screen printing. Due to its high relevance for the electronics industry, soldering was subject to a large number of investigations in recent years. The main focus has been on the development and qualification of lead-free solder alloys, which was required by the restriction of hazardous substances (ROHS) directive, passed in 2013 [34]. However, due to the low solidus and liquidus temperatures of conventional lead-free electronic solder alloys, as well as their tendency to creep at elevated temperatures of 190°C and above, soldering was discarded as a joining method, since it does not fulfil the requirements, as described in chapter 2.

2.4.2 Micro welding

Another process, which has been under investigation for several years in electronics packaging and assembly, is laser micro welding [35]. Due to the joint geometry, the application of a welding process is problematic for the described task. The joining geometry consists of a wire with a diameter of 200 µm which must be joined to an electrode structure represented by a screen-printed Ag metallisation of 10–20 µm thickness. This joint geometry is particularly unfavourable for a welding process since the upper joining partner's thickness is about ten times the thickness of the lower joining partner, which results in a perforation of the Ag electrode and thus delamination of the contact pad and cracking of the piezoceramic substrate [14].

2.4.3 Wire bonding

Wire bonding is a method of generating interconnections between integrated circuits (ICs) or other semiconductor devices and the next higher wiring level, usually represented by the printed circuit board (PCB). Wire bonding was established as one of the dominant joining processes in electronics packaging and is used nowadays in a clear majority of semiconductor packages. The process has maintained its leading position amongst electronics packaging processes for over 30 years [36; 37]. The fundamental mechanism of wire bonding is the material bonding of two joining partners by applying a constant force acting vertically and a superimposed periodic

lateral force. These forces are applied using a sonotrode which is excited by a piezo-active transducer.

The principle of the bonding mechanism is the generation of a metallurgical compound in the joining area, which categorises the process as a type of friction welding. Such joining processes are also referred to as cold press welding [36]. Deficiencies of the wire bonding process arise from the necessity to introduce mechanical forces into the joining partners. For instance, forces of 10 to 30 N are required if wire bonding is to be used for wire thicknesses between 300 - 500 µm. The mechanical forces necessary to guarantee a robust bonding process can be applied only if the joining partners are clamped mechanically and show sufficient bending stiffness. As a result, thin films or foils, as well as ceramic sheets, are unfavourable substrates for a wire bonding process, since they don´t provide a sufficiently high mechanical strength.

2.4.4 Generation of electrically conductive droplets

As a supplement to the above-mentioned standard joining methods, several special purpose processes have been developed in recent years. These address different challenges in electronics packaging and assembly. Those joining processes must also be considered to thoroughly describe the state of the art. For example, the "Solder Ball Jetting" or "Solder Ball Bumping" method is commercially available and in use, e.g. for detaching solder balls to ball grid arrays. However, this process can also be utilised to solve other problems posed by electronics packaging (see [38–40] and [41]). Since the system is commercially available [42; 43], the process has been subject to profound research and is used as an assembly technique for optics, e.g. in aerospace applications [44; 40; 45]. Furthermore, due to the local and indirect energy input into the joining area, thermal distortions can be ignored, which makes the process suitable as a joining process for high-precision optics [46]. However, since standard tin-based electronic solders are used in solder ball jetting, the joints would not be able to withstand the thermal loads occurring during Al die casting or hot pressing.

Other methods have also been developed and utilised in the past to selectively deposit conductive material to different substrates, to create electrical or mechanical joints. For example, electromagnetic methods have been proposed to generate and deposit solder droplets [47; 48], or to detach ferrofluid droplets via a coil gun [49]. However, those approaches are not suitable as a joining method for piezo actuators which are to be integrated into

structural components via aluminium die casting or hot pressing due to the low liquidus temperature of the investigated filler materials.

Also, various piezoelectric printing heads are described in the literature to detach solder droplets, but, due to the loss of the piezoelectric effect when the printing head's Curie temperature is exceeded, such devices are currently not used to generate braze droplets with liquidus temperatures above 800°C. The main application of piezo-based print heads is the application of solder or dispensing of conductive inks [50; 51] or gallium [52].

Another approach to generate metal droplets is the melting of a wire tip and a droplet detachment by applying a mechanical movement of the molten wire tip [53]. Several different technologies have been used to generate droplets from metal wires, of which applying laser radiation is the most dominant. In the past, setups comprising of two laser beams [14], three beams as shown in [54] and [55], or annular foci as shown in [56] were proposed. The twin-beam setup utilised a 1 mm wire of Cu75AgP-645 with a melting point of T_m = 645°C for droplet generation [14]. The shear strength of the generated joints ranged between 35 – 42 N/mm², however, the contact angle of the droplet on the electrode surface, as well as the dispatched braze volume and its lateral position on the electrode structure varied significantly. In addition, the process induced cracks into the ceramic substrate. Due to these process-inherent flaws, the approach of generating droplets from wires was discarded for further investigations.

3 Objectives

As described in the requirements formulated in chapter 2, the integration of piezo actuators into Al or FRP structures, place high demands on any potential joining process. In summary, a suitable process for high volume application must fulfil the following requirements:

Casting:

- High thermal stability of the joints above $T_{Liquidus}$ of 593°C for the casting alloy 226D [25].
- Endurance of a shear force of 12 MPa as induced by the Al melt during casting.

Hot pressing:

- Contact needs to be free to be able to join 20 µm foils.
- Joint must endure a tool temperature of 240°C which is applied for ten minutes at a perpendicular pressure of 0.05 MPa.

In addition, there are further requirements to be fulfilled for a process to be suitable for high volume production:

- Cycle times below 500 ms to be competitive with wire bonding.
- Process monitoring to enable traceability.
- Electrode structure and matrix material of piezo actuator must not be damaged thermally or mechanically.
- Lateral positioning deviation of capillary orifice and joint of < 300 µm, to ensure precise and reproducible melt deposition.

From the state of the art it can be derived, that none of joining processes and technologies described in this chapter meets this multitude of requirements, which arise due to the downstream integration processes described in chapter 2. Thus, a novel approach for joining the electrode structures of piezo actuators with Cu-wires needed to be developed. A possible approach is described in the following chapter.

4 Materials and methods

As pointed out in the description of the state of the art, a lack of suitable joining methods able to fulfil the requirements described in chapter 2 became apparent. Aside from the downstream integration processes, the alloy composition of the piezo module's electrode structure and the connecting wire represents an additional boundary condition, which must be taken into consideration when developing a suitable joining method.

Both, the electrode structures of the LTCC-based piezo modules (LPMs), developed for the casting process and the thermoplastic-compatible piezoceramic modules (TPMs) [29], developed for the hot-pressing process consist of a 20 µm sintered Ag-layer, and 20 µm Ag-foil respectively. Since both electrodes need to be joined to a copper wire of 100 to 200 µm diameter, the fundamental problem to be solved from a metallurgical perspective is the joining of the elements copper and silver. Both elements are amongst the metals with the highest thermal and electrical conductivity. Some basic physical properties of Cu and Ag are shown in table 1.

Table 1: Material properties of silver and copper [57; 58]

Element	Thermal conductivity [W/m K]	Liquidus temperature [°C]	Electrical conductivity [10^6S/m]
Silver	429	962	58.7
Copper	377	1083	61.4

Both metals show a tendency to form thin oxide or sulphide layers in air within a short time period, which passivates the surfaces and thus prevents wetting with other metals or alloys [59]. This effect must be counteracted by the selection of a suitable processing gas and filler material.

4.1 Filler material

A suitable filler material for the described joining task must fulfil the following requirements:

- Liquidus temperature above 593°C (see section 2.1).
- Compliant with restriction of hazardous substances (ROHS) directive.
- Metallurgical compatibility and wettability of Ag and Cu surfaces

- Mechanical strength to resist a shear force of 12 MPa (see section 2.1)

An alloy with particularly promising properties for the described application is the bronze wrought alloy CuSn12, which has a high liquidus temperature $T_{Liquidus}$ and a wide solidification interval. It is classified according to DIN EN 1044 as a copper based braze alloy. The term bronze wrought alloy refers to copper alloys with tin as the main alloying element. The copper-tin alloys are standardised in DIN V 17900 and can contain up to 8.5 wt% Sn. For deoxidizing, the above-mentioned alloys can contain 0.1 to 0.4 wt% phosphorus, which is added in small amounts to achieve deoxidation of the copper-tin melt. This prevents the formation of tin oxide (SnO_2), which would adversely affect the properties of the alloy. The resulting reaction product, phosphorus pentoxide is either vaporised or slagged during the re-melting process of the alloy [60]. This oxidation inhibiting property makes the CuSn12 alloy particularly suitable for the laser drop on demand joining process, since it enhances the wetting of Cu and Ag surfaces necessary to form a substance-to-substance bond.

According to [61] the CuSn12 alloy has a solidus temperature $T_{Solidus}$ of 830 °C and a liquidus temperature $T_{Liquidus}$ of 1000 °C. However, it must be stated that the solidus and liquidus temperatures vary depending on the source: [62; 63]. Figure 4 shows the copper-rich side of the CuSn phase diagram [64].

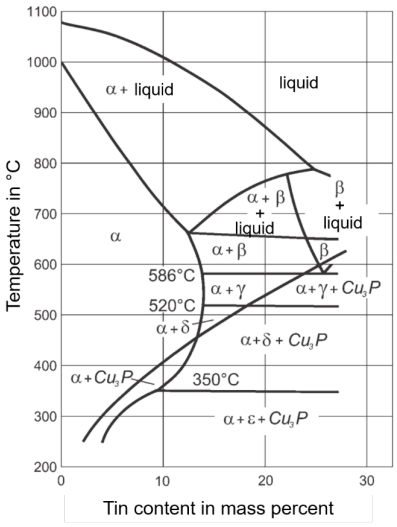

Fig. 4: Copper side of the copper-tin phase diagram [60] reproduced from [64]

The diagram indicates the precipitation of a copper-rich solid solution that forms during the solidification of the CuSn melt. The residual melt solidifies considerably richer in tin than the average content of the alloy would suggest. The exceedingly high tin content of the solidified mixed crystals can only be compensated by diffusion [60]. After solidification, the higher alloyed copper-tin alloys (> 6 wt% Sn) exhibit not only the α phase but also α+δ eutectoid. The dendrite strains and branches of the α phase exhibit an above-average copper content, whereas the α+δ phase, which is mainly formed during steep cooling, is characterised by a higher tin content [65]. By increasing the tin content of the Cu base alloy, the strength and hardness of the microstructure increases [60].

In addition, by adding small amounts of about 0.5 wt% of phosphorus to the alloy, a deoxidative property of the filler material is achieved and the formation of tin oxide (SnO_2) is avoided, which would otherwise adversely affect the alloy's wetting behaviour on metals [66]. Also, since the low-melting tin forms a solid solution with Ag [62], and results in the formation of a metallurgical Ag-Sn-rich phase [67], the material is a suitable choice to generate a firm substance-to-substance bond with the Ag electrode structure. Another reason for the selection of the braze material CuSn12 is the fact that, due to the similar coefficients of linear thermal expansion, it can be assumed that the mechanical stresses introduced into the transition layer between braze alloy and base material are neglectable when the braze alloy cools down (see table 2):

Table 2: Coefficient of linear thermal expansion of braze material [68] und metallisation [58]

	Braze/filler material: CuSn12	Metallisation/Ag electrode	Cu wire:
Coefficient of linear thermal expansion α_{Exp} [10^{-6} K^{-1}]	17.8 [67]	19.7 [69]	16.8 [69]

Thus, the braze material tin-bronze is particularly suitable for joining silver and copper [70]. Furthermore, the filler material CuSn12 is compliant with restriction of the hazardous substances directive. All of these properties make the CuSn12 braze alloy a particularly suitable choice for the described joining application [71; 72; 67; 65] and thus it was chosen as the filler material. Table 3 shows the most relevant physical properties of the alloy:

Table 3: Thermal and electrical properties of CuSn12 [68]

Thermal conductivity [W/m K]	Liquidus temperature [K]	Electrical conductivity [10^6S/m]	Electrical resistivity [Ωmm²/m]
51	1233 K	6.2	0.180

4.2 Laser drop on demand joining (LDJ)

The state of the art in electronics packaging does not provide a joining method which is able to fulfil the large variety of requirements as described in chapter 2. This deficit in the state of the art required the development of a novel joining method tailored to the described tasks. Not only is the ratio of wire and electrode structure thickness not favourable for a welding process, but the joint must also absorb the mechanical loads that occur during the casting process. Thus, the application of an additional filler material, such as a braze, is desirable. This enables the process to exploit the complete area of the solder pad as a joining interface and thus increases the mechanical strength of the joint. In order to provide additional filler material for the joining, a feasible approach was found to be melting a spherical braze preform and depositing it on the joining area. This results in a substance-to-substance bond between the Ag electrode and the Cu conductor. The developed process is referred to as laser drop on demand joining and can be divided into four phases (see figure 5).

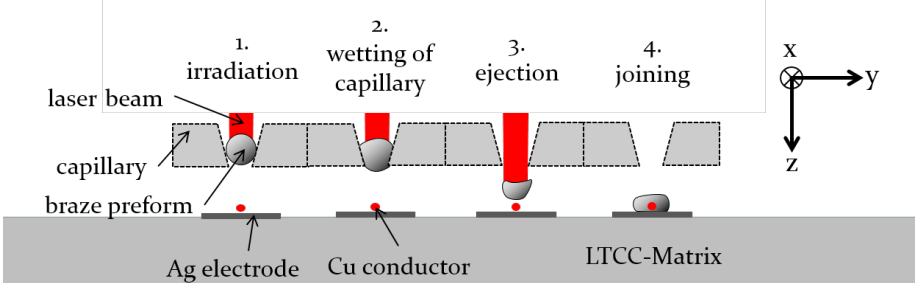

Fig. 5: Schematic of the four process phases of laser drop on demand joining

First, a spherical preform of filler material is inserted into a capillary and irradiated with a laser pulse (1), which heats the preform above its liquidus temperature. During the melting process, the liquid alloy wets the capillary surface (2). As gas overpressure is applied to the machining head, the melt is detached from the capillary (3). After a flight phase, it impinges on the

joining area (4), wetting both the copper wire and the electrode structure, resulting in a firm joint after its solidification.

The proposed process promises significant advantages over the joining processes described in chapter 2:

- It is contact-free, and thus does not induce any mechanical forces into the electrode structures or the piezoceramic.
- The thermal stability of the joints depends solely on the liquidus temperature of used filler material used, and thus can be varied over a wide range.
- The thermal input into the joining area is determined by the braze preform's volume and its liquidus temperature. This enables a defined energy input into the joining area since both properties can be established very precisely.
- The joining area available to form a substance-to-substance bond between the wire and the electrode structure is significantly enhanced, since the filler material's melt can bridge gaps and level out tolerance deviations.

4.3 Preparation of the joining interface

Impurities of the joining interface are not only caused by fats, oils or other residues and processing agents from previous production steps, but also by components of the ambient air. These can impair wetting and diffusion processes. Such oxide or sulphide layers form when Ag or Cu is exposed to ambient air, particularly at elevated temperatures. Sulphur residues can result from contamination during the smelting process of the Cu ores or its storage in inappropriate environments. Since metal oxides show significantly higher decomposition temperatures than the respective metals [73], the presence of oxide layers must be avoided in order not to deteriorate the mechanical and electrical properties of the joints. Thus, a crucial process step is the removal of such surface contaminants prior to the joining process.

One possible way of achieving that goal is via a mechanical processing of the surfaces by rubbing, blasting, scouring or tumbling. However, chemical processes like cleaning with immersion baths (pickling), do not introduce mechanical stress that can lead to damage on the respective electrode structure of the piezo module. Thus, chemical processes are favourable to be used to prepare the joining interface. Pickling enables the generation of metallic surfaces free from oxidic or sulphuric contaminants. This is neces-

sary, since both the braze preforms and the Ag electrode structure are exposed to ambient air and thus atmospheric oxygen which may potentially exhibit sulphuric impurities. Both oxygen and sulphur can interact with the Au and Cu surfaces to form silver and copper sulphide as well as silver or copper oxide layers [74]. By applying a pickling solution, a chemical process is initiated, during which the pickling solution first reacts with the metal oxides and sulphides on the respective surface to form the corresponding electrolytes. Those are subsequently dissolved by the pickling solution.

Thus, the braze preforms as well as the Ag electrode structures are immersed in a solution of deoxidant SENO 2001 Deox [75] and distilled water for about 30 seconds. The electrolytes are then dissolved in the acidic solution with a pH value of 1.2, whereby the base material is almost completely freed from oxidic and sulphuric residues. Subsequently, the braze preforms are rinsed with distilled water to remove the acidic residues of the deoxidant solution. After this treatment, the braze preforms and the piezo modules are stored in an inert atmosphere using a nitrogen cabinet.

Blank Cu wires must be treated in the same way. However, since insulated wires were used in the experiments, a blank surface of the wire is only assured once the polyimide varnish coating is mechanically removed. This is carried out using a precision wire stripper, since the thermal removal of the polyimide varnish, e.g. by flame or laser radiation, would facilitate an instantaneous oxidation of the Cu surface.

5 Setup

The standard solder ball bumping system, as described in section 2.4, cannot provide joints which fulfil the thermal requirements described in chapter 2. However, the process offers several unique features, making it a suitable starting point for the development of an experimental setup. Those features include the possibility to apply additional material to the joining area, and thus to exploit the total area of the solder pad as a joining interface. In addition, the process is contact free, therefore not introducing mechanical stress into the electrode structure, the ceramic matrix or the Ag foil. The impulse of a CuSn12 droplet of about 600 µm diameter impinges on the substrate surface after a flight distance of 1 mm, during which it is accelerated by 9.81 m/s². In addition, the thermal energy induced into the joint is limited by the thermal energy stored in the solder melt. The heat-affected zone is therefore confined to the solder pads. This reduces the risk of exceeding the piezo module's Curie temperature, which would corrupt its functionality.

These advantages however are overshadowed by the fact that the commercial system cannot be utilised to process CuSn12 braze preforms. The various reasons for this, as well as the respective approaches derived and measures taken to overcome these shortcomings will be explained in the forthcoming subsections. It must be emphasised at this point, that the only aspect adopted from the commercial system was its underlying process concept. Due to the inadequate modification possibilities of the commercial system, a laboratory system was set up, for which all components were specifically designed, constructed and manufactured. No components of the conventional system were implemented or utilised in the scope of this work.

5.1 Beam source

The most critical component of the experimental setup is the beam source used to irradiate and melt the braze preform. To determine the necessary optical output power of the system, the operation conditions of the standard system were evaluated. The commercial system processes tin-based solder spheres with a maximum diameter of 600 µm, utilising a fibre laser with a maximum optical output P_{max} of 40 W. To estimate, how substituting a tin-based solder with a copper-based braze will alter the requirements on the beam source, the necessary energy E_o to melt a standard 600 µm solder preform is first calculated, using equation 2:

$$E_0 = (\Delta H_f + c_p \, \Delta T_{Room-Liquid}) \rho (4/3) \pi \, r^3_{preform} \quad (2)$$

Where $r_{preform}$ represents the radius of the preform, σ the density, c_p the specific heat capacity at room temperature, ΔH_f the enthalpy of fusion and $\Delta T_{Room-Liquid}$ the temperature interval between the room and liquidus temperatures of the respective alloy. The physical and geometrical properties of both preforms are shown in table 4:

Table 4: Physical properties of CuSn12 braze and conventional electronic solder SAC 305

	CuSn12 braze	**SAC305 standard electronic solder**
Density σ	8776 kg/m³ (by the rule of mixtures based on [69])	7390 kg/m³ (by the rule of mixtures based on [69])
Specific heat capacity c_p	367 J kg^{-1} K^{-1} (by the rule of mixtures based on [69])	232 J kg^{-1} K^{-1} (by the rule of mixtures based on [69])
Liquidus temperature T_{Liquid}	1269 K[69]	493.2 K [76]
Enthalpy of fusion ΔH_f	91.3 kJ/kg [77]	59 kJ/kg (by the rule of mixtures based on [69])

Using the values given in table 4, gives the theoretical minimum energy E_0 necessary to melt the respective preforms of CuSn12 and SAC305 with an equal radius of 300 µm. The theoretical minima are 0.447 J for CuSn12 and 0.088 J for SAC305 solder. Those energies represent the minimum thermal energy to be deposited on the preform in order to heat it to liquidus temperature, omitting any thermal loss by heat convection, radiation or conduction. In order to melt the braze sphere in the same time period that the conventional system melts the solder sphere, the optical output power of the system must thus be scaled up by almost exactly a factor of five to be able to compete with the conventional soldering system with respect to process cycle time.

For this reason, a YLR-200-SM fibre laser, with an optical output power of 200 W, was used as beam source since the optical output power of that beam source exceeds the that of the standard source by a factor of 5. Its central emission wavelength is 1070 nm and its raw beam diameter is 6.9 mm [78]. The laser beam is focused with a lens with a focal length f = 50 mm. Table 5 shows the technical specifications of the beam source used:

Table 5: Technical specifications of the beam source used

Maximum optical output power P_{max}	200 W
Wavelength λ	1070 nm
Collimated beam radius w_0	3.45 mm
Beam quality factor M^2	1.16
Focal length f	50 mm

It is important to note, that the conventional solder ball bumping system does not have any focusing optic, but the laser beam exits the fiber at the fibers divergence angle and irradiates capillary and braze preform without any sort of beam shaping. The laser beam is basically used to heat the WC/Co capillary which in turn heats the preform by heat conduction. This approach works only for solder materials as the WC/Co capillary would break down after about 80 joining cycles if higher melting alloys such as braze were used as was shown in [85]. Hence a completely new approach was developed in the scope of this work.

The developed experimental setup is shown in figure 6. The beam is deflected via dichroic mirrors, allowing the laser beam to be aligned relative to the capillary and focusing optics. Mirror 3 is transparent in the visible wavelength range and thus enables coaxial process observation using a charge-coupled device (CCD). The system is controlled by a computer on which the programming of a field-programmable gate array (FPGA)-based microcontroller is carried out. In addition, the processing head can be sealed gas-tight and is mounted to a cage system. A detailed description of the gas atmosphere used is provided in section 5.2.

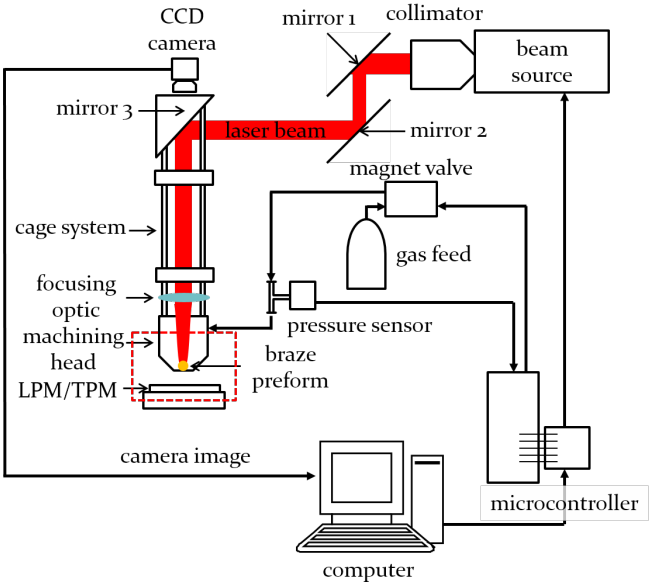

Fig. 6: Schematic of the experimental setup

In figure 7, a section of a CAD model of the machining head is shown to illustrate the geometric dimensions. The beam passes through a beam entry window into the processing head, which is sealed by an O-ring. The beam entry window and the O-ring are fixed in place using a screwed-on cover plate. It is essential that the optical axis of the focusing optics propagates exactly through the centre of the capillary orifice. Due to tolerances, this is guaranteed by attaching the machining head to an XY-translation mount, which is aligned manually before each series of experiments. This measure is necessary, since a misalignment of the laser beam with respect to the capillary orifice would result in a capillary perforation once laser emission is triggered.

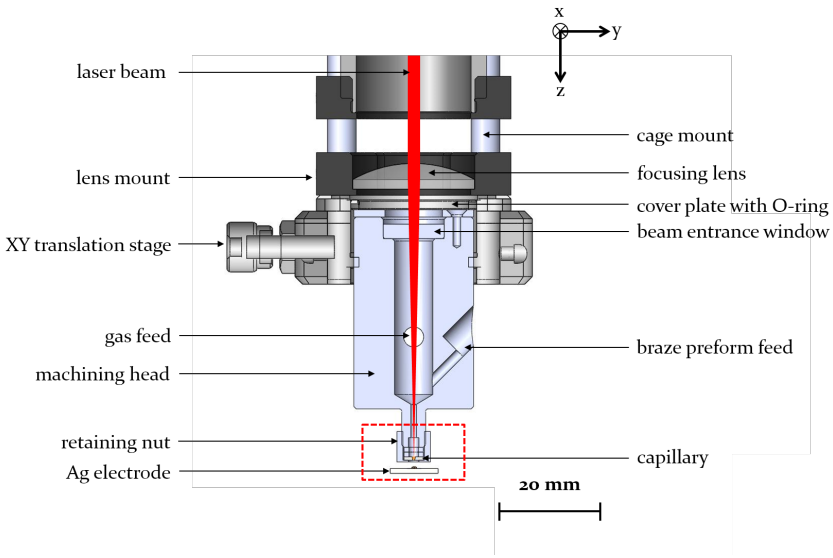

Fig. 7: Enlarged section of the machining head

In order to enhance comprehensibility of the dimensions of the electrode structure and the Cu wire with respect to the machining head and the system in general, the section of the machining head containing the capillary is further enhanced in figure 8. The capillary is screwed into the processing head using a retaining nut with a through-bore. During the joining process, the electrode structure, the substrate and the copper wire are located at approximately 1 mm from the lower edge of the retaining nut.

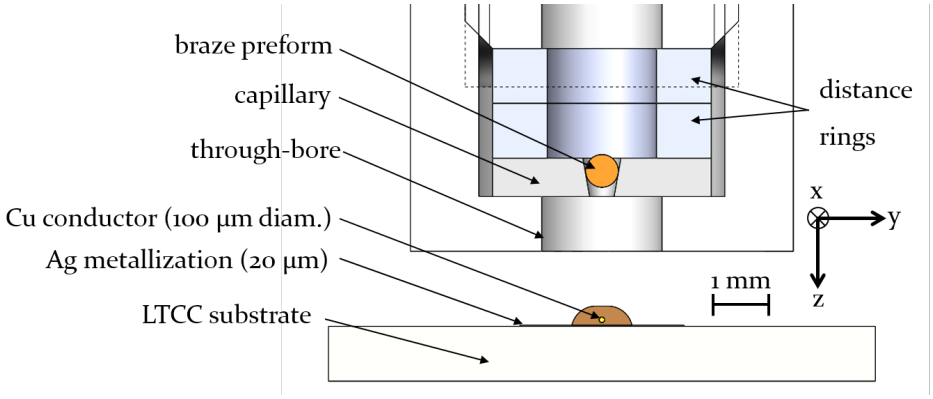

Fig. 8: Detail of the capillary, substrate and electrode structure

5.2 Process gas atmosphere

The gas fed to the machining head is either nitrogen or forming gas 90/10, which is specified according to EN ISO 14175 N5-NH-10 to contain 90 vol.% nitrogen and 10 vol.% hydrogen. The reason for using forming gas is its capability to render oxygen atoms ineffective and to reduce copper oxide to copper [82; 83; 37]. Despite its hydrogen content, forming gas 90/10 is not flammable.

To provide a defined overpressure within the machining head as necessary to detach the braze melt from the capillary, a pressure regulator is connected to the machining head via a polymer hose. The pressure regulator is connected to a process gas cylinder, serving as a gas reservoir. The pressure regulator enables a variable relative overpressure within the machining head of between 0 and 250 hPa. The overpressure is necessary as shown in [79] to generate a sufficiently high force onto the molten droplet to overcome the surface tension that keeps the melt in the capillary. The relative overpressure within the machining head is monitored in situ by a pressure sensor, First Sensor HMA B001 U Z7 H5, which measures the relative pressure difference between 0 and 1000 hPa. The response delay of the sensor is 0.5 ms. It has a zero-pressure offset of 0.5 V and a full-scale output of 4.5 V, corresponding to a 0 and 1000 hPa relative pressure difference. Equation 3 enables a conversion between the sensor's output signal in Volts and the relative overpressure inside the machining head in hPa:

$$p_{rel} = 250\frac{hPa}{V} \cdot V_{PS} - 105\,hPa \tag{3}$$

The sensor's measurement accuracy is specified to be ± 1.5% full-scale span (FSS) [80]. In addition, a 2-way BIBUS series 720 Matrix high-speed solenoid valve enables the process gas supply to be interrupted within 2 ms [81]. A pressure spring keeps the valve closed between joining cycles to prevent the loss of the process gas. The braze preforms are introduced via a plastic tube into the machining head, which is sealed gas-tight during the joining process.

5.3 Capillary

Since the capillary is the only component of the system that is exposed to braze melt, the requirements on the capillary are particularly high:

- Thermal stability at temperatures above 1000°C.

- Low thermal conductivity to avoid temperature loss of the braze melt due to heat conduction.
- No wetting tendency of the capillary with the braze alloy, selected in section 4.1.

The use of tungsten carbide (WC/Co) capillaries, as used by the standard solder ball bumping system, was discarded since copper melt wets [84] and forms intermetallic phases with cobalt. This results in a clogging of the capillary, as confirmed in the experiments carried out in the scope of the work of [85] and thus disqualifies the WC/Co capillaries. Figure 9 shows the clogging of a conventional WC/Co capillary with a CuSn12 braze filler material.

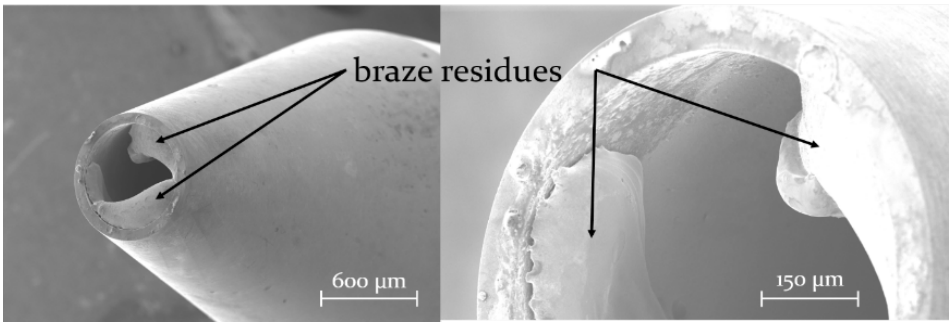

Fig. 9: A tapered standard WC/Co capillary, showing enhanced wetting with a Cu-based braze

To identify a suitable capillary material, various technical ceramics were evaluated in respect of their suitability for the process. In table 6, the three technical ceramics, aluminium oxide (Al_2O_3), aluminium nitride (AlN) and silicon nitride (Si_3N_4) were compared.

Table 6: Thermal conductivities of different technical ceramics

Type	**Thermal Conductivity** [W/mK]
Al_2O_3	24
Si_3N_4	90
AlN	180

A low thermal conductivity of the capillary material results in less thermal energy being withdrawn from the braze preform during the melting process, which facilitates a uniform melting and detachment of braze from the

capillary. As a result, materials with low thermal conductivity are to be preferred as the capillary material. A more detailed description of the investigation into and discussion on that topic can be found in [86]. Also, the braze material's wetting behaviour on the capillary material is critical. In general, technical ceramics exhibit a lower tendency to wetting with metal melts than metals, due to their metallurgical incompatibility. Higher wear resistance is achieved by reinforcing the aluminium oxide with about 4 weight percent of zirconium oxide, resulting in a ceramic called zirconia-toughened aluminium oxide (ZTA). Due to the hardness of the granules and the solid bonding of sintered material between the individual ceramic crystals, ZTA ceramics achieve strength values close to those of metals with an optimum microstructure formation, according to the manufacturer. The material used was Rubalit 708 S, provided by the company CeramTec.

Capillary manufacturing

The capillaries for the LDB process with brazing parts are produced by micro processing using ultra-short pulse (USP) laser ablation. In the literature, ultra-short pulses are defined in the time domain in which the absorption-dependent optical penetration depth corresponds to the thermal diffusion length of the chosen substrate. The cavities were generated, using a Fuego laser with a wavelength of 1064 nm, an average optical output power of 50 W, and a pulse duration of 10 ps, as provided by the company Time-Bandwidth. Beam guidance is carried out by a HurryScan system from the company Scanlab, on which a F-Theta lens with 160 mm focal length was mounted. The contour of the work piece to be machined is created with the software environment SAMLight. The maximum achievable feed speed of the laser beam relative to the work piece surface is 500 mm/s.
The high pulse powers of an ultra-short pulse couple electronic excitation energy from intense electromagnetic fields with the atomic motion of the irradiated substrate's crystal lattice. The crystal lattice is ionised, and the mechanical bonds are broken. As a result, the now free electrons form a plasma which gains additional energy due to the still-acting electromagnetic excitation by the laser pulse. Thus, the plasma reaches extremely high temperatures. Subsequently, the ions are expelled from the irradiated area extremely quickly as the chemical bonds of the substrate are broken, resulting in an ablation process at a macroscopic scale [87]. At high fluencies, small amounts of the solid are sublimated into a plasma of ionised atomic particles, resulting in an ablation of the irradiated area. By material ablation, very high surface qualities are achieved [88]. The process parameters used for structuring the cavities were:

- P_{Laser} = 13,7 W
- d_{Focus} = 30 µm
- f_{Pulse} = 100 kHz
- $z_{Rayleigh}$ = 500 µm
- λ = 1064 nm
- v_{feed} = 500 mm/s
- t_{Pulse} = 10 ps

Figure 10 shows the capillary's cavity after the USP ablation process:

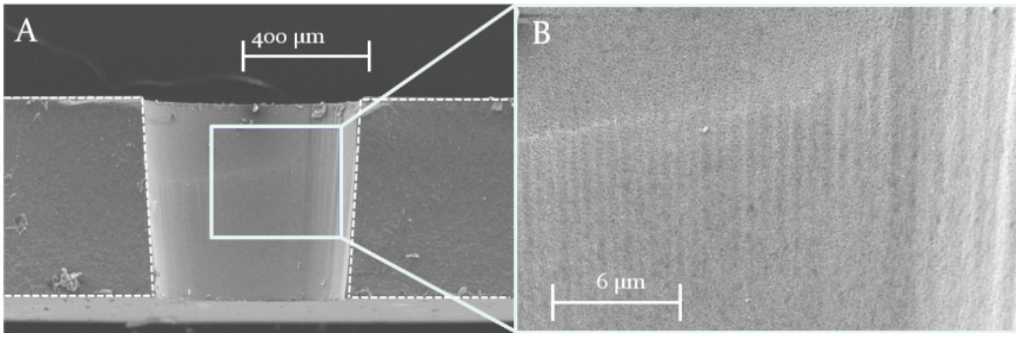

Fig. 10: SEM image of a cross-section of the ZTA capillary's cavity generated by USP ablation

Magnifying the capillary's cavity using an SEM-microscope, a coarse and porous surface becomes apparent (figure 10 right). This porosity results from the manufacturing process of the ceramic, which is sintered from ZTA particles. This property of the capillary's cavity decreases its wetting tendency with the molten CuSn braze, since it reduces the surface area between the melt and the ZTA substrate, which is a preferable property for the desired application. A detailed investigation of the occurring wetting phenomena was carried out in section 7.2.

5.4 Process sequence

During one joining cycle, first, the magnet valve is opened, and inert gas overpressure builds up in the machining head. After approximately 50 ms, a stationary pressure level is established. The laser pulse is emitted 100 ms after the magnet valve is opened. The beam is focused by a lens of f = 50 mm onto the surface of the braze preform. A fraction of about 30% of the incident radiation is absorbed on the braze preform's surface. In metals, the optical absorption is dominated by energy transition from the incident beam to the metal's electron gas by mechanisms such as inverse bremsstrahlung [89]. The excited electrons' energy is subsequently transferred to crystal lattice phonons via collisions [90]. During the melting process, the

braze melt wets the capillary and is subsequently detached from the capillary by the force exerted by the gas overpressure. After a short flight phase, the braze melt impinges on the electrode structure and the Cu wire, wets both and results in a firm substance-to-substance bond after its solidification. After droplet detachment, the orifice is no longer blocked by braze melt and thus the overpressure within the machining head drops by about 20 hPa within 20 ms and then remains constant. Finally, the magnet valve closes 100 ms after the droplet was detached from the capillary, cutting off the gas supply. This results in the machining head's pressure adapting to the ambient pressure level within about 8 ms. Figure 11 shows the signal pattern generated during a joining cycle.

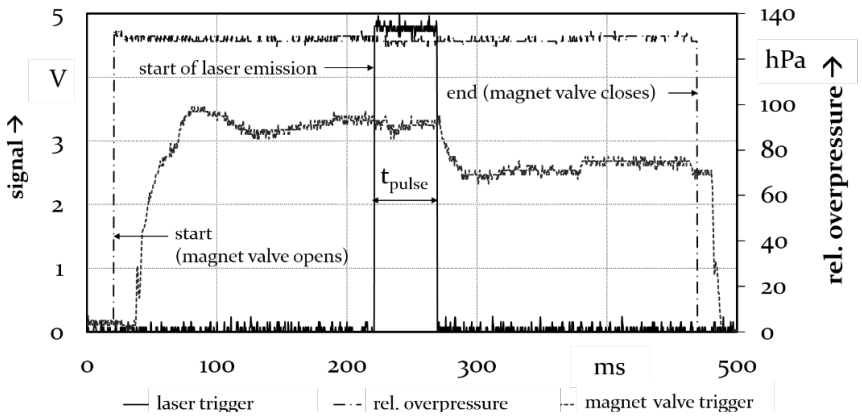

Fig. 11: Signal pattern of a process cycle

The pressure level inside the machining head increases after the magnet valve is opened. However, microscopic investigations of the braze preforms showed that the braze preform's surface is not perfectly spherical: it sometimes shows the formation of satellite particles or a deviation from sphericity. Those deviations originate from the braze preform's manufacturing process of atomisation, which unfortunately facilitates geometric deviations of the braze preforms. Those geometric deviations from perfect sphericity result in a settling movement of the preform within the conic capillary as soon as force is applied to the preform by the increasing gas overpressure and are reflected by the fluctuating overpressure values within the machining head.

5.5 Braze preforms

In the scope of this work, CuSn12 braze preforms were used for the experiments, provided by the manufacturer Ecka Granules, which generates the preforms by atomisation of CuSn12 bulk material in an argon atmosphere.

After atomisation, a subsequent sieving step is carried out to segregate preforms with a desirable diameter of about 600 µm. After delivery, the braze preforms were qualified by microscope imaging and precision balancing. Table 7 shows the mass and diameter of a batch of 100 preforms. The diameter was measured using an Olympus LEXT OLS4000 3D laser-scanning microscope. The masses were quantified using a precision-balance Mettler Toledo XD105 DualRange, with a minimum measuring limit of 0.01 mg and a repeatability of 0.008 mg.

Table 7: Mass and diameter of the CuSn12 braze preforms used

Diameter	632 ± 11 µm
Mass	1.15 ± 0.11 mg

6 System qualification

6.1 Beam guidance and shaping

Due to the high refractive power of the focusing lens, it is particularly suitable to serve as an imaging element for a coaxially mounted CCD-camera. Thus by moving the focusing lens to different position it can be utilized to act as an objective for the CCD, enabling an acquisition of images from inside the machining head. There are three different relevant scenarios, all of which require different lens positions and thus a z-translation, see figure 12.

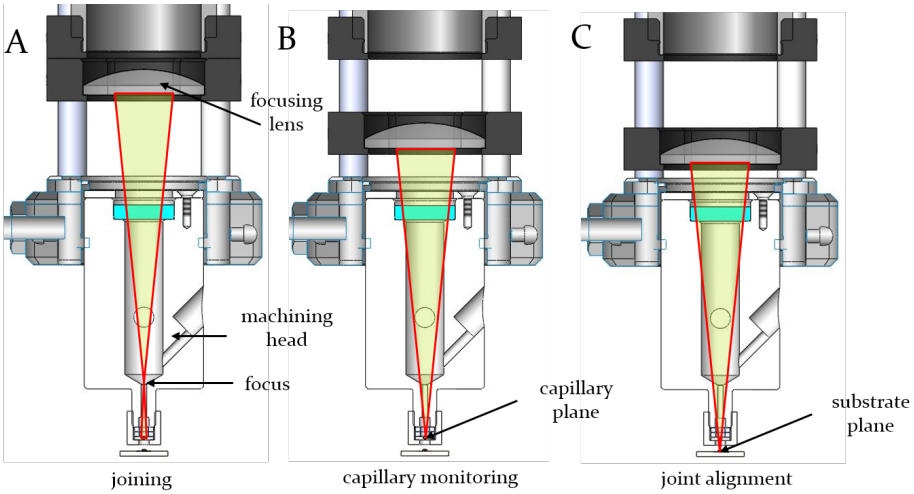

Fig. 12: Different lens positions for A) irradiating the braze preform, B) capillary monitoring, and C) alignment of the machining heads with respect to the joining area

The upper lens position, A in figure 12, can be utilised to modify the intensity distribution on the capillary plane in the desired manner. In particular, it can be used to match the beam diameter to the braze preform diameter. It is critical for the joining process to avoid perforation of the braze preform (see figure 13) since this would result in partial braze ejection and thus the partial deposition of filler material onto the joining interface.

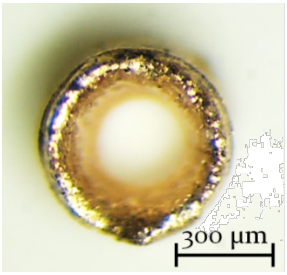

Fig. 13: Preform perforation

Further decreasing the distance between the capillary plane and the focusing lens, B in figure 12, results in the capillary being imaged on the coaxially mounted CCD, since the focusing optics also act as the imaging optic for the CCD. This effectively turns the setup into a microscope. This constellation is used to perform online capillary monitoring by means of machine vision, since the capillary is exposed to significant thermal loads during joining.

At position C, the system is able to acquire a coaxial image of the joining area, necessary for joint alignment. Those three positions can be stored in the graphical user interface and subsequently be set directly.

However, in order to determine the necessary minimal increment respective resolution of the optic's z-translation, and to determine the precise distance required between the focusing optics and the braze preform in order to obtain a beam diameter which matches the braze preform diameter, a few initial theoretical considerations must be taken and some conventions must be established.

In the following sections, the beam diameter or radius will be described by the $1/e^2$ criterion in accordance with [91; 92] and [93]. This enables the analytical description of a laser beam's diameter after its propagation through a focusing lens, and thus the assessment of its intensity distribution at any point along its path. Those conventions are well established in literature and are briefly expressed here in order to enhance the comprehensibility of the following sections. Figure 14 shows the convention of a Gaussian beam propagating through a focusing lens with the focal length *f*, following [94].

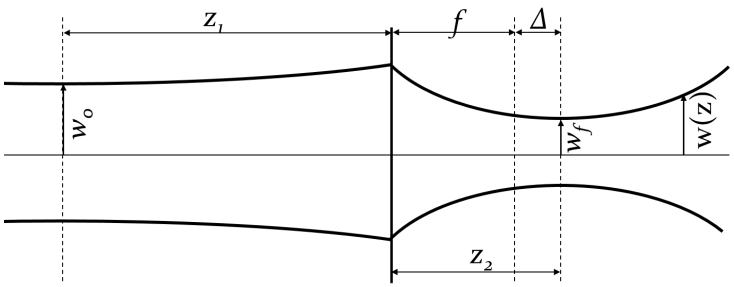

Fig. 14: Gaussian beam propagation through a focusing lens with the focal length *f* following [94]

Using the specifications of the beam source from section 5.1 enables an analytical description of the beam propagation. According to equation 4, a beam waist radius w_f of a focused Gaussian beam of 5.7 µm is obtained [95]:

$$w_f = \frac{\lambda \cdot f \cdot M^2}{\pi \cdot w_0} = 5.7\,\mu m \tag{4}$$

To explain, w_o refers to the waist radius of the collimated beam, w(z) refers to the beam waist radius of a Gaussian beam along its propagation direction, M^2 refers to the beam quality factor, λ refers to the beam source's central emission wavelength, and w_f refers to the waist radius of the focused beam, also known as the focus radius. Due to its high beam quality, the beam can still be approximated as a Gaussian beam. The Rayleigh range z_R is defined as the distance from the focus at which the beam waist is $\sqrt{2}$ larger than at the minimum beam waist w_f at the focal plane of the lens. This range can be calculated using equation 5 [94].

$$z_R = \frac{\pi \cdot {w_f}^2}{\lambda} \cdot \frac{1}{M^2} \tag{5}$$

The Rayleigh range of the beam after propagating through the lens is 96.3 µm. Knowing these values enables the calculation of the divergence of the beam. It was found to be 6.8°. The high divergence is a desired property since it allows for a large beam diameter, and thus a "flat" intensity distribution on the work piece. Hence, this reduces the risk of thermal damage and perforation of the piezo module. In addition, the high divergence enables a very precise tuning of the beam diameter with respect to the capillary orifice by translating the focusing optics in the z-direction. Since manual manipulation and translation of the focusing lens does not provide a sufficiently high positioning accuracy to carry out reliable

experiments, an electromechanical focusing unit was integrated. It was designed in such a way that the minimum resolvable increment in the z-direction of the focusing optics has a minimum increment of travel in the z-direction of 10 µm, representing approximately 1/10th of the Rayleigh range. The overall z-travel of the focusing unit is 75 mm in. Figure 15 shows the joining area as observed via the coaxially mounted camera (lens position C in fig. 12).

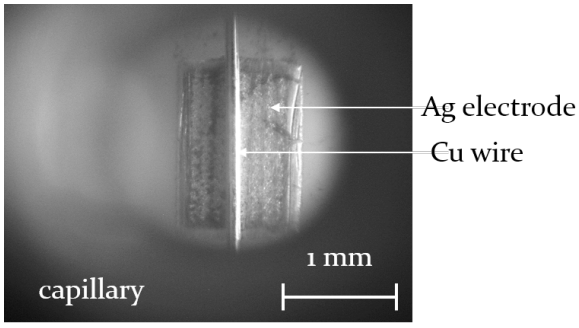

Fig. 15: Coaxial observation of the joining area consisting of a Cu wire and an Ag electrode structure screen-printed on a LTCC substrate. The focusing optics act as a microscope objective at this z-position.

Joining must be carried out at position A, since the intensities would otherwise be sufficiently high enough to instantaneously perforate the Ag electrode (top view, A, figure 16) or the LTCC substrate (cross section, B, figure 16).

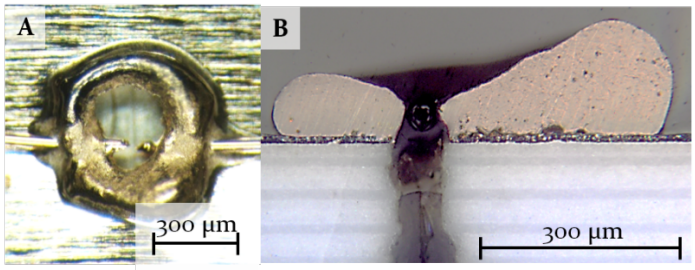

Fig. 16: Electrode, wire and substrate perforations due to an exceedingly high beam intensity

A USB-6009 NI DAQ card with a clock frequency of 150 Hz is used to control the focusing unit. The lens is connected by a threaded rod via a stepper motor driven by a True Transistor Logic (TTL) control signal via an encoder (EC Motion ECMD 241). When selecting a suitable stepper motor, it must be ensured that the sum of the friction torques of the linear guide, bearing housing, seals and the sliding friction torque of the threaded rod, as well as the gravity of the mechanical components do not exceed the holding torque

of the stepper motor. These requirements are met by the SECM 243 stepper motor.

The stepper motor is connected to the threaded rod via a flexible spring bar coupling CPL-12-5-5 in order to compensate for positional deviations between the stepper motor hub and the threaded rod. Two limit switches have been integrated to prevent the lens mount from colliding with the mechanical components of the processing head. For safety reasons, normal closed (NC) switches are used, preventing any movement of the stepper motor if the cable connection is cut. The stepper motor used has a full step angle of 1.8° and is used in half-step mode, to achieve a higher axial resolution and thus, by a factor of two, finer travel increments in the z-direction. The cumulative repeatability of the travel of the focusing unit and the contact switch is 10 µm, which corresponds to approximately 10% of the Rayleigh range of the laser beam and therefore satisfies the requirements of the overall system.

In order to adapt the beam diameter, and thus the intensity distribution, to the diameter of the capillary orifice, it is necessary to describe the divergent laser beam analytically. The position of the beam waist after the laser beam passes through the focusing lens z_2 can be calculated using equation 6, the sign convention is given in figure 14:

$$z_2 = f + \Delta \tag{6}$$

Whereby applies:

$$\Delta = (z_1 - f) \cdot \frac{f^2}{(z_1 - f)^2 + {z_R}^2} \approx 0\ mm \tag{7}$$

In practice, the divergence of the collimated incident laser beam is low, hence Δ can be neglected in equation 6. The maximum power density in the focal plane can be calculated, using equation 8:

$$I_0 = \frac{P_{\max}}{A} = \frac{P_{\max}}{\pi \cdot {w_f}^2} = 1.94 \cdot 10^8 W / cm^2 \tag{8}$$

In order to be able to classify this value, some common power densities and the corresponding physical effects in laser beam material processing have been gathered from various sources and are shown in table 8 (from [96] and [97]):

Table 8: Power densities and their associated physical effects

Power density [W/cm²]	Physical effects
> 10^7	sublimation, formation of plasma
10^6	deep penetration welding, formation of a keyhole
10^5	heat conduction welding
< 10^5	austenitic hardening

Thus, the power densities at the focal plane would be sufficiently high to achieve sublimation and the formation of plasma according to the literature. Obviously, such thermophysical effects are not desired where a uniform re-melting of a metal sphere is to be achieved (see fig. 13 and 16). As a result, the radius of the laser beam should correspond to the radius of the braze preform in order to achieve the most uniform energy deposition possible into the braze preform. The beam waist according to the $1/e^2$ condition must be 300 µm (equation 9). At the same time, the beam should not be broadened beyond the diameter of the braze preform in order to prevent thermally damaging the capillary. That precise z-position at which the beam exhibits a radius of 300 µm is referred to as z_{300}:

$$w(z_{300}) = w_f \cdot \sqrt{\left[1+\left(\frac{z_{300}-f}{z_R}\right)^2\right]} = 300\mu m \qquad (9)$$

Rearranging the equation yields the necessary distance of the braze preform from the lens' principal plane as z_{300} = 55.04 mm. In this z-plane, the peak intensity is reduced to 0.036% of the intensity at the focal plane of the lens (equation 10):

$$I\left(z_{300}\right) = I_0 \cdot \frac{{w_0}^2}{w\left(z\right)^2} = 0.7 \cdot 10^5 Wcm^{-2} \qquad (10)$$

According to table 7, this power density is suitable for heat conduction welding, where the power density domain results in a homogeneous melting of metals without the formation of turbulent vapour plumes or the formation of plasma, all of which are undesired effects. Since the $1/e^2$ criterion is used, and due to the infinite expansion of a Gaussian beam, about 13% of the optical output power of the beam source is deposited into the capillary.

Figure 17 shows the normalised power densities measured in the focal plane of the focusing lens (left) and at z_{300} = 55 mm from the principal plane of the focusing lens (right).

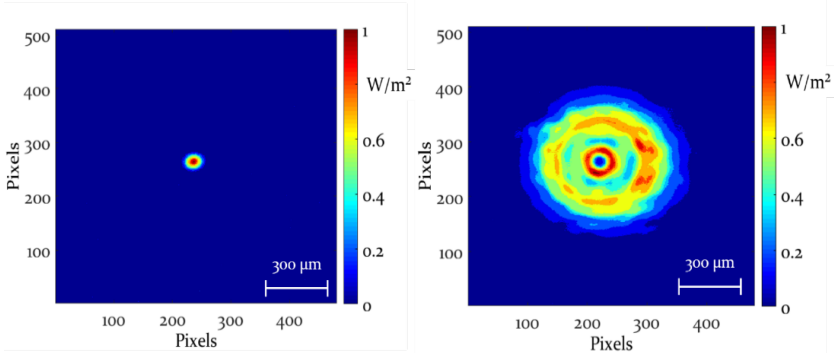

Fig. 17: Normalised intensity distribution in the system's focal plane (left) and after defocusing by 55 mm (right)

The measurements were carried out using a Coherent LaserCam-HR II. The device was equipped with a continuously variable attenuator module, (VARM) UV-C- 190-1100nm, to avoid damage to the CCD. Further, using a dichroic beam splitter with a 5% transmission at the beam source's central emission wavelength of 1070 nm, and neutral density filters Thorlabs ND3.0 and ND4.0, the power was further reduced. The attenuation factor of all filters and the beam splitter is thus $2 \cdot 10^8$. The cascading of the attenuating optical elements was chosen so that the element with the highest attenuation is hit first by the beam. This measure makes it possible to avoid any distortion of the beam, e.g. by the formation of a thermal lens due to thermal expansion of the respective filter.

These measures were necessary to be able to measure the particularly high energy densities in the focal plane of the system. For evaluation, the software BeamView-USB 4.4.2. was used. The measurements indicate a favourable power density distribution at a defocused position of 55 mm as predicted, which matches the capillary orifice diameter precisely.

6.2 Braze detachment time

In order to be able to determine how the power density distribution influences the braze preform's melting behaviour and detachment times, it is necessary to be able to measure the precise duration between the beginning of the laser pulse and the droplet's detachment from the capillary. This is realised by utilising a photodiode (PD) DET 100 A, aligned to the joining position under a lateral angle of about 60° (figure 18).

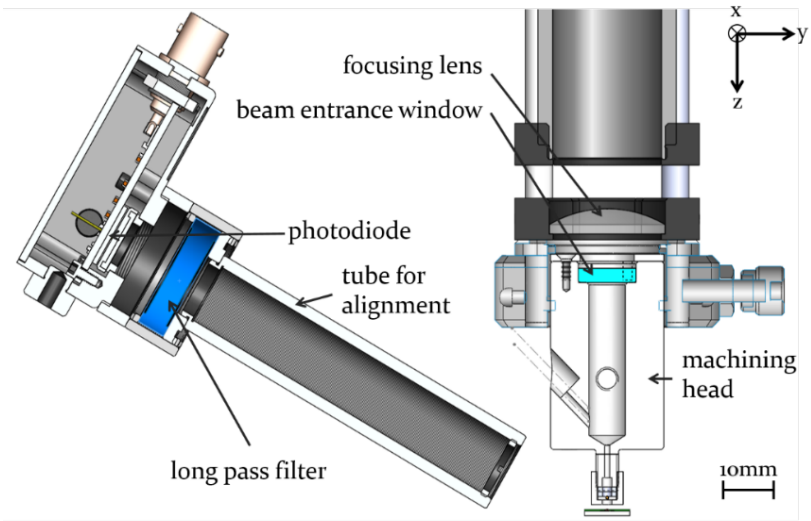

Fig. 18: The setup used for determining the braze detachment by scattered laser radiation, consisting of a photodiode DET 100 A, and the edge pass filter FEL 1050, aligned to the joint at a lateral angle of about 60 degrees

The laser radiation emerging from the capillary orifice is diffusely reflected by the liquid braze onto the PD detector chip. Alignment is simplified by mounting a tube to the PD, which is directed towards the joining area. An edge pass filter is mounted in front of the silicon detector, which filters radiation in a wavelength range of below 1050 nm. This measure is necessary since visible light in the wavelength range of between 330 and 780 nm is used for substrate illumination. This wavelength band of the illumination system would represent a significant interfering factor, since the photodiode would detect radiation in this wavelength range. It even exhibits a higher sensitivity in this range than at the central emission wavelength of the beam source. Thus, it is necessary to limit the detectable bandwidth to the central emission wavelength of the beam source.

Therefore, a 1050 nm edge pass filter was mounted to the photodiode. Above 1050 nm, the filter has a transmissivity of over 80%. In addition, exploiting the PD's inherent drop in sensitivity above 1000 nm, results in an overall sensitivity of the system in a narrow bandwidth gap of between 1020 and 1150 nm. This matches the central emission wavelength of the beam source rather well. Figure 19 shows the spectral sensitivity of the photodiode, the transmissivity of the filter, and the resulting overall sensitivity of the system. The vertical dashed line indicates the central emission wavelength of the beam source. The diagram is standardised to 1 W.

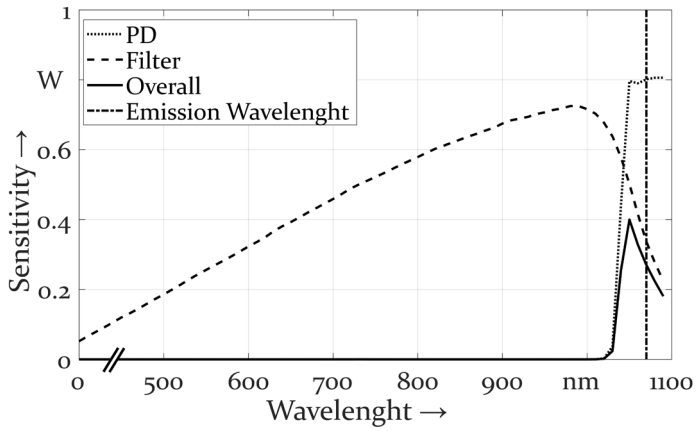

Fig. 19: Spectral sensitivity of the photodiode, transmissivity of the filter, and the resulting overall sensitivity of the system. The diagram is standardised to 1 W.

In order to achieve sufficiently low measurement latencies of braze detachment times, an FPGA-based 40 MHz real-time system was implemented, providing latencies of 25 ns. By evaluating the PD signal, as explained in section 5.4, the braze detachment times for different beam diameters and thus the intensity distributions on the braze sphere's surface can be investigated. The results are shown in figure 20.

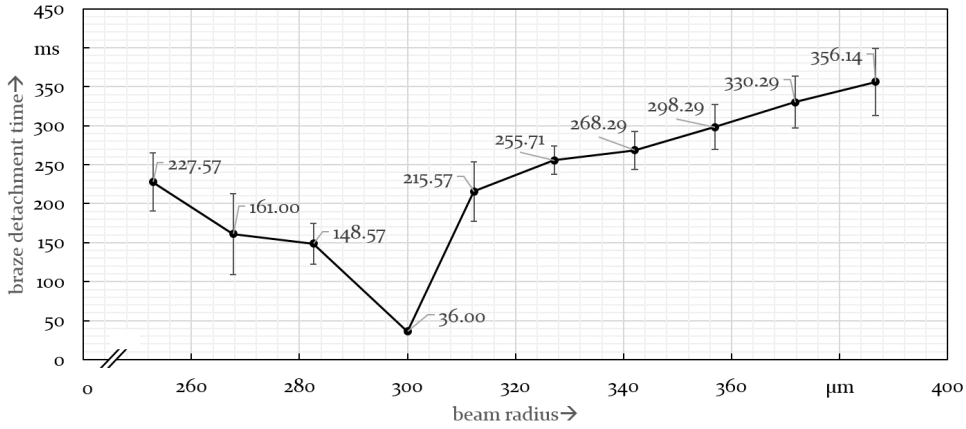

Fig. 20: Influence of the beam diameter on the braze detachment time (n=6)

Matching the beam diameter to the diameter of the capillary orifice not only prevents the capillary from clogging with braze residues, but also reduces the standard deviation of the braze detachment times significantly.

Once the beam diameter matches the diameter of the capillary orifice, the overall process efficiency reaches a maximum, since no fraction of the capillary is irradiated, thus no energy is deposited into the capillary and therefore wasted by heat dissipation. Furthermore, it is interesting to note, that with beam diameters smaller than the braze preform diameter, there is also an increase in the detachment times, which at first glance is counterintuitive. This observation must be attributed to the fact that various mechanical components, such as the through-hole for inserting the braze preform into the capillary, or the cover plate which fixes the O-ring, and the beam entry window, act as apertures, shading areas of the laser beam. This effect is dependent on the z-position of the beam waist, and thus on the focusing lens' position. This shaded fraction of the beam does not contribute to the heating of the braze preform, hence the power passing the processing head was measured as a function of the focusing lens' position.

During this measurement, the solenoid valve was open, to enable cooling of the machining head, since measurements were carried out in a continuous wave mode, leading to a slow heating of the mechanical components of the processing head during the course of the measurement. The measuring device used was a Coherent Field Master GS, equipped with an LM-200 air-cooled measuring head, utilising the measuring principle of a thermopile. The system's relative measurement error is ± 5%. The minimum power resolution is 10 mW and the minimum detectable power is 100 mW. The results of the measurement are shown in figure 21:

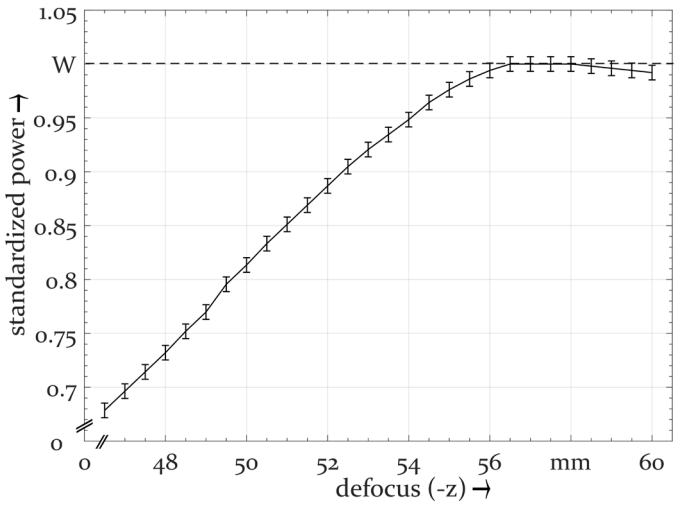

Fig. 21: Power transmission dependant on the focal plane position

The results confirm the assumption that the laser power drops if the mechanical components of the machining head cut a fraction of the beam's cross-sectional area. This effect must be avoided since the lost energy is not utilised for preform heating, but rather thermally damages the machining head. The power losses due to reflection and absorption on the surfaces of the mechanical components of the machining head result in a decreased energy deposition in the braze preform and thus increase braze detachment times. It is important to mention that choosing larger beam radii than 300 µm would result in an irradiation of the capillary, and thus its thermal breakdown after an extended period of joining cycles. Therefore, beam radii of > 300 µm at the capillary plane must be avoided. In the experiments described in the following chapters, the beam radius at the capillary plane was held constant at 300 µm.

6.3 Long-term capillary behaviour

The capillary is the component of the system which has the most significant effect on the shape of the braze preform during the melting, detachment and flight phase. Not only does its shape influence the flow velocity of a passing media, but irregularities of the capillary also contribute to lateral position deviations of the detached braze droplet. This is critical if the process is to be used for industrial applications. In addition, since the capillary is not only exposed to temperatures of approximately 1000 K during a joining cycle, but also to intense heating and cooling rates, monitoring the capillary shape will enable the evaluation of wear, and thus the standing time of such a capillary.

In order to be able to give a statement on the extent to which solder residues form inside the capillary and how these residues influence the process results, the coaxially acquired camera images are evaluated by means of machine vision. In order to be able to evaluate the capillary shape, a binarized image consisting of two regions, the capillary and the capillary orifice, must be acquired. Thus, to assure a maximum image contrast, the focal plane of the focusing lens must coincide with the upper surface of the capillary. Subsequently, an image is acquired, which is binarized by applying a brightness-level threshold to distinguish different image areas. Figure 22 shows a coaxially acquired image of an unused capillary (a) and the binarized image after thresholding (b). It shows the orifice of the capillary (A) and the capillary itself in black (B) [98].

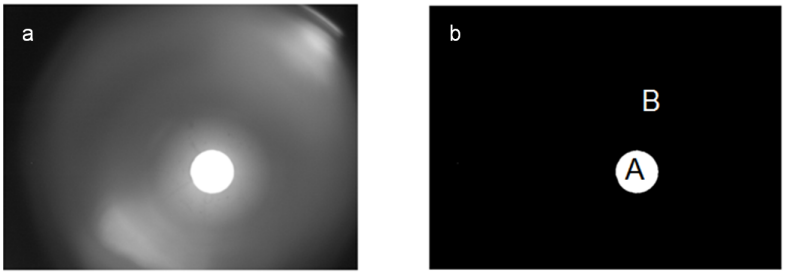

Fig. 22: The initial picture of the capillary (a) and after binarization (b) with two areas: capillary orifice (A) and its surroundings (B) [98]

Next, the convex hull encircling the white area of the binarized image is calculated. The resulting binary image now consists of one area, representing the aperture of the capillary (A) in figure 22. Subsequently, the smallest circle enclosing the convex hull is calculated. This circle serves to build a reference image. Dividing the number of white pixels of the reference image by the number of white pixels of the actual image allows for a statement regarding the area fraction of the capillary orifice which is contaminated with braze residues. Thus, large percentages of e.g. 30% must be interpreted in a way that 30% of the capillary orifice is contaminated by braze residues. Figure 23 shows examples of various cases and the algorithm's response.

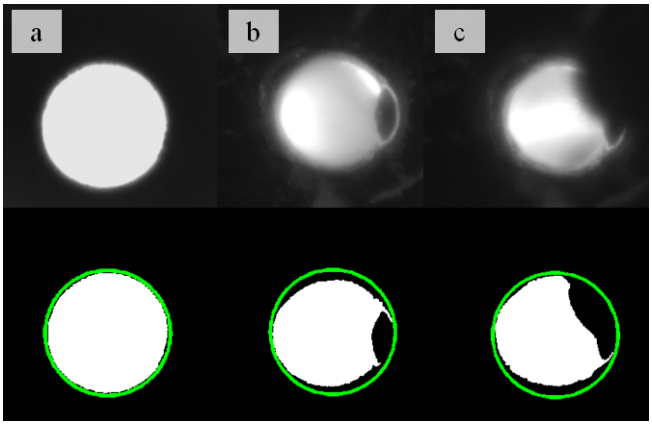

Fig. 23: Image (top) and response (bottom) of the algorithm for an unused capillary (a) and capillaries with braze residues (b, c) [98]

As with any image processing algorithm, the accuracy of the algorithm is strongly dependent on the magnification of the imaging system and its resolution. For capillaries in their initial state (case *a* in figure 22) the algorithm returns an area fraction that is blocked of 6%, which thus represents

the resolution limit. For case *b,* the calculated blocked area fraction is 21.9%. And for case *c,* the algorithm calculates this fraction to be 28.6%. The diameters of the circles were 93, 98 and 100 pixels. Subsequently the algorithm was applied to detect capillary wear over an elevated number of process cycles. Figure 24 shows the evolution of braze residues inside the capillary over a cycle of 2000 joints.

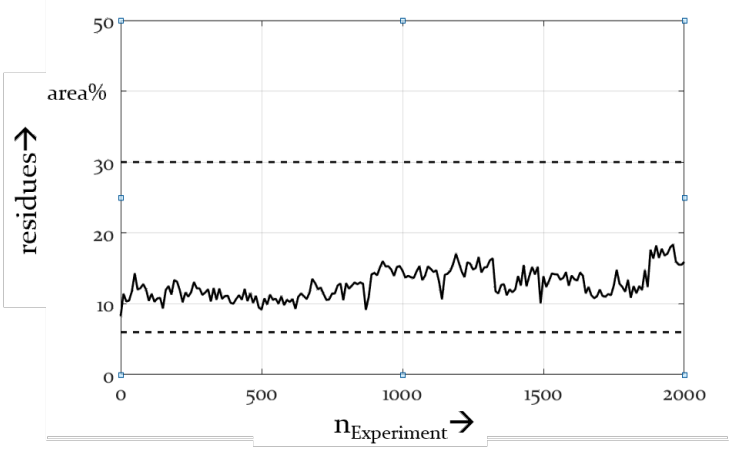

Fig. 24: Evolution of braze residues over 2000 process cycles p: 120 hPa; P_{Laser} = 140 W [98]

The upper dashed line at 30% was found to be a threshold value in preceding investigations [99], demanding the replacement of the capillary. The lower dashed line at 6% indicates the resolution limit of the imaging system. Capillary failure or clogging could not be observed within 2000 joining cycles. Taking the error of 6% of the image processing algorithm into account, the development of capillary residues does not exceed 30%. This was shown in [99] to be sufficient for reproducible joint results. The observations indicate capillary clogging of up to 20%, which nevertheless is not a permanent effect, since subsequent joining cycles clear the capillary orifice from already existent braze residues.

During the experiment no capillary failure was detected, neither was manual cleaning of the capillary necessary. After 2000 joining cycles, a cross-section of the capillary was investigated by SEM Imaging and EDX measurements. Figure 25 shows a cross-section of the capillary (A) with a magnified detail (B):

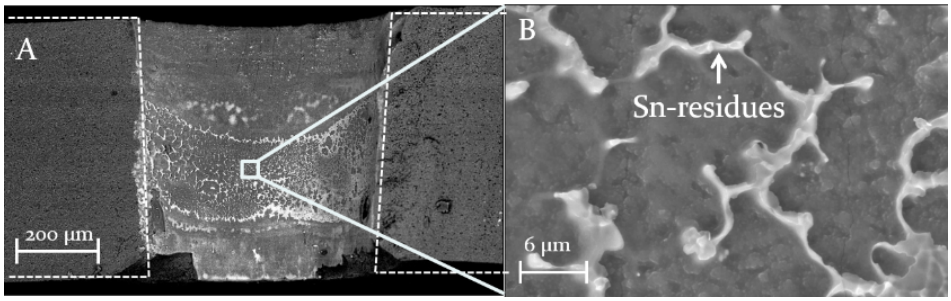

Fig. 25: An SEM image of a capillary after 2000 joining cycles

The porosity of the original sintered ceramic is still visible in figure 25 B, which is exposed by the laser ablation process during capillary production (compare with figure 10). However, in addition, some bright residues seen in the magnified image, extend from inside the cavity of the capillary. By EDX analysis, those residues were found to contain primarily Sn, which is not surprising since Sn is the alloying element with the lowest liquidus temperature. In addition, its viscosity is not only significantly lower than that of the copper portion of the melt, plus it can also be retained in the molten state longer due to the temperature that prevails in the capillary opening during the melting process (for a detailed evaluation of the capillary temperature during a joining cycle, see chapter 7). Both effects enhance a gradual deposition of Sn residues within the capillary. In addition, capillary wetting is supported by the deoxidizing effect of phosphor, which is also an alloying element of the braze material (see section 4.1).

Thus, the phosphor content might be able to reduce aluminium oxide and thus gradually change the surface properties of the capillary. This hypothesis is supported by EDX measurements (see figure 26), showing the elemental distribution of phosphorus inside the capillary after 2000 process cycles.

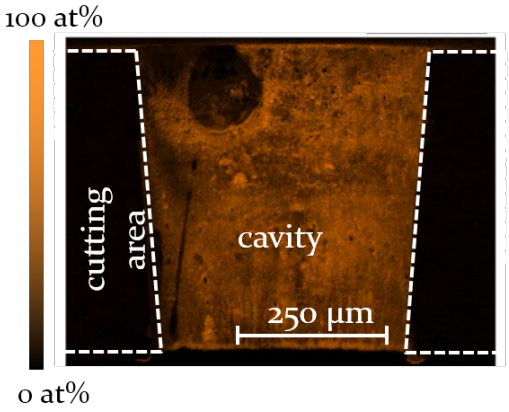

Fig. 26: Phosphorus residues inside the capillary in at%; EDX mapping: Zeiss Merlin Gemini 2 VP Compact 6143 REM; ETH=20.00 kV; Vac. 1.12x10-5 hPa

The phosphorus residues accumulate by adsorption on the aluminium oxide surface of the capillary, and agglomerate there, which is a known phenomenon [100]. However, due to the microscopic scale of Sn and phosphorus deposits inside the capillary, these do not pose a problem for a subsequent droplet detachment process. Particularly, the low-melting Sn deposits are re-melted by subsequent process cycles and expelled from the capillary, as indicated by figure 24.

7 Capillary time-temperature evolution

Since the process described in the scope of this work is a novelty and thus has not yet been thoroughly investigated, it is paramount to understand the actual heating and cooling rates and the resulting temperature fields forming during the joining process within the capillary. In theory, by knowing the expected heating and cooling rates within the capillary, it will be possible to evaluate a multitude of hypothetical materials regarding their suitability to be used as capillary material. Therefore, this investigation is important to establish the hypothetical boundary conditions for capillary material selection, and to indirectly assess the potential standing times of such a capillary.

With the insights obtained in section 6.3, it became apparent that a capillary will be able to withstand 2 000 joining cycles without thermal damage. However it is infeasible to experimentally evaluate the capillary's behaviour at extended numbers of joining cycles of 1 million joints or more due to time restraints on the prototype system. In addition, since measurements with thermocouples are not possible due to restricted accessibility and the small dimension of the capillary orifice and the preform, and since such measurements would influence the process itself, a different approach was chosen in order to indirectly estimate the formation of temperature fields and thus to estimate the capillary's lifetime. To do this, a numerical simulation technique was utilised, which is explained in the following section.

7.1 Numerical model for the evaluation of the thermal cycle during joining

In order to evaluate the thermal input into the capillary during laser irradiation, energy absorption and heating of the braze preform, a fluid dynamic simulation was set up using a multi-physical simulation approach. The model used is based on a model which has already been successfully applied to several laser based joining processes [101; 102]. The numerical problem is solved by applying finite volume methods, and takes the underlying physics of beam/matter interaction, wetting phenomena and heat conduction as well as fluid dynamics into account. It was implemented using the open source computational fluid dynamics (CFD) software package OpenFoam (Open Field Operation And Manipulation, ©OpenCFD Limited). The numerical model consists of 190,000 hexahedral elements. A sectional view of the model is shown in figure 27.

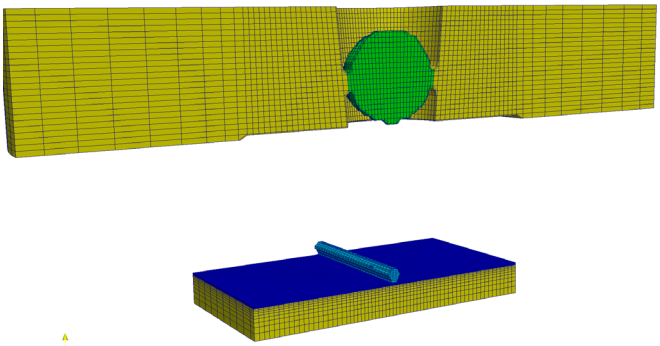

Fig. 27: Section of the meshed CAD model used for numerical simulation, consisting of 190,000 hexahedral elements

Meshing was carried out using the ANSYS ICEM software. The final model consists of five discrete components (figure 28):

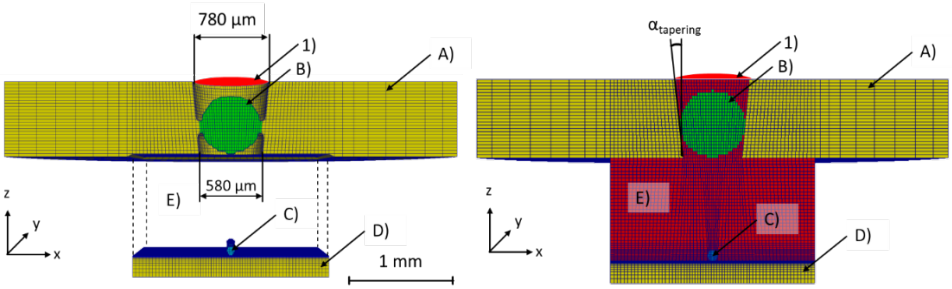

Fig. 28: Meshed model of the capillary (A), the braze preform (B), the substrate with metallisation (D), and the Cu conductor (C), at time step 0 without the air body (left) and with the air body (right), where gas pressure is applied at surface 1

Those components are:

A) The capillary made from the technical ceramic Al_2O_3.
B) The braze preform made of CuSn12.
C) The copper wire that serves as the conductor of the current (Ø = 100 µm).
D) The ceramic substrate consisting of a low temperature cofired ceramic (LTCC) and the Ag metallisation layer, serving as the solder pad and the electrode structure of the piezo element respectively.
E) The air body connecting the described discrete components, visualised in red in figure 28 (right).

The tapering angle of the capillary is 8.13°. The boundary conditions are applied at the boundaries enveloping the volumes of the discrete components as described above. The material properties used in the simulation are shown in table 9:

Table 9: Material properties used in the simulation for air, capillary material, and braze material

	Air	Al_2O_3 (capillary)	CuSn12 (braze preform)
Specific heat capacity c_p	1.188 J kg^{-1} K^{-1}	831 J kg^{-1} K^{-1} [103]	367 J kg^{-1} K^{-1} (by the rule of mixtures according to [69]
Thermal conductivity λ	0.026 W·$(m·K)^{-1}$	34.7 W·$(m·K)^{-1}$ [104]	51 W·$(m·K)^{-1}$ [60]
Surface tension σ_{ST}	-	$760·10^{-3}$ N·m^{-1} (1)	$1{,}825·10^{-3}$ N·m^{-1} [105]
Kinematic viscosity γ_{Kin}	$1.48·10^{-3}$ m^2 s^{-1}	400,000 m^2s^{-1} (2)	$5.352·10^{-7}$ m^2·s^{-1} [106] Value for Cu
Solidus temperature T_{solid}	-	-	1,062 K [60]
Liquidus temperature T_{liquid}	-	2,223 K	1,233 K [60]

For the ceramic with the Ag electrode structure, located at the bottom of the model (D in figure 28), phase transportation is not permitted since the ceramic does not melt during the joining process. Initially, the pressure and velocity values of the discrete phases are set to zero, resembling the initial state of the experiment. As the experiment is carried out at room temperature, the initial global temperature of the model is set to 293 K. The air body, connecting the capillary, braze preform, metallisation and Cu conductor, is subject to two boundary conditions: In the x- and y-directions, the boundary is defined to permit gas and temperature exchange through the interface boundary. In the z-direction, at the top of the model (surface 1 in figure 28), a defined gas overpressure is applied, which resembles the overpressure inside the machining head. In addition, laser intensity is applied at surface 1 which is projected onto the braze preform. The capillary is modelled from a round Al_2O_3 disc with a conic cavity. The lower diameter is 580 µm and the upper diameter 780 µm, which, due to the convex shape, will hold a spherical braze preform with a diameter of 600 µm in place.

[1] The surface energy between the CuSn braze and Al_2O_3 has been implemented in a way so that the wetting angle resembles the measured wetting angle of Al_2O_3 with a molten braze material see figure 30.
[2] The enthalpy of fusion was set to a high value, since the capillary material is not melting during the process.

Since absorption defines the energy input into the braze preform, to accurately model the temperature input and distribution on the curved surface, Fresnel absorption is considered. Absorbed laser radiation is implemented as a heat source, which leads to an increasing surface temperature of the braze preform and finally results in its complete melting.

To model the melting process of the preform, the heat equation with convective and conductive heat transfer is solved, taking the enthalpy of fusion into account. This plays a crucial role in the energy balance during melting and solidification of brazing processes [101]. For each volume element, the temperature T is thus determined by applying the heat transfer equation (equation 11) in which ρ denotes the density, $\vec{u}$ the fluid velocity vector, T the absolute temperature, and t the relative time:

$$Q = \frac{\partial(\rho H)}{\partial t} + \nabla \cdot (\rho \vec{u} H) - \nabla \cdot (\lambda \nabla T) \quad (11)\ [130]$$

Thereby H is the enthalpy defined as the specific heat capacity c_p multiplied by the absolute temperature T plus the latent heat L:

$$H = c_p T + L \quad (12)\ [130]$$

The source term Q in equation 11 corresponds to the absorbed energy available for heating the braze preform. The heat transfer equation is subsequently solved iteratively for every time step. Since the goal is to simulate the process behaviour accurately, particularly the fluid dynamics of the melt during heating and detachment from the capillary, its wetting behaviour with the capillary material must be considered in order to obtain realistic results. Therefore, the CuSn12 braze material, capillary material, and air volume were modelled as individual incompressible fluid phases. To enable an analytic process description of a multi-phase system, a coupled system of differential equations needs to be solved. First, conservation of mass is ensured by implementing the continuity equation (equation 13):

$$\frac{\partial \rho}{\partial t} + \nabla \cdot (\rho \vec{u}) = 0 \quad (13)$$

Furthermore, to account for the different phases, the phase transport equation is taken into consideration (equation 14):

$$\frac{\partial \alpha}{\partial t} + \nabla \cdot (\alpha \vec{u}) = 0 \quad (14)$$

Whereby α is the phase indicator function which specifies the volume fraction occupied by each phase. To determine the coordinates of the free surface between the liquid braze material and the surrounding air respective to the capillary, the volume of fluid (VOF) approach according to [107] is applied. This approach was chosen in order to obtain a good description of the relevant wetting phenomena, needed for an accurate simulation of the droplet detachment from the capillary. A surface tension model [108] was therefore adapted to enable the calculation of surface tension effects for multiple phases and include both radial and tangential forces on the fluids.

7.2 Wetting behaviour of the Al_2O_3 capillary and the molten CuSn12 braze

Since understanding the wetting behaviour of the capillary material used is crucial for process modelling, the wetting angle occurring at the solid/liquid/gas phase between the molten CuSn12 braze, the Al_2O_3 ceramic, and the surrounding gas was measured using the sessile drop method (figure 29):

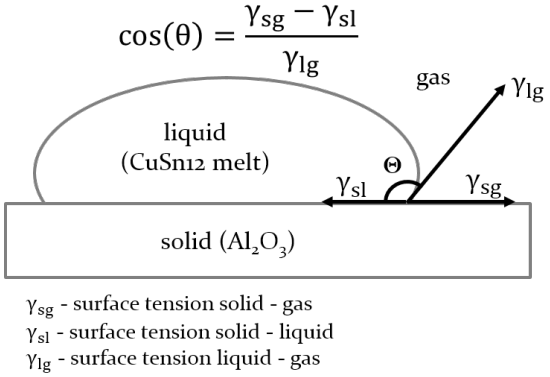

Fig. 29: Schematic of determining the wetting angle by the sessile drop method

To generate liquid CuSn12 droplets on Al_2O_3 substrates, a process chamber with an inert gas atmosphere as described in [109] was used, in order to resemble similar conditions as in the described droplet joining process. During the wetting experiment, a wire feeder imposes the CuSn12 wire into the process chamber, enabling the irradiation of the wire tip via a window with a laser pulse of 2 kW of laser power and a 2 second pulse duration. The wire tip melts and droplet detachment are enforced by an abrupt retracting of the wire. The droplet thus wets the ceramic substrate placed below the wire after a short flight phase. Due to the low thermal conductivity of the ceramic, 34.7 W/m K [104], the droplet cools below the solidus temperature

after the oscillation of the droplet has ceased. Thus, the stationary wetting angle is exhibited in the liquid state. The laser drop on demand joining setup itself could not be used to determine the wetting angle, since the momentum of the process gas jet influences the droplet shape during its cooling, before a stationary wetting angle is formed. The wetting experiment is monitored by means of high-speed imaging. Figure 30 shows a schematic of the experimental setup and the stationary wetting angle exhibited at the interface of molten CuSn12 and Al_2O_3. The value of the stationary wetting angle Θ was measured to be 130 degrees in the liquid state. Subsequently, the wetting angle was implemented in the simulation model.

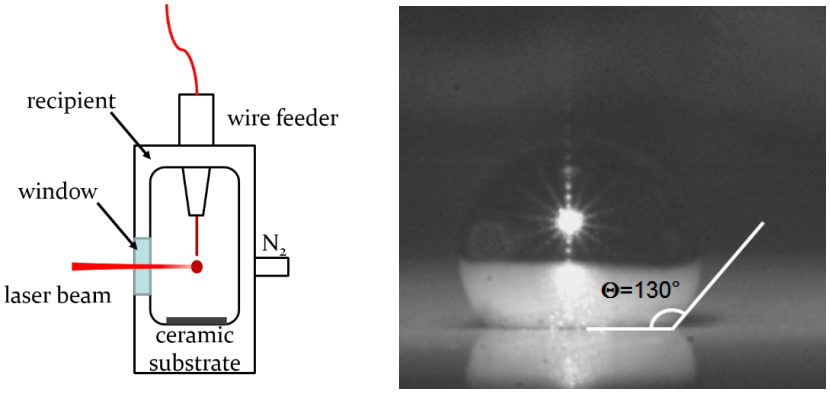

Fig. 30: Experimental setup for the determination of the wetting angle (λ_{Laser} = 1,030 nm; P_{Laser} = 2 kW; v_{Wire} = 1 m/min; t_{Pulse} = 2 s) [86]

7.3 Time-temperature cycle of the capillary during joining

In earlier works, significant heating and cooling rates of the capillary during irradiation and droplet detachment were found to be the main reason for capillary failure [85]. The described numerical approach is used to obtain space- and time-resolved information regarding the thermal load of the capillary during one joining cycle. Thus, the numerical model presents the only method to understand the process dynamics inside the capillary, without interfering with the process itself. Figure 31 depicts the time-temperature evolution for four discrete points inside the capillary during a melting cycle as numerically calculated with the simulation model.

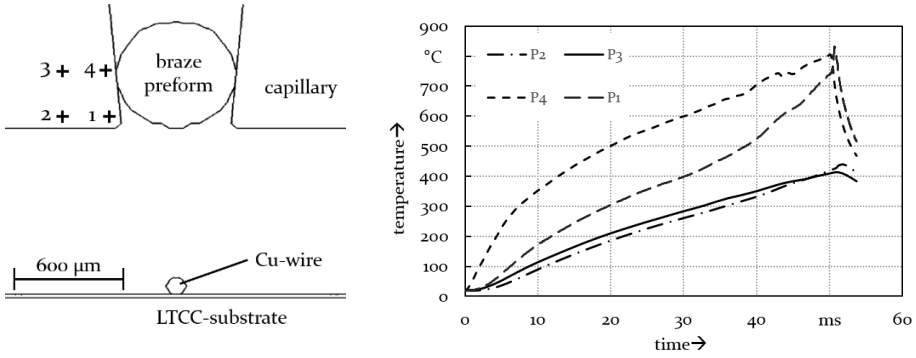

Fig. 31: Simulation of the time-temperature cycle at four discrete points inside the capillary over time during a melting cycle (P_{Laser} = 150 W, $p_{Nitrogen}$ = 120 hPa, capillary material: Al_2O_3, braze material: CuSn12)

The result shows significant thermal input into the capillary due to heat conduction from the braze preform during its melting and detachment process, as well as due to absorption of laser radiation in the cavity of the capillary. According to the simulation, droplet detachment occurs shortly after 50 ms. The heating rate at points 1 and 4 is 22,100 Ks^{-1}. In the bulk material (points 2 and 3), the temperatures rise to 438°C and 413°C respectively, indicating heating rates of about 8 700 Ks^{-1}. The findings indicate that the melting temperature of Al_2O_3 of 2323 K [110] is never exceeded during one joining cycle, which is consistent with the experiments carried out in section 6.3.

To validate the simulation, the period from beginning of the laser pulse until droplet detachment was measured by using the photodiode setup as explained in section 6.2. The experimental results were compared with the numerical results, where it was found to be 51 ms in the simulation and 37.5 ms in the experiment, resembling a deviation of 33%. Considering the complexity of the process the results show surprisingly good conformity with the experiment. The deviation may be explained by the fact that multiple reflections are not taken into consideration in the numerical model, which results in reduced energy deposition in the numeric model in comparison to the experiment.

Furthermore, the droplet velocities during the flight phase have been measured experimentally by means of high-speed imaging (for details, see section 8.3). The droplet velocity according to the numerical model was found to be 1.6 m/s whereas the mean droplet velocity in the experiment was 1.9 m/s (n=5) and thus is 13% higher. This can be attributed to the micro

roughness of the actual capillary (see figure 10). This micro roughness inhibits the wetting of the capillary as it decreases the interface area, which can result in higher droplet velocities. Since the surface tension is the sole force preventing the droplet from detaching, it can be concluded that the numerical model incorporating the measured stationary wetting angle resembles the experiment fairly well.

7.4 Summary and conclusions

Since a direct measurement of the process dynamics inside the capillary during the irradiation and heating of the preform is not possible, a numerical model was set up to describe this crucial process phase. A numerical FVM model was created, which takes the measured wetting angles of molten braze (CuSn12) and the capillary material (Al_2O_3) into consideration. The value of the wetting angle was obtained by applying the sessile drop method. The simulation model considers the wetting behaviour of the capillary with the molten braze material, the Fresnel absorption and the intensity distribution of laser radiation, as well as the heat conductivity and the geometry of the capillary. This approach enabled the evaluation of a spatially resolved time-temperature evolution inside the capillary during a joining cycle.

The results indicated heating rates exceeding 22 100 K s^{-1} at the orifice of the capillary due to the absorbed laser radiation and heat conduction by molten braze material during a joining cycle. A comparison of droplet velocity and braze detachment times shows the numerical model is in good accordance with the experiment. The presented numerical approach represents the only method available to obtain space- and time-resolved information regarding the thermal loads that the capillary is exposed to during one joining cycle. The numerical results confirmed that the melting temperature of the capillary material used, Al_2O_3, is not exceeded during melting and droplet detachment, which was indicated by the experiments carried out in section 6.3. The initially formulated hypothesis that a suitable material can be identified by a numerical process analysis has thus been confirmed and may be applied to new materials in the future.

8 Impact of capillary shape on gas velocity and droplet trajectory

Altering the shape of a capillary influences the fluid dynamic behaviour of a passing medium and has been studied extensively in recent years [111–114; 103; 115]. In theory, a diffusor shape capillary would result in a decreased momentum transfer from the gas jet and the gas molecules respectively to the braze droplet after its detachment from the capillary. This would impact the process result since a diffusing process of the capillary would enable larger process windows, particularly at higher gas pressures, since the droplet might atomise if a sufficiently high momentum transfer from the gas jet to the droplet occurs. In addition, a diffusor shaped capillary will homogenise the gas velocity fields below the capillary. This might hypothetically result in lower lateral positioning deviations between the capillary orifice and the final position of the braze droplet on the electrode structure, effectively increasing the system's accuracy. In order to test this hypothesises, further simulations were carried out.

In order to identify a suitable geometry, several different geometries have been simulated and evaluated, particularly regarding the reduction of the gas flow velocity fields at their orifice and below.

8.1 Simulation

To evaluate the influence of the capillary geometry on gas flow velocities, a three-dimensional simulation model consisting of 90,500 hexahedral elements was created and meshed. Figure 32-1 shows the standard conic capillary, referred to as geometry 1 in the following sections. It exhibits an upper diameter of 780 µm and an orifice diameter of 580 µm. Figure 32-2 shows a meshed model of a diffusor-type capillary. It consists of a conic shaped cavity with an upper diameter of 780 µm and a waist diameter of 580 µm in the centre of the ceramic plate. This convex shape is necessary to hold the braze preform in place. At the bottom of the diffuser-type capillary, a radius of the curve of 1.12 mm was defined to broaden the orifice and to obtain a diffusing effect on the passing process gas (figure 32.-2).

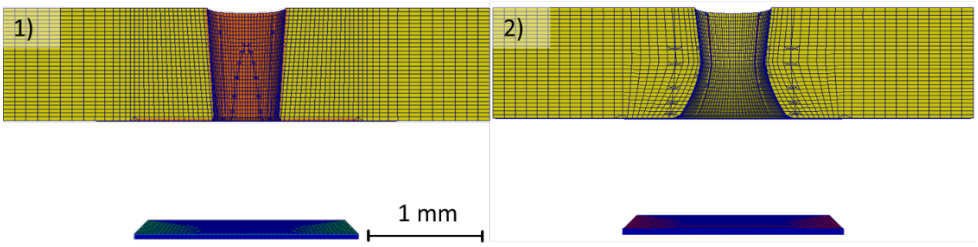

Fig. 32: Meshed models of a conic capillary (geometry 1) and a diffuser-type capillary (geometry 2)

Applying a defined overpressure to the capillary enables a way to determine the impact of the capillary's shape on the passing medium's flow velocity. Figure 33 shows the numerically acquired gas velocity fields after the stationary state is reached for the conic capillary (left) and diffuser-type capillary (right) after applying an overpressure of 125 hPa.

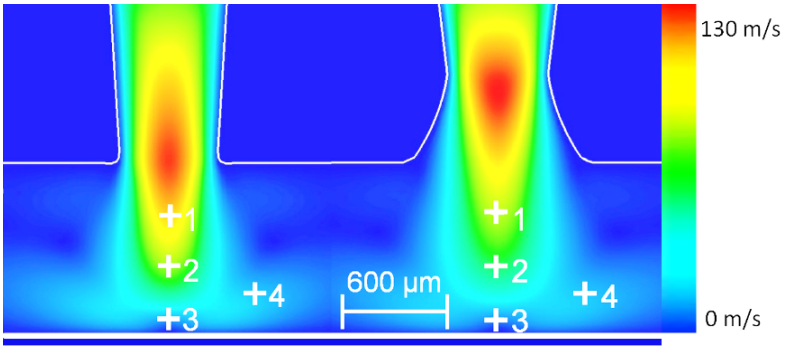

Fig. 33: Stationary gas velocity fields for a conic capillary (geometry 1, left) and a diffuser-type capillary (geometry 2, right), after applying an overpressure of 125 hPa; cross sectional view [86]

The diffuser type capillary exhibits lower gas velocities in the area below the capillary than the conic shaped capillary. However, in order to give a quantitative statement regarding the reduction of gas flow velocities, the four discrete points highlighted in figure 33 have been evaluated. The results at the particular points for various applied overpressures are shown in figure 34.

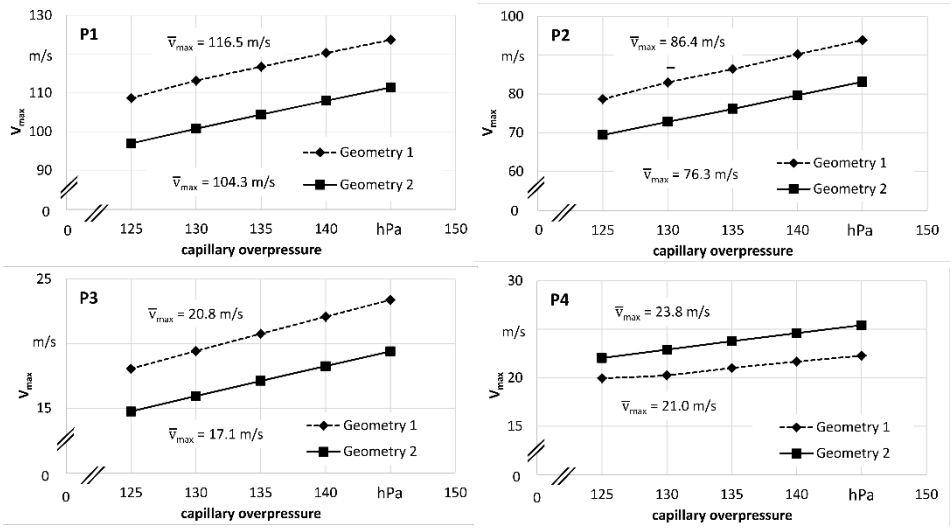

Fig. 34: Influence of overpressure and capillary geometry on the gas flow velocities at points 1, 2, 3 and 4 as highlighted in figure 33 [86]

According to the numerical data, it can be concluded that a modification of the capillary geometry results in a reduced gas velocity in the joining area. By modifying the capillary geometry according to the numerical model, the average gas velocity for points 1, 2 and 3 can be reduced by 10.4%, 11.8% and 17.57% respectively. For point 4, the velocity increases by 13.3%. This can be attributed to the diffusing effect of capillary geometry 2, which results in a uniform distribution of the gas velocity fields in the joining area. These findings indicate a more homogeneous droplet geometry. Further, by increasing the applied overpressure, the velocities increase linearly. With decreasing distance from the capillary orifice, the flow velocities decrease since the substrate below the capillary acts as a barrier for the gas molecules.

8.2 Machining

In order to verify the numerical results, two different capillary geometries were machined by means of laser ablation, one with a conic shape and another with a diffuser type geometry. In order to verify the numeric results experimentally, both geometries were machined by laser ablation, applying picosecond laser pulses. In order to produce such capillaries the ablation strategy described in [116] was used to enable the generation of cavities of defined dimensions. Both the standard conic capillary (geometry 1, figure 32) and the diffuser-type capillary (geometry 2, figure 32) were machined by laser ablation. The parameters used for the ablation process were:

- P_{Laser} = 13,7 W
- d_{Focus} = 30 µm
- f_{Pulse} = 100 kHz
- $z_{Rayleigh}$ = 500 µm
- λ = 1064 nm
- v_{feed} = 500 mm/s
- t_{Pulse} = 10 ps

Geometry two was generated in two steps. First the upper part of the cavity was generated. Subsequently the capillary was rotated 180°, followed by another ablation process with modified parameters to obtain the desired geometry (2 in figure 32). The surface roughness inside the cavity of the capillary after laser ablation was measured using a laser-scanning microscope. The values for Rz and Ra were found to be 0.9µm ± 0.16 µm (n=5), and 0.19 µm ± 0.03 µm (n=5) respectively, which is small in comparison to the preform diameter. Nevertheless, microscopic capillary roughness could result in turbulent gas flow at the interface between the capillary and the passing medium. This is not taken into consideration in the numeric model.

In order to measure the influence of the overpressure and capillary geometry on the droplet geometry after its solidification, droplets are generated using both capillary types, varying the inert gas overpressure inside the machining head. Height and diameter of the droplets are measured after solidification using a laser-scanning microscope to obtain three-dimensional data of the droplet topology. The experimental results are shown in figures 35 and 36.

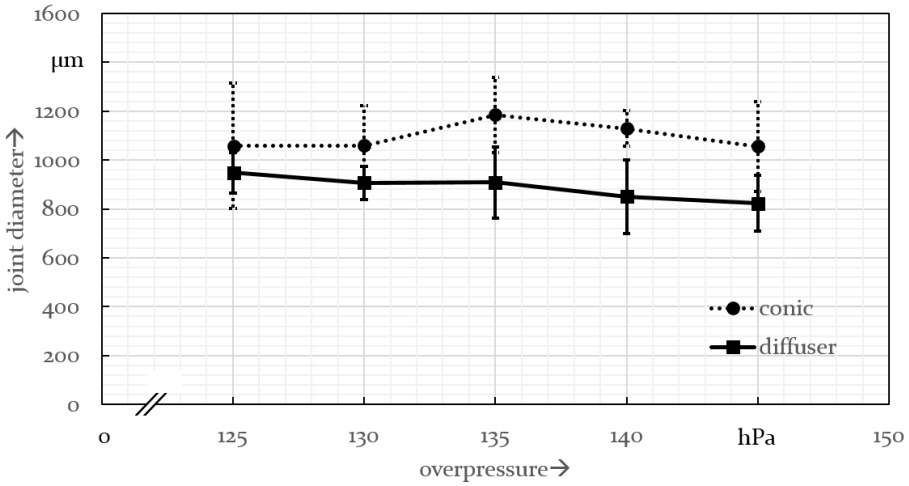

Fig. 35: Influence of capillary overpressure on droplet diameter in a congealed state for different capillary geometries (P_{Laser} = 140 W, working distance = 1 mm, N = 5)

The average droplet diameter for after solidification over all pressures was reduced from 1098 µm for capillary geometry 1 to 887 µm for capillary geometry 2, which resembles a reduction of 19%. The mean standard deviation of the droplet diameter over all pressures was reduced by 32% from 166 µm for capillary geometry 1, to 113 µm for capillary geometry 2. Thus geometry 2 provides more uniform droplet shapes than the standard conic capillary, as predicted by the numerical model. This is explained by the homogenised gas flow velocity field generated by the diffuser-type capillary. The same method was applied to evaluate the maximum droplet height (figure 36).

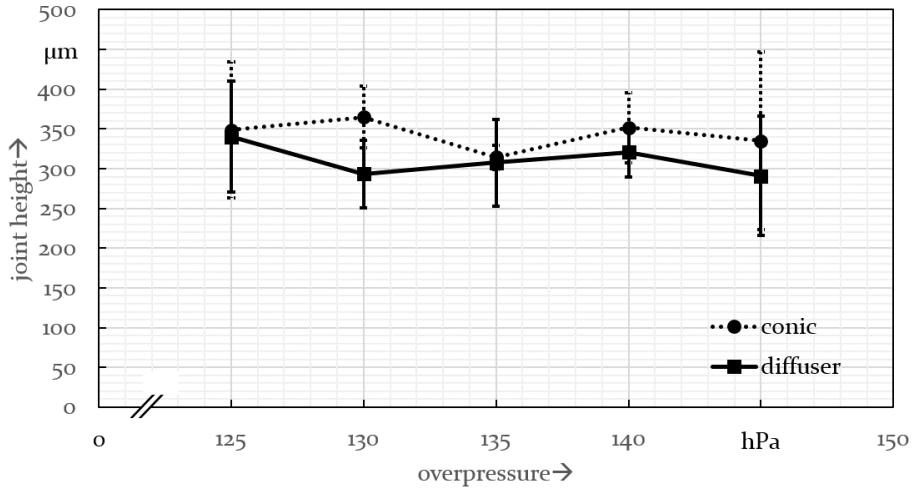

Fig. 36: Influence of capillary overpressure on droplet height in a congealed state for different capillary geometries (P_{Laser} = 140 W, working distance = 1 mm, N = 5)

The results show a reduction of the mean droplet height after solidification from 343 µm for the conic capillary (geometry 1), to 311 µm for the diffuser-type capillary (geometry 2) which represents reduction of 9.5%. The standard deviation of the droplet height was reduced from 59 µm for the capillary geometry 1 to 55 µm, representing a reduction of 7.5%. Thus, also regarding the droplet height, the diffuser-type capillary shows a higher reproducibility in comparison with the conic-shaped capillary. It can therefore be stated, that the impact of the capillary geometry on the droplet diameter was more significant than on the maximum droplet height. Thus, the diffuser-type capillary is to be favoured regarding the reproducibility of the process results. These results, however, do not allow any statements regarding droplet flight velocity and trajectory, and thus cannot predict droplet deposition accuracy. This is a significant factor if the system is to be used for high-volume production. In order to evaluate said properties dependant on the process parameters, another approach was pursued.

8.3 Droplet tracking using stereoscopic high-speed imaging

In order to understand how capillary geometry, gas overpressure and pulse power influence the droplet flight trajectory and velocity, investigations utilising stereoscopic high-speed imaging and image processing were carried out. This approach enables the three-dimensional tracing of the droplet during its flight phase. Two Vision Research Phantom V1210 high-speed

cameras were used, which were aligned at a 31.5-degree angle, to form a convergent stereo camera system (figure 37). The cameras complementary metal-oxide-semiconductor (CMOS) sensor has a pixel size of 28 µm and a bit depth of 12 bits. The dimension of the sensor is 35.8 mm x 22.4 mm with a maximum resolution of 1280 x 800 pixels, at which an image rate of 12,000 fps can be obtained. The maximum framerate of 103,400 fps can be obtained at a resolution of 256 x 256 pixels or below [117]. In the experiments, a framerate of 30,000 Hz at a resolution of 512 x 512 pixels was chosen. These parameters ensure a comparably large field of view while maintaining a high recording frequency, and thus represent a good balance of the required spatial and temporal resolution. Said parameters were kept constant for all experiments. In order to protect the CMOS sensor from scattered laser radiation and overexposure, two edge pass filters were mounted in front of the lenses, which are transparent solely within a narrow wavelength band of the pulsed illumination laser at a wavelength of 807 nm. The frequency of the illumination laser is matched to the 30,000 Hz recording frequency of the cameras.

To obtain 3D information of the droplet flight trajectories, the following steps must be carried out:

- Camera alignment and synchronisation.
- Recording of a calibration pattern for different angles and distances.
- Calibration by edge detection, which is divided into:
    - Single camera calibration.
    - Stereo calibration.
- Rectification of the recorded frames.

After the alignment of the cameras, single- and stereo calibration is carried out by applying the method proposed by [118] and [119], using the software environment Matlab. In order to obtain high-quality calibration images and thus accurate results, a precisely manufactured calibration pattern is necessary since the process observation is carried out at a microscopic scale. Therefore, a 6×7 aluminium oxide checkerboard pattern, with a 2 mm edge length of each square, and an accuracy of ± 0.001 mm was used (see figure 37 left). Sintered aluminium oxide was chosen as the substrate material of the calibration pattern since it suppresses reflections of the illumination laser better than e.g. glass calibration patterns. During the recording of the calibration images, the checkerboard pattern is positioned at the precise position where the capillary is located during joining experiments. It is translated and rotated in in every spatial direction to generate a large number of calibration images. Image 37 shows the visualisation of

the stereoscopic camera system and the respective optical axis of both cameras as indicated by the dashed lines. Camera 1 represents the coordinate origin. Further, in figure 37 right, 20 exemplary calibration pattern planes are shown in an unscaled (A) and a scaled manner (B) for better visibility.

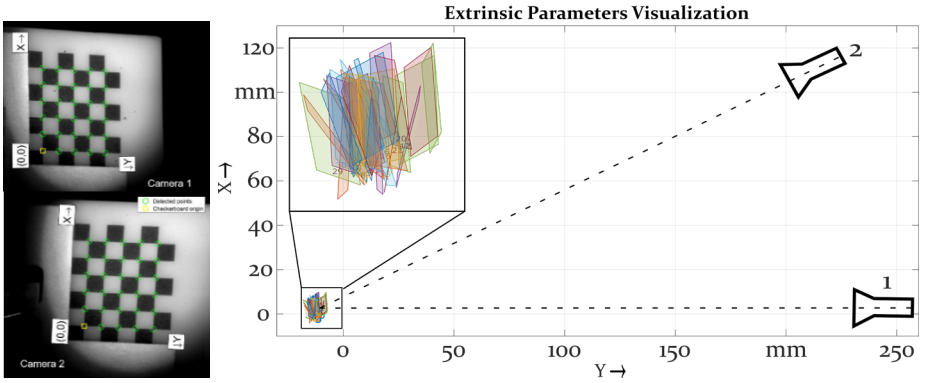

Fig. 37: Detected edges of the checkerboard pattern used for calibration (left) and the visualisation of the extrinsic parameters of the convergent stereo camera system used with the respective detected calibration pattern planes drawn to scale and magnified. [120]

It is of particular importance to cover the entire image plane by moving the calibration pattern, to be able to derive a precise lens distortion model of the optical system composed by the camera and the lens, necessary for subsequent rectification of the high-speed recordings. Since the experiments were carried out in different series, before each series of experiments, a new calibration was carried out as marginal misalignments of the cameras can result in large deviations in the results. After calibration and determination of the camera and lens distortion, the steps for rectification, triangulation and 3D reconstruction can be carried out.

In order to reconstruct the flight trajectory of the braze droplet, the spatial position in x-, y- and z-direction of the droplet must be determined. To achieve this, the images are binarized and rectified. Subsequently, the centre points of the braze droplets are identified sequentially for each frame respective to the time step. The binarization is carried out by applying a threshold value for the left and right image. Subsequently, the centroid of the detected region is calculated to be able to describe the droplet as one discrete coordinate. The respective 2D coordinates of the droplet are subsequently stored in a matrix, from which the 3D coordinates of the braze droplet can be derived by triangulation. After this step, the 3D coordinates of the braze droplet in the camera coordinate system are known for all recorded frames. In order to simplify and unify the evaluation of the flight

trajectory of the droplet, the camera coordinate system is shifted by a coordinate transformation in such a way that its origin corresponds to the orifice location of the capillary. In figure 38, an exemplary droplet flight trajectory is in pseudo 3D. The colour bar indicates the calculated transient velocities for two consecutive time steps with respect to the frame pairs.

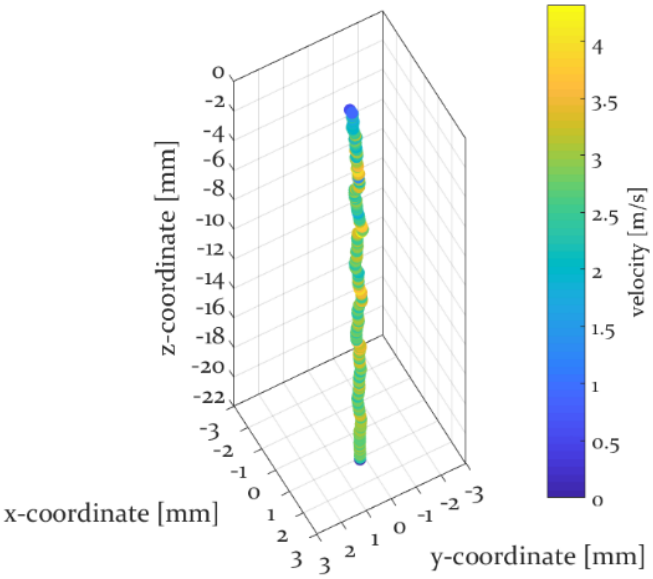

Fig. 38: Exemplary droplet flight in pseudo 3D. P_{Laser} = 120 W; P_{Gas} = 70 hPa, capillary geometry: diffuser type; mean droplet velocity: 2.5 m/s

From the 3D coordinates of the braze droplet during the flight phase, the time resolved and mean droplet velocity, as well as the lateral positional deviation of the droplet position relative to the capillary orifice can be derived as a function of the capillary geometry, the machining head overpressure and the pulse power. For instance, figure 38 indicates the droplet being accelerated after detachment, which is to be attributed to the impulse of the gas molecules emanating from the capillary orifice and therefore accelerating the droplet. This effect is superimposed by the droplet's gravitational acceleration, resulting in a steadily increasing droplet velocity during the flight phase. However, it must be stated that the gravitational acceleration plays a minor role, as the droplet would just reach 0.4 m/s or 18% of the measured velocity after a flight path of 10 mm.

In the experiments, the parameters were varied for P_{Pulse} from 60 to 200 W, in increments of 10 W, whereas the overpressure was varied from 20 to 110 hPa in increments of 10 hPa. First, the complete parameter window in

which droplets can be generated was established for both capillary geometries. Subsequently, an additional set of experiments within the established parameter window was carried out in order to provide information about the statistical significance of the findings. The results of the investigations are discussed in the following sections.

8.3.1 Lateral position deviation

The parameter window was established by gradually increasing both pulse power and overpressure, until droplet atomisation occurred for the first time. Figure 39 shows the effect of droplet atomisation (right) in comparison with the formation of a discrete droplet within the valid parameter window (left). At higher pressures, the gas impulse on the braze melt results in its atomisation when it exceeds the surface tension of the droplet. This effect is thus the reason for the right boundary of the parameter window shown in figures 40, 41, 42 and 43.

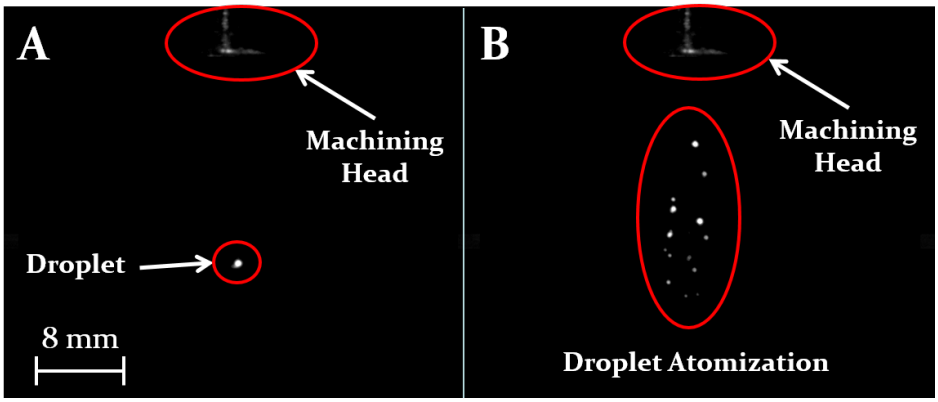

Fig. 39: Freeze frame of two videos. Left: Discrete droplet after detachment from the machining head (conic capillary, P_{Pulse} = 130W; overpressure = 70 hPa). Right: droplet atomisation by exceedingly high overpressure (conic capillary, P_{Pulse} = 130W; overpressure: 110 hPa) [120]

The other boundary of the parameter window is represented by the parameters at which no droplet detachment is observed. This is caused either by applying a pulse power which is insufficient to thoroughly melt the preform, or by applying an overpressure which does not overrule the surface tension holding back the braze melt within the capillary (right and bottom in figures 40, 41, 42 and 43). Subsequently, for the conic capillary, 123 additional measurements were carried out within the valid parameter window for statistical evaluations.

The lateral deviation of the droplet in the x- and y- planes was calculated 1 mm below the capillary orifice using the Euclidean distance in accordance to equation 15. A distance of 1 mm was chosen to ensure consistency, since during the actual joining experiments, the electrode structure is placed 1 mm below the machining head.

$$LD_{z=-1mm} = \sqrt{(x_0 - x_{z=-1mm})^2 + (y_0 - y_{z=-1mm})^2} \tag{15}$$

The area between the discrete measured points was interpolated in figures 40, 41, 42 and 43, using a linear interpolation in order to enhance the comprehensibility of the diagrams. The discrete measured parameter sets are indicated by black dots. Figure 40 shows the lateral position deviation of the droplet 1 mm below the capillary orifice of the conic capillary shape.

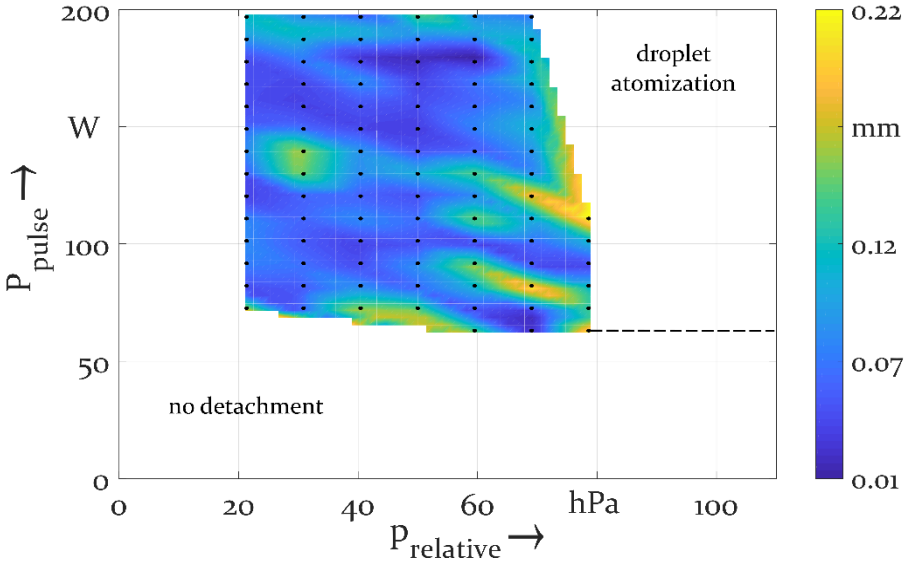

Fig. 40: Results of the stereoscopic evaluation of the lateral position deviation of the droplet at z = 1mm below the capillary orifice for the conic capillary shape [120]

The average lateral positioning deviation for the conic-shaped capillary was found to be 170 µm ± 130 µm (n = 215). The maximum optical output of the beam source represents the upper limit of the investigated parameters. No droplet detachment was observed below 20 hPa at any pulse power, which must be accounted to the fact that the surface tension of the molten droplet inside the capillary exceeds the cumulative force of gravity and gas overpressure and thus prevents droplet detachment as explained in [79]. If the chosen pulse power is below 60 W, no detachment is observed, since the pulse power is insufficient to melt the preform.

In summary, the average lateral position deviation of 170 µm for the conic capillary proved to be sufficient to join 1 x 1 mm electrode structures with Cu wires as shown in [121]. The average lateral displacement of the droplet represents only 17% of the total electrode structure area. The lateral displacement of the droplet should not exceed 30% of the electrode structure's diameter, 300 µm, which is fulfilled for all investigated parameters. In order to be able to compare the capillaries performance, the same procedure was carried out for the diffuser-type capillary. The results are shown in figure 41:

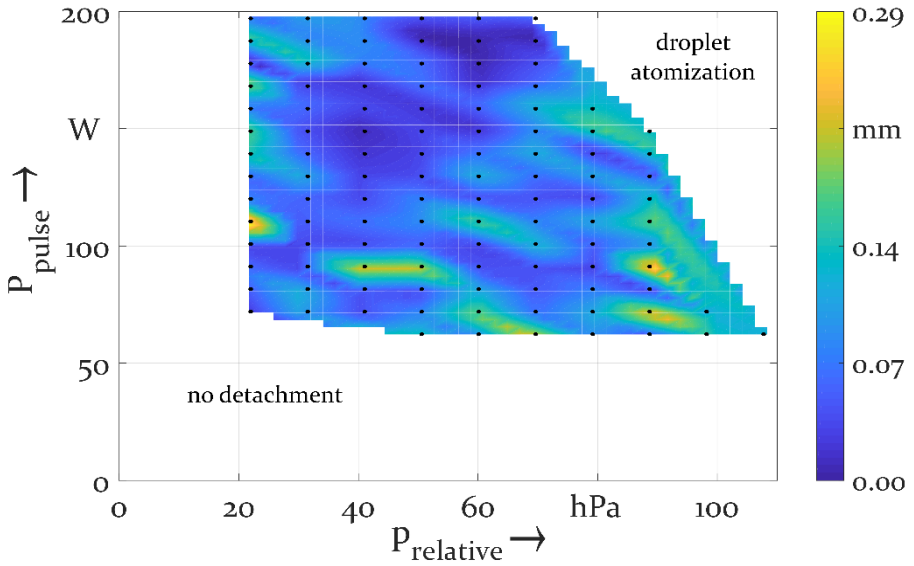

Fig. 41: Results of the stereoscopic evaluation of the lateral position deviation of the droplet at z= 1mm below the capillary orifice for the diffuser-shaped capillary [120]

The number of valid measurements to establish the parameter window were 111. Again, an additional 102 parameter sets were tested for statistical evaluation, resulting in a total number of 213 parameter combinations to be evaluated by stereoscopic high-speed videos for the diffuser type capillary. The average lateral position deviation 1 mm from the capillary orifice was found to be 150 µm ± 120 µm (n = 213). Therefore, the positioning deviation of the conic capillary is 12% higher than the positioning deviation of the diffuser-type capillary. This is particularly remarkable, since the valid parameter window was increased by 21% by replacing the conic with the diffuser-type capillary. Even with this larger parameter window in which joints can be generated at higher pressures, the positioning accuracy of the diffuser-type capillary is yet higher than the positioning accuracy of the

conic-shaped capillary. As droplet atomisation occurs at higher overpressures when comparing the diffuser-type capillary with the conic capillary, a stabilising effect, as indicated by the simulation, was confirmed in the experiment. This must be attributed to the reduced impulse of the gas molecules on the braze droplet after its detachment from the diffuser-type capillary, which was expected and indicated by the numeric model.

8.3.2 Droplet velocity

Not only does stereoscopic image processing enable the tracking of the flight path of the droplet, in three dimensions, it further enables an analysis of how the process parameters influence the droplet's flight velocity. The velocity can be calculated by applying equation 16:

$$v_{Droplet} = \frac{\sqrt{(x_0 - x_{End})^2 + (y_0 - y_{End})^2 + (z_0 - z_{End})^2} \cdot FPS}{n_{Frames}} \tag{16}$$

Whereas x_0, y_0 and z_0 indicate the respective coordinates of the capillary orifice centre and thus the coordinate origin, x_{End}, y_{End} and z_{End} indicate the spatial coordinate of the droplet before escaping the field of view of the cameras. n_{Frames} is the total number of frames in which the droplet is visible to both cameras, and *FPS* indicates the framerate. Using this approach, the mean droplet velocity is obtained, since it integrates the velocity values over the total flight trajectory. The process boundaries are the same, since the same videos as in section 8.3.1 have been evaluated. The results of the investigation for said parameters and capillaries is shown in figure 42.

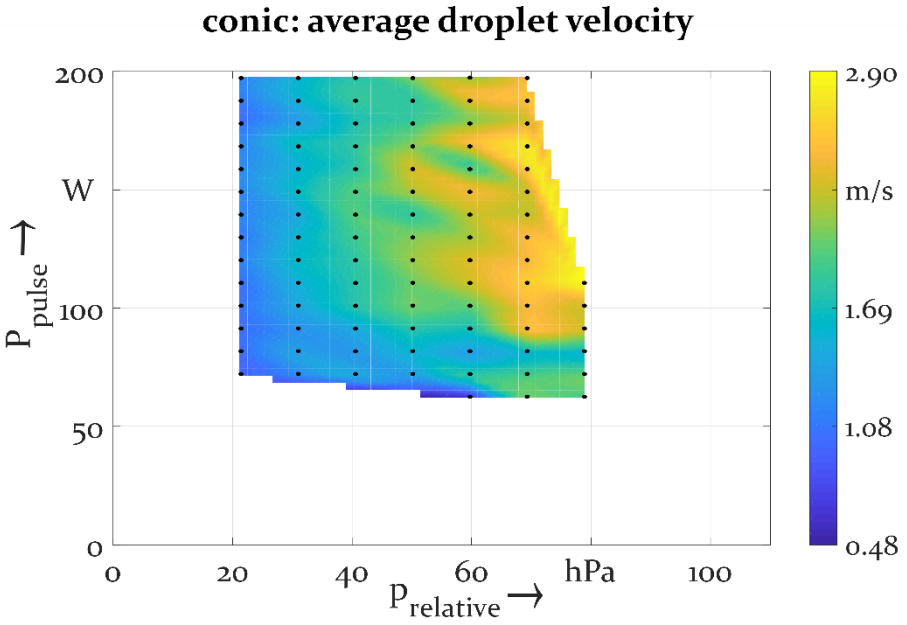

Fig. 42: Results of the stereoscopic evaluation of the average droplet velocity for the conic capillary shape [120]

The average velocity for the conic-shaped capillary was found to be 1.7 ± 0.7 m/s (n = 215). The large standard deviation must be attributed to the fact that a significant braze preform volume and mass deviations occur due to the manufacturing process of the preform, generated by atomisation [121]. This can result in preform porosity as explained in section 5.5. A lower droplet mass thus results in an increased droplet acceleration due to the impulse of the gas molecules on the droplet during the flight phase. Using a polynomial 1 x 1 regression to fit a plane to the measured points, gives the following model, used to describe the influence of pulse power and relative overpressure on the droplet velocity (equation 17):

$$v_{Droplet}(P_{Pulse}, p_{relative}) = 2.4 \cdot 10^{-2} \frac{m}{sW} P_{Pulse} + 4.3 \cdot 10^{-3} \frac{m}{s\ hPa} p_{relative} + 1.2 \cdot 10^{-1} \frac{m}{s} \qquad (17)$$

The coefficient of determination, R^2, of the model is 0.7. Equation 17 indicates that the impact of the machining head overpressure on the droplet's flight velocity is 82% higher than the pulse power's impact. Thus, the pulse power can be chosen in a wide range without altering the droplet's impact velocity, which determines the droplet's and thus the joint's shape to a large extent. These observations thus confirm the result obtained in chapter 7.

Since the simulation indicated a lower gas velocity below the capillary orifice for the diffuser-type capillary than for the conic capillary, the same approach was pursued for the diffuser-shaped capillary. Figure 43 shows the results.

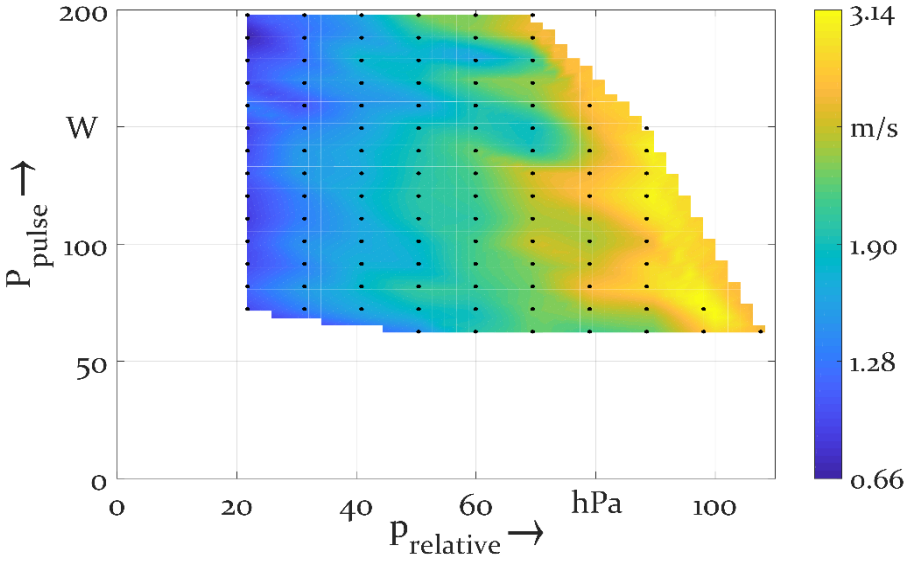

Fig. 43: Results of the stereoscopic evaluation of the average droplet velocity for the diffuser-shaped capillary [120]

The average droplet velocity was found to be 1.8 m/s ± 0.7 (n = 213), which is 7.6% higher than the average velocities obtained with the conic capillary. This is mainly attributed to the rarer occurrence of droplet atomisation at higher gas pressures, which must occur due to the diffusing effect of the capillary geometry on the gas velocity fields (figure 33), as discussed above. Thus, it can be concluded that using the diffuser-shape capillary not only can the positioning accuracy be increased by 13%, but also the parameter window can be increased by 21%. In addition, an 8% higher droplet velocity can be obtained using the diffuser-shaped capillary, without resulting in droplet atomisation. Again, using a polynomial 1 x 1 regression, results in the following analytic description of the influence of pulse power and relative overpressure on the droplet velocity of the diffuser-shaped capillary (equation 18):

$$v_{Droplet}(P_{Pulse}, p_{relative}) = 2.6 \cdot 10^{-2} \frac{m}{s\,W} P_{Pulse} + 1.3 \cdot 10^{-3} \frac{m}{s\,hPa} p_{relative} + 3.7 \cdot 10^{-1} \frac{m}{s} \qquad (18)$$

The coefficient of determination R^2 of the model is 0.88. The model indicates a 95% higher impact of the relative overpressure on the droplet velocity than the pulse power.

In summary, the diffuser-shaped capillary outperforms the conic capillary in every aspect investigated within the scope of this work, as was expected from the CFD simulations. To conclude, the approach pursued of first modelling and simulating a capillary geometry capable of reducing gas flow velocities, then subsequently machining it by means of laser ablation proved to be a suitable measure to enhance both the process parameter window and the positioning accuracy of the braze droplet. The diffusing effect of the altered capillary geometry enables the application of overpressures, which would result in droplet atomisation for the conic-type capillary. Thus, the impact of the gas impulse on the molten droplet dependent on the capillary geometry was successfully quantified for the first time using stereoscopic high-speed imaging. Thus, the hypothesis of stabilizing a droplet of molten copper by first numerically investigating a favourable capillary geometry and subsequently machining it, was proven a suitable approach to obtain a system, tailored to the respective application.

9 Mechanical strength of generated joints

It is of the utmost importance to understand, how changing the alloy composition from the standard SAC solder to a copper based braze influences the joint's mechanical strength, particularly in the scope of a high-volume application of the processes described in chapter 1. Since the CuSn-based braze alloy was, according to the author's best knowledge, never used as filler material in a drop on demand joining process, no information regarding the shear strength of such joints is to be found in the literature. However, the joint's mechanical strength is expected to exceed the shear strength of the standard tin-based solder joints, as the process represents a brazing rather than a soldering process. The numerical results even indicate a temperature domain of the joining process in which a melting of the Ag electrode could be expected, resulting in a partial welding process between the Cu braze and the Ag electrode. If this hypothesis is correct, a failure would occur not in the joint itself, but rather in the ceramic matrix below the Ag electrode structure.

In order to test this hypothesis, braze droplets were deposited on a DuPont LTCC tape CT 2000 with a screen-printed Ag metallisation of 20 µm thickness. This resembles the electrode structure of an LPM-type piezo actuator quite well, and thus it can be determined whether the forces acting on the joints during the Al die casting process will be successfully withstood.

After detaching the droplets onto the Ag electrode structure of the LTCC substrate, the solidified droplets are sheared off using a XYZTEC shear tester Condor 150-3. The system's measurement precision is 0.1% of the absolute value. The velocity of the shear chisel is 5 mm/s. The area $A_{Failure}$ at which failure occurred was measured using an Olympus LEXT OLS4000 3D laser-scanning microscope, and the maximum force at failure F_{Max} was divided for each joint by this area to yield the shear strength τ_{Shear} (equation 19):

$$\tau_{Shear} = \frac{F_{Max}}{A_{Failure}} \tag{19}$$

Particularly in automotive- or aircraft-body applications, structures are exposed to thermal loads with respect to temperature changes during their lifetime. Therefore, it is important to investigate how cyclic thermal loads influence the mechanical properties of the generated joints. In order to evaluate their impact on the mechanical strength, the joints were exposed to thermal cycles according to DIN EN 60068-2-14 (1000 cycles,

-40°C/+125°C, dwell time: 10 minutes, transfer time: 10 seconds). The parameters for joint generation and the procedure of mechanical characterisation were identical as for the reference probe.

Furthermore, since the piezo modules are applied e.g. to achieve active vibration damping, the electrical bonds must endure mechanical loads, induced by mechanical excitation through vibration. In order to evaluate the influence of vibrations on the shear strength, joints were generated and exposed to vibrations using an electrodynamic vibration exciter RMS SW 1512. The technical data of the exciter is listed in table 10:

Table 10: Technical data of electrodynamic vibration exciter RMS SW 1512

Property	Value
Max. vector force (noise)	2.2 kN (effective)
Frequency range	0 – 5000 Hz
Max. amplitude	13 mm
Max. velocity (noise excitation)	3 m/s
Max. acceleration (noise)	169 m/s² (10 kg)

In accordance with the industrial standard DIN EN 60068-3-8, the samples are exposed to effective accelerations $a_{\text{effektive}}$ of 3.9 m/s² applying a noise signal. The excitation was carried out for 8 hours for each available axis (x, y and z). Again, the parameters for joint generation and the procedure of mechanical characterisation were identical as for the reference probe. The results of the experiments are shown in figures 44 and 45, in which the shear strength is plotted over the laser power and the nitrogen overpressure applied to the machining head respectively. This enables the evaluation of the influence of both parameters on the shear force independently.

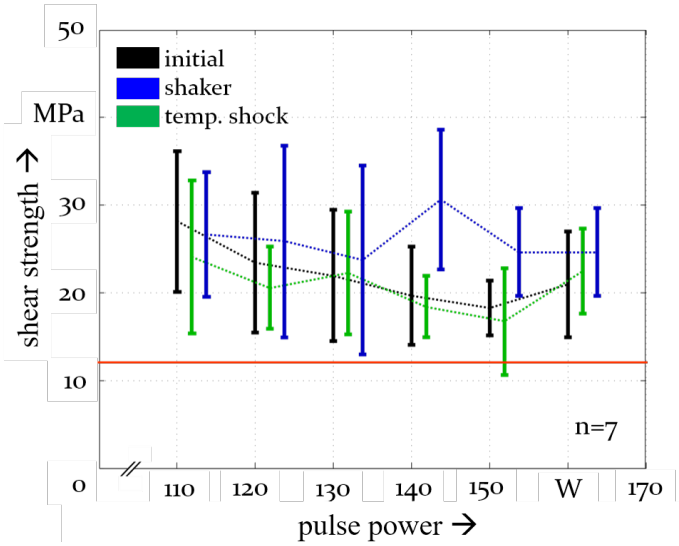

Fig. 44: Influence of laser pulse power on shear strength in the initial state (black), after exposition to acceleration according to DIN EN 60068-3-8 (blue), and after thermal cycle tests according to the industrial standard DIN EN 60068-2-14 (green); (n=7). The red line indicates the shear strength of SAC solder joints with comparable geometry

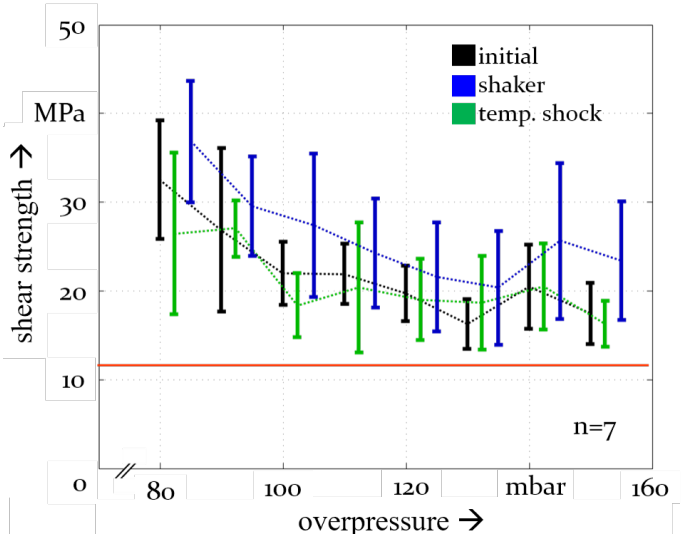

Fig. 45: Influence of capillary overpressure on shear strength in the initial state (black), after exposition to acceleration according to DIN EN 60068-3-8 (blue), and after thermal cycle tests according to the industrial standard DIN EN 60068-2-14 (green); (n = 7). The red line indicates the shear strength of SAC solder joints with comparable geometry

The average shear strength in the initial state was found to be 22 MPa, which exceeds the shear strength of standard Sn–3.5Ag as in

Sn–3.5Ag–0.75Cu solder spheres with a comparable diameter by about a factor of two [122]. By increasing the overpressure from 80 hPa to 150 hPa, the average shear strength is reduced from 33 MPa to 17 MPa. This observation is attributed to the fact that the gas impulse on the solidifying droplet alters its geometry, resulting in a larger bonded area. This is critical due to the shrinkage of the CuSn12 braze which induces stress into the brittle ceramic.

The results of the mechanical characterisation after exposure to thermal shocks seem to confirm the findings of the reference group. They indicate high standard deviations, which must be attributed to the fact that failure occurs in almost all cases in the ceramic, which is obviously the weakest point of the joint. By increasing the pulse power from 110 W to 160 W, the average shear strength is reduced from 24 MPa to 22 MPa. Thus, the influence of the pulse power seems insignificant since it does not have a large influence on the droplet geometry. Contrarily, by increasing the overpressure from 80 hPa to 150 hPa, the average shear strength is reduced from 26 MPa to 16 MPa, which is a reduction of shear strength of 39%. This indicates a significant loss of mechanical strength, the reason for which will be discussed below. The mean value of the shear strength after applying cyclic thermal loads was 21 MPa, with a standard deviation of 5 MPa. In comparison to the initial shear strength this represents a reduction of 7%, which is surprisingly low. Most importantly, it must be stated that thermal cycles do not reduce the joint's mechanical strength significantly. This poses significant advantages over soldered bonds, particularly in high temperature environments.

By increasing the pulse power from 110 W to 160 W the average shear strength after exposure to noise acceleration is reduced from 27 MPa to 25 MPa. Thus, the influence of the pulse power on the resulting shear strength can be considered to be low. The situation changes the overpressure is increased from 80 hPa to 150 hPa. Again, the average shear strength is reduced significantly from 37 MPa to 23 MPa. Thus, the influence of the overpressure on the resulting shear strength is again significant. The mean value of the shear strength after the mechanical vibration test was 26 MPa with a standard deviation of 7 MPa. In comparison with the initial shear strength, the shear strength was increased by 17%. The increasing shear strength can be explained only by the relatively large standard deviation of the absolute measurement of shear strengths. Yet, a negative influence of accelerations due to vibrations cannot be concluded from the experimental results, thus the joining method developed seems particularly suited for

applications such as active vibration damping of structural lightweight components.

The requirements formulated in chapter 1 and the objectives derived from chapter 2 require a firm joint on a 20 µm thin sintered Ag-electrode structure, which makes the selection of a suitable braze material a critical step. Hence, the braze alloy chosen was CuSn12, as it is able to form AgSn-rich phases if Ag is present. This results was expected to result in a diffusion layer between the Ag pad and the braze material and hence in a metallurgical bond between the Cu wire and the Ag electrode (for details, see section 4.1). This hypothesis was proven by element sensitive EDX-mappings of a joint cross section. Figure 46 shows EDX mappings of Cu precipitations forming during cooling, resulting in a formation of AgSn-rich phases at the interface between the Ag structure and the braze material. As predicted, the melt forms a AgSn rich phase during cooling and Cu-precipitation, which firmly bonds the braze alloy to the Ag-electrode.

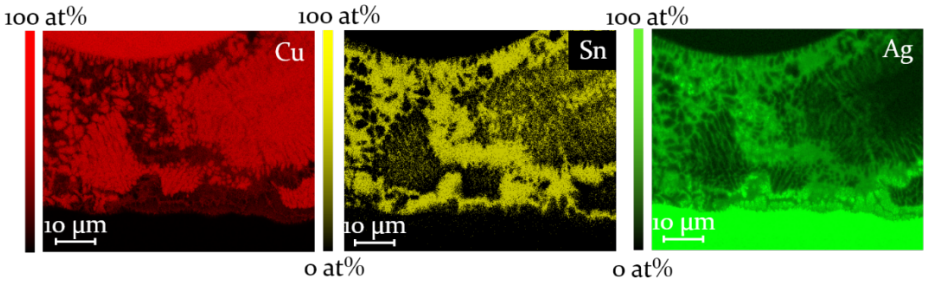

Fig. 46: Cu precipitations forming during cooling, resulting in a formation of AgSn-rich phases at the interface between the Ag structure and the braze material

Since the joint's mechanical strength exceeds the mechanical strength of the LTCC substrate, characteristic, shell shaped craters form within the substrate after the joint is sheared off the Ag electrode. Figure 47 shows a pseudo three-dimensional visualisation of the ceramic after shear testing. The crater exhibits a depth of 170 µm.

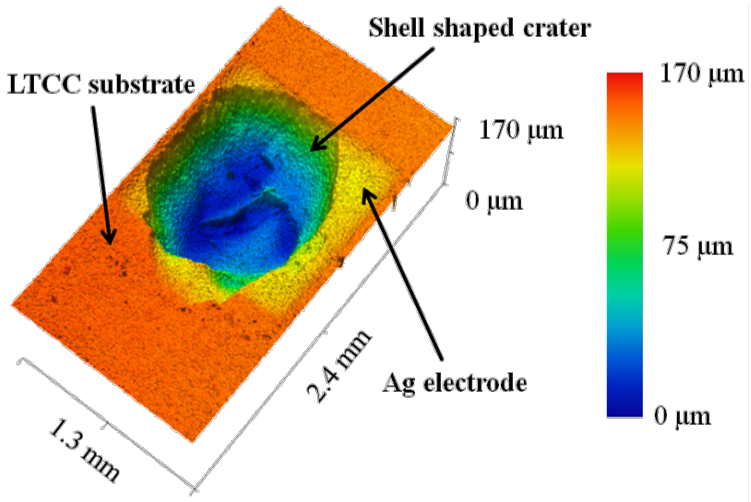

Fig. 47: Topography of a crater in the LTCC substrate after shear testing; the Ag electrode was partially removed during shear testing.

The failures of the LTCC matrix can be explained by its inherent brittleness, which makes the ceramic the most critical material for obtaining reliable joints [123]. In addition, the difference between ceramic's and metal's thermal expansion coefficients (CTE) leads to a build up of residual thermal stresses as the braze material cools to room temperature. This reduces the joint strength as is known from literature [124]. Thus, the thermal stress during cooling and shrinkage of the filler material, in combination with the high elastic module and low-relaxation characteristics of the ceramic substrate, results in residual stresses at the joining area. This effect is dominant, particularly between the Ag electrode and the LTCC due to the ductile behaviour of the Ag pad, which cannot buffer the shear forces that occur during shrinkage of the braze filler material. The Ag pad translates said residual stress into the brittle LTCC matrix, resulting in microscopic shell shaped cracks in the ceramic, particularly at the outer circumference of the bonded interface. In order to prove this hypothesis, figure 48 shows a cross-section of a joint at the interface between the braze and the LTCC ceramic. Exactly at the edge of the Ag interface, which is exposed to the highest shear strength during cooling and solidifying of the braze, a characteristic micro crack forms (highlighted by the dashed line in figure 48).

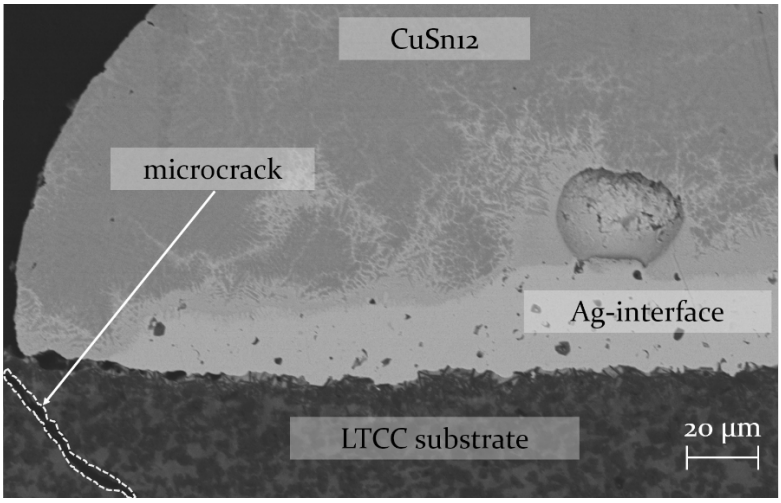

Fig. 48: SEM image of joint cross section with a micro crack (substrate: DuPont 951 PX LTCC tape, 20 µm screen-printed Ag metallisation; Mag. 1.55 K).

With the increasing aspect ratio of the droplet, determined by the inert gas overpressure, the likelihood of such cracks increases, since a larger area is wetted by the droplet. If the droplet is flattened due to the momentum of the gas jet, as the braze spreads over a larger area fraction of the electrode, the mechanical stress during its cooling and thus shrinkage increases. This stress acts on the Ag electrode and the ceramic substrate and increases the chance of the formation of micro cracks within the brittle ceramic. This effect is thus believed to explain the joint's reduction in mechanical strength at elevated inert gas overpressures. Regardless, the generated joints exceed the shear strength of tin-based solder joints with a comparable contact area by at least a factor of two. Furthermore, the joints do not show significant degeneration after exposure to vibrations and cyclic thermal loads. The requirements formulated in chapter 1 and the objectives derived from the deficits of the state of the art in chapter 3 are thus fulfilled by the developed process. The initial hypothesis was confirmed by the experiment since a partial welding between the electrode and the braze material was observed see figure 46 and figure 48.

10 Analytic model of the process energy balance

The yield losses of laser-based processes due to energy dissipation by convection, radiation and conduction are notoriously difficult to measure. Consequently a straight forward approach to quantify those energy losses would be of value to the scientific community. The developed LDJ process is particularly suitable to establish such a model, since the volume of material to be molten is precisely defined. In addition, the period from the beginning of the laser pulse throughout the melting of the braze volume can be measured with a with high temporal resolution in the regime of milliseconds. This distinguishes the developed process e.g. from laser beam welding or soldering, and provides promising boundary conditions for such an undertaking.

To establish a model capable of analytically describing energy losses of laser-based processes, first the material properties of the braze material as well as the preform's mass must be quantified as precisely as possible. To obtain the CuSn sphere's average mass, a total number of 100 spheres were measured using a precision balance Mettler Toledo XD105 DualRange, with a minimum measuring limit of 0.01 mg. The average mass was found to be 1.15 mg, with a standard deviation of 0.11 mg, which represents 9.6% of the absolute value.

One of the dominant reasons for energy and thus yield loss of laser-based processes, is the comparably low absorptance of metals to infrared laser radiation. To determine the accuracy of the model, the absorption of the investigated material must first be determined conventionally. This was carried out using an Ulbricht sphere setup as shown schematically in figure 49:

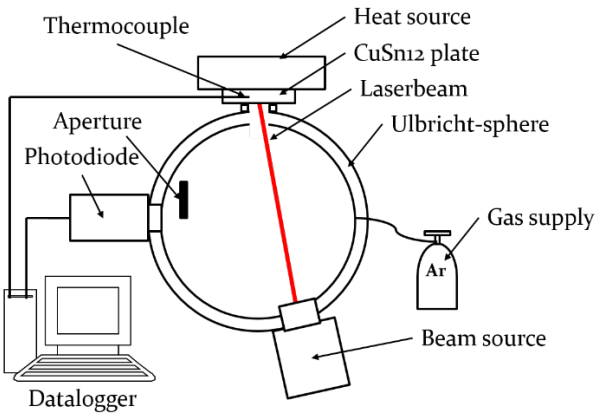

Fig. 49: Schematic of the modified Ulbricht sphere setup for laser radiation with an inert gas supply and the heating of the work piece [125]

Since an important factor influencing the absorptance α of metals is the temperature, the setup described is capable of measuring the absorptivity of the material in dependence of the material's temperature, up to 700 K. The specimen used was a polished bar of CuSn12 with a roughness R_a of 0.0548 ± 0.006 µm, and R_z of 0.525 µm ± 0.062 µm (n=10). The roughness was measured using an Olympus LEXT OLS4000 laser-scanning microscope. The wavelength of the beam source used was 1064 nm. The results of the absorptance measurements are shown in figure 50.

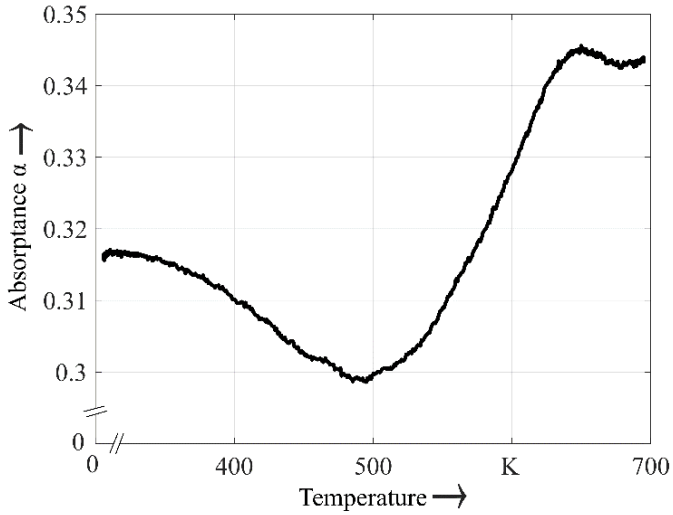

Fig. 50: Temperature-dependent absorptance at λ = 1064 nm of a polished CuSn12 specimen, using argon shielding to prevent oxidation during heating [125]

The results indicate an absorptance of the CuSn12 surface between 29% at 500 K and 35% at 700 K, with a mean value of 32%.

As a boundary condition for establishing an analytical process model, it is assumed that a constant amount of energy is necessary to heat a braze sphere of a certain mass up to the liquidus temperature T_{Liquid}. It is further assumed that braze detachment and thus the detection of the scattered laser radiation occurs instantaneously after the braze sphere is heated to T_{Liquid}. This is not entirely correct, since there is a small delay between the complete melting of the braze preform and its detachment from the capillary. However, highspeed videos showed that this time domain is short in comparison to the overall time period necessary to melt the preform. Thus the error induced by this assumption is in the range of about 5%.

Further, it is assumed that the cumulative energy E_0 to melt the braze sphere is the sum of the caloric energy $E_{\Delta T}$ necessary to heat the preform to the liquidus temperature and the fusion energy E_{Fus} necessary for the phase transition from a solid to a liquid state (equation 20):

$$E_0 = E_{\Delta T} + E_{Fus} \tag{20}$$

The hypothesis further assumes that the caloric energy necessary to heat the braze droplet to liquidus temperature can be calculated by applying equation 21, where c_p refers to the specific heat capacity, m to the average mass of the braze sphere and ΔT to the temperature difference between the room and liquidus temperatures:

$$E_{\Delta T} = c_p \, m \left(\Delta T_{room-liquid} \right) \tag{21}$$

The specific heat capacity shows the strongest temperature dependence of all said material properties. Since no temperature-dependent values of the specific heat capacity of CuSn12 are available in the literature, values of Cu were taken from [126] and are plotted in figure 51:

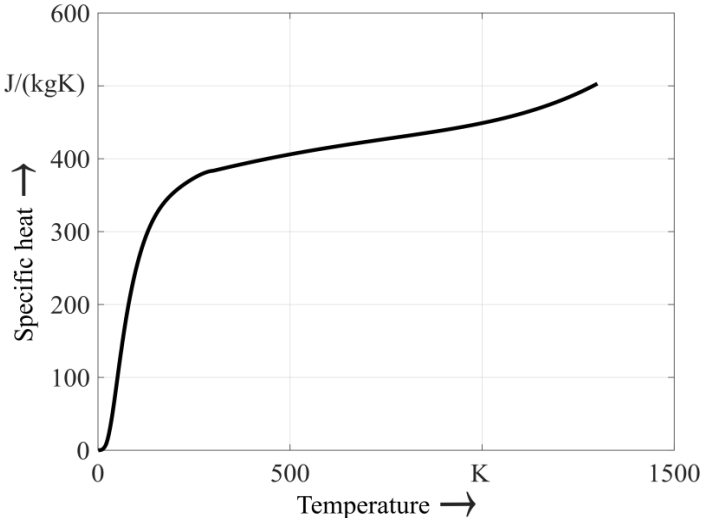

Fig. 51: Temperature-dependent specific heat capacity of Cu according to [126]

Subsequently, the mean value of the specific heat capacity of Cu between room temperature T_{Room} and liquidus temperature T_{Liquid} was calculated using equation 22:

$$c_p(T) = \frac{1}{T_{Liquid} - T_{Room}} \int_{T_{Room}}^{T_{Liquid}} c_p(T)\, dT = 433\ \frac{J}{kgK} \tag{22}$$

The caloric energy to heat the braze spheres to T_{Liquid} can subsequently be calculated, applying equation 23:

$$E_{\Delta T} = m \int_{T_{Room}}^{T_{Liquid}} c_p(T)\, dT = 433\ \frac{J}{kgK} \tag{23}$$

A braze preform's mass of 1.15 mg was assumed, as measured in section 5.5. In addition, the fusion energy necessary for the phase transition from solid to liquid E_{Fus} must be taken into consideration. It is calculated in accordance to equation 24, in which H_f refers to the enthalpy of fusion:

$$E_{Fus} = H_f \cdot m = 0.1J \tag{24}$$

In this model, the minimum amount of energy necessary to melt the braze sphere is the sum of the caloric and the fusion energy E_0 (equation 25):

$$E_0 = E_{Fus} + E_{\Delta T} = 0.5J \tag{25}$$

In an ideal process with an absorptance of the braze preform of $\alpha = 1$ or 100%, and no thermal energy loss by heat convection, conduction and radiation, a laser pulse with an energy E_0 would deposit precisely the thermal energy necessary to heat the braze preform from T_{Room} to T_{Liquid}. As stated earlier, several effects result in energy losses, the most prominent of which is the low absorptance α of metallic surfaces. In addition, energy losses due to dissipating thermal energy by heat convection, conduction and irradiation do occur. These losses are aggregated by introducing the term E_{Loss}. It represents the factor of pulse duration t_{Pulse} during which a certain amount of power dissipation P_{Loss} occurs. The analytic model (equation 26) describing the process can thus be written as:

$$E_0 = t_{Pulse} \cdot \alpha \cdot P_{Pulse} - E_{Loss} = t_{Pulse}(\alpha \cdot P_{Pulse} - P_{Loss}) \tag{26}$$

In equation 26, E_0 represents the calculated cumulative energy necessary to melt the braze sphere, and t_{Pulse} represents the pulse duration after which the laser emission is interrupted. The analytic model assumes t_{Pulse} to be the exact duration from the start of the laser irradiation and the detachment of the braze preform, since the pulse will be interrupted by the process control implemented within less than 2 ms, which is almost instantaneous after droplet detachment. P_{Pulse} denotes the pulse power, which is multiplied with the absorptance α, since only the absorbed fraction of the laser radiation can be attributed to the heating of the braze sphere. P_{Loss} represents the power dissipation by heat convection, conduction into the capillary, and heat radiation. A simplification must be assumed here, since the analytic model incorporates energy losses only within the pulse duration t_{Pulse}, omitting any thermal energy losses after the laser pulse is interrupted, after droplet detachment. An evaluation of the influence of the laser pulse power on the droplet detachment was carried out by evaluating the photodiode signal, as described in section 6.2, in order to determine the precise times at which the braze detachment occurs. Since the pulse is instantaneously interrupted after braze detachment, the period between the beginning of the laser pulse and droplet detachment is equal to the pulse duration t_{Pulse}. Depending on the laser power selected, t_{Pulse} varies between 100 and 30 ms. The results of the measurements and the curve obtained by the analytic model (dashed line) are shown in figure 52.

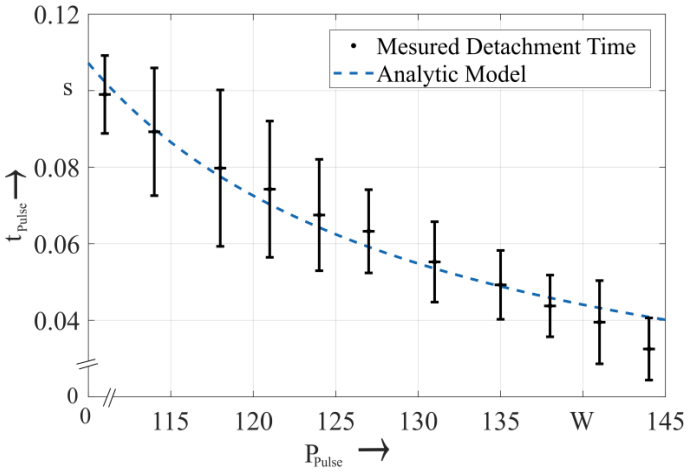

Fig. 52: Braze detachment time over pulse power with respective fit (n=5) [125]

The standard deviations of the measured points must be attributed to the braze sphere mass deviations, which require different pulse durations to thoroughly melt the braze sphere. In order to gain P_{Loss} and α analytically equation 27 was rewritten:

$$t_{Pulse} = \frac{E_0}{(a \cdot P_{Pulse} - P_{loss})} \tag{27}$$

After approximating equation 27 to the measured points, using the coefficients P_{Loss} and α as degrees of freedom and applying the sum of the least squares regression method, we gain $\alpha = 0.23$ and $P_{Loss} = 20$ W. The measured absorptance using the Ulbricht sphere setup and the absorptance estimated by the regression of the analytic model to the measured detachment times, shows surprisingly good accordance given the different approaches to quantify α. The deviation of 28% in both measurements can be attributed to several effects:

- The absorptance of CuSn12 was measured in a temperature range between room temperature and 425°C using the Ulbricht sphere setup, thus no measured absorptance at higher temperatures are available. However, according to the literature, it is unlikely that absorptance drops significantly with increasing temperatures [96; 97].
- Since no temperature-dependent values for CuSn12 were available in literature, the temperature-dependent specific heat capacity was taken from Cu, which might also introduce a rather small systematic error.

- Droplet detachment does not occur instantaneously after complete melting of the braze preform, but after a certain small delay as stated earlier.

The analytic model indicates, that reducing the pulse power from 144 W to 111 W results in an increased thermal energy loss from 0.7 J to 2 J. This is particularly interesting, since the total energy necessary to melt the preform to T_{Liquid} is just 0.5 J (see equation 25). Thus, reducing the pulse power by 23%, increases the cumulative thermal energy loss by 200%. This is a significant reduction in process efficiency.

In addition, the energy loss by heat conduction, radiation and convection E_{Loss}, exceeds the energy necessary to heat the braze preform to T_{Liquid} by magnitudes if low pulse powers are chosen. The model also indicates, that at a pulse power of 111 W the droplet detaches after 0.097 s, which is equal to a pulse energy of 10.8 J. Of this energy, only 23% are absorbed and hence available to thermalise and melt the braze sphere. Of this fraction, 2.02 J of thermal energy are dissipated from the braze sphere by heat convection, radiation and conduction, leaving only 0.5 J or 18% of the deposited thermal energy to contribute to the heating of the braze preform, which is a strikingly low fraction. With the proposed method, it seems feasible to quantify the energy balance of many laser-based processes. However, this is not yet a well-understood field due to the lack of quantitative measurement approaches. In addition, the obtained values might be relevant in the future to further improve e.g. the energy efficiency of laser-based additive manufacturing processes. It must be stated, that the model must not be utilised for ultra-short pulse (USP) laser processes, since a throughout thermalisation of the irradiated sample is assumed. This represents an impermissible generalisation for USP-processes.

11 Synopsis

In the scope of this work, a novel joining process was developed and investigated from both an application-driven and an academic point of view. The process utilises laser radiation to melt a CuSn-braze preform, which is subsequently detached from a ceramic capillary via inert gas overpressure. After a flight phase, the braze droplet impinges on the joining interface and wets the joining partners where it forms a metallurgical bond after solidification. This process is referred to as laser drop on demand joining (LDJ). Figure 53 shows the LDJ development process with the most important dependencies indicated by arrows.

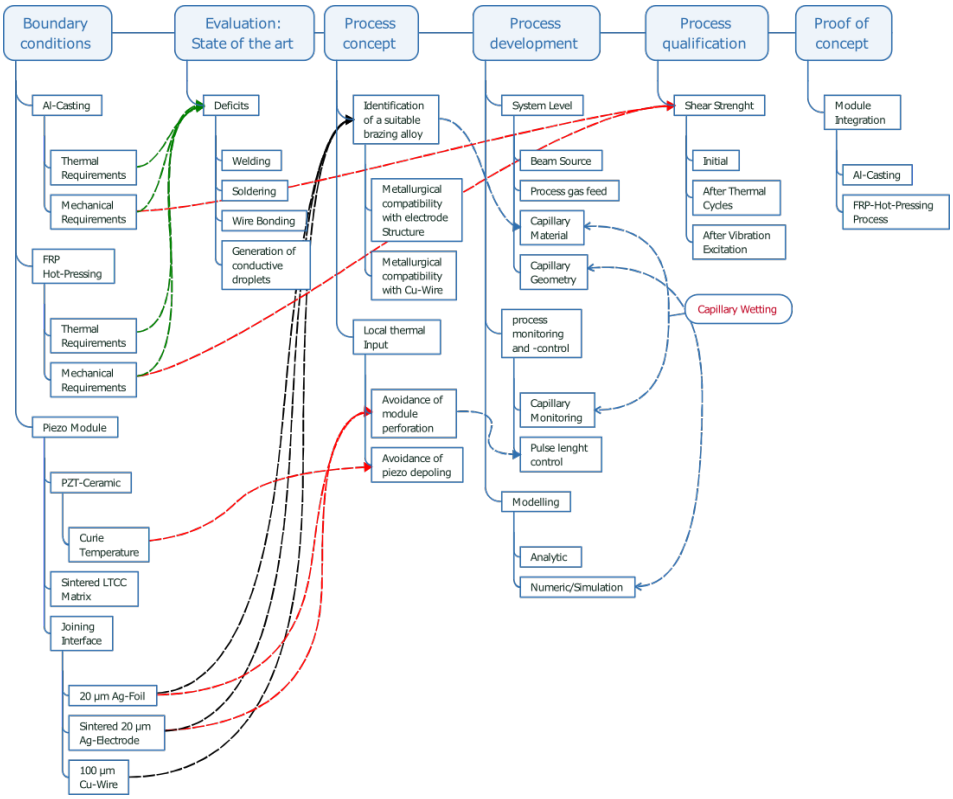

Fig. 53: Flow chart of the LDJ development process with each step's respective dependencies

The process was particularly tailored to generated joints withstanding an Al casting process and a hot-pressing process, both of which are processes proposed to integrate piezo modules into active lightweight structures. During casting, the joint is exposed to a liquid aluminium melt of about 700°C [121], where the melt applies a pressure of 12 MPa onto the joint. In

contrast, the hot-pressing process exhibits a tool temperature of 240°C and a force of 0.05 MPa, both of which are applied for ten minutes during the FRP structure's consolidation. Both integration processes are withstood by the joints generated by LDJ without impairing the piezo module's functionality, however, in order not to exceed the scope of this work, the author refers to [121] and [127] for more details on the investigations of the respective integration processes.

It was shown, that the shear strength of the joints exceeds the strength of standard tin-based solders by a factor of two, regardless of whether the joints were in their initial condition or exposed to temperature shocks or vibration excitation. Thus the requirements formulated in chapter 1 and the objectives derived from those in chapter 3, both are fulfilled by the developed process.

To gain an understanding, process dynamics simulations were carried out to determine a favourable capillary geometry. Subsequently a capillary with a tailored shape was machined by means of USP laser ablation. To quantify the impact of the capillary geometry on the droplet's positioning accuracy and flight velocity, as well as the overall process window, stereoscopic high-speed videos were recorded and evaluated. The experimental results confirmed the results obtained by the fluid dynamic simulation. The modified capillary geometry enabled an increase of the parameter window by 20.7%. In conclusion, the approach pursued, first modelling and simulating optimised capillary geometries and subsequently machining such capillaries by means of laser ablation, proved to be a suitable measure to enhance both the process parameter window and the positioning accuracy of the braze droplet on the electrode surface. The impact of the gas impulse on a molten droplet of a copper-base alloy in dependence of the capillary geometry was successfully quantified for the first time within the scope of this work using stereoscopic high-speed imaging.

In addition, the simulation predicts significant thermal loads during joining. To evaluate capillary performance over an extended number of joining cycles, a machine vision algorithm was developed to monitor the development of braze residues within the capillary, and to determine capillary failure due to the adhesion of the braze material or the formation of thermally induced cracks. However, within 2000 consecutive experiments the capillary did not show any signs of thermal breakdown.

The developed process has interesting properties, not only from an engineering but also from an academic perspective. By measuring the precise

period between the beginning of the laser pulse until the droplet's detachment, the setup can be utilised not only to quantify energy balances of laser-based processes, but also to quantify the absorptance of a given alloy indirectly by measuring the pulse duration until the melt droplet detaches from the machining head. It was found that decreasing the pulse power by 23%, results in an increase of cumulative thermal energy loss by heat dissipation of more than 200%. Those losses are driven by convection, conduction and irradiation. This observation is interesting, since particularly at low pulse powers the loss of thermal energy by dissipation are overruling the effect of the materials comparably low reflectivity. The analytic model yielded an absorptance of 28%, which matches the reference value of 32% obtained using an Ulbricht sphere setup surprisingly well, given the fact that the value was obtained simply by measuring the laser pulse duration until droplet detachment. Since thermal energy dissipation and yield losses due to metals' low absorptivity are crucial factors for many laser-based processes, and since those are notoriously difficult to quantify, the described approach could be utilised in future to characterise other metals relevant e.g. for laser beam welding or laser-based additive manufacturing processes.

12 Summary and outlook

The laser drop on demand joining process, as discussed in the scope of this work, was developed and tailored to perform a unique and complex task. However, the process is not necessarily limited to this application since an application in many other fields seems to be a plausible scenario as well, for example, enhancing the yield of thermoelectric power generators. Such generators are utilised to generate energy from temperature gradients by means of the Peltier effect. Since the efficiency of such generators depends essentially on the temperature gradient between the n and p layers of the module, in the majority of such cases, the maximum operating temperatures of such elements is restricted to approximately 200°C [128], since the soldered interconnections would degenerate at higher temperatures. Substituting a low melting solder alloy with a high melting Cu-based braze material would enable the ability to apply higher temperatures to the module, and thus to increase its yield and enable the application in high temperature environments, such as rocket engines [129].

In addition, the developed joining method could also be used in an area of the electronics industry with particularly high temperature requirements, including "harsh environments" e.g. of deep drilling heads. Such electronic devices can be exposed to temperatures above 200°C, and thus require a joining technology that can provide thermal stability and mechanical robustness, which is not often able to be provided by conventional soldered contacts.

Aside from these possible applications, the process could be applied to print three-dimensional structures, with the capability to generate an application-driven tailored alloy composition, since each preform can potentially consist of a different metal or alloy. This would enable a tailored modification of the structure's properties, including hardness, stiffness, corrosion resistance and elastic modulus within a single structure or component in accordance with the locally prevailing requirement profiles.

13 Zusammenfassung und Ausblick

Im Rahmen dieser Arbeit wurde ein neuartiger Fügeprozess entwickelt und sowohl aus anwendungsorientierter als auch aus wissenschaftlicher Sicht untersucht. Bei diesem Verfahren wird mittels Laserstrahlung ein CuSn-Lötformteil aufgeschmolzen, und anschließend mittels Inertgasüberdruck aus einer keramischen Kapillare ausgetrieben. Nach einer Flugphase trifft der Löttropfen auf die Fügefläche und benetzt die Fügepartner, wo er nach der Erstarrung eine metallurgische Verbindung bildet. Dieser Prozess wird als Laser Drop on Demand Joining (LDJ) bezeichnet. Abb. 54 zeigt den LDJ-Entwicklungsprozess mit den wichtigsten Abhängigkeiten, die als Pfeile gekennzeichnet sind.

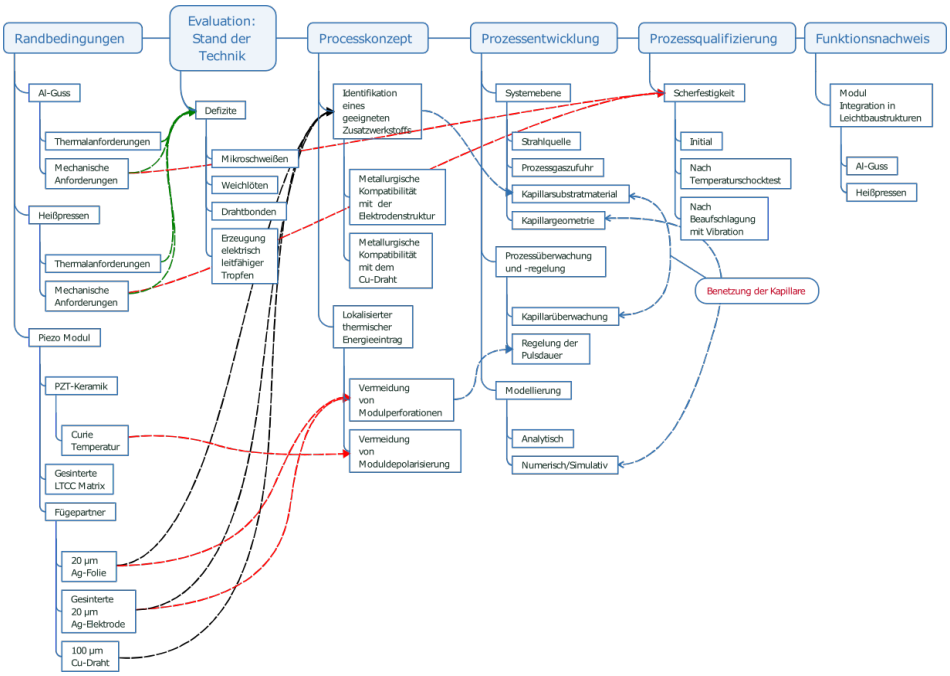

Fig. 54: Ablaufdiagramm des LDJ-Entwicklungsprozesses mit den jeweiligen Abhängigkeiten

Das Verfahren wurde speziell auf die Erzeugung von Fügeverbindungen zugeschnitten, um die Lastkollektive, die beim Al-Gussverfahren dem Heißpressverfahren auf die elektrischen Kontakte wirken standzuhalten. Beide Verfahren werden dabei zur Integration von Piezomodulen in aktive Leichtbaustrukturen diskutiert. Während des Gießens wird die Verbindung der flüssigen Aluminiumschmelze von ca. 700°C [121] ausgesetzt,

während diese einen Druck von 12 MPa auf die Fügeverbindung ausübt. Im Gegensatz dazu weist der Heißpressprozess eine Werkzeugtemperatur von 240°C und eine Kraft von 0,05 MPa auf, welche während der Konsolidierung der Faserverbundstruktur zehn Minuten lang auf die Fügestelle einwirken. Die mittels des LDJ-Prozesses erzeugten elektronischen Kontaktierungen überstehen dabei beide Integrationsprozesse, ohne dass der Fügeprozess selbst die Funktionalität der Piezomodule beeinträchtigen würde. Um den Umfang dieser Arbeit nicht zu überschreiten, verweist der Autor für weitere Details zu den jeweiligen Integrationsprozessketten auf [121] und [127].

Zudem konnte gezeigt werden, dass die Scherfestigkeit der Verbindungen die Festigkeit von Standardloten auf Zinnbasis um den Faktor zwei übersteigt. Dabei ist es irrelevant, ob die Verbindungen im Ausgangszustand vorliegt oder mit Temperaturschocks oder Vibrationsanregungen vorbelastet wurde. Somit werden alle in Kapitel 3 an einen geeigneten Fügeprozess formulierten Anforderungen erfüllt.

Des Weiteren wurden, um eine günstige Kapillargeometrie zu identifizieren, mit der sich die prozessinhärente Dynamik positiv beeinflussen lässt Simulationen durchgeführt. Die numerisch gewonnenen Erkenntnisse wurden anschließend genutzt, um eine optimierte Kapillargeometrie mittels Ultrakurzpuls-Laserablation herzustellen. Um den Einfluss der optimierten Kapillargeometrie auf die Tropfenpositioniergenauigkeit und Fluggeschwindigkeit des Schmelzetropfens sowie auf die Tropfenintegrität zu quantifizieren, wurden stereoskopische Hochgeschwindigkeitsvideos aufgenommen und ausgewertet. Die dabei generierten dreidimensionalen Flugbahninformationen bestätigten die Ergebnisse der strömungsmechanischen Simulation. Durch die modifizierte Kapillargeometrie konnte das Parameterfenster um 20,7% vergrößert werden. Somit erwies sich der verfolgte Ansatz der numerischen Analyse optimierter Kapillargeometrien und deren anschließenden Herstellung mittels Laserablation als geeignete Maßnahme, um sowohl das Prozessparameterfenster als auch die Positioniergenauigkeit des Löttropfens auf der Elektrodenoberfläche zu verbessern. Der Einfluss des Gasimpulses auf einen Tropfen einer geschmolzenen Kupferbasislegierung in Abhängigkeit von der Kapillargeometrie wurde im Rahmen dieser Arbeit erstmals mit stereoskopischen Hochgeschwindigkeitsbildern erfolgreich quantifiziert.

Darüber hinaus prognostiziert die Simulation signifikante thermische Belastungen der Kapillare während der Ablösung des Schmelzetropfens. Zur

automatisierten Beurteilung der Kapillarstandzeit auch bei größeren Zyklenzahlen wurde ein Bildverarbeitungsalgorithmus entwickelt, der die Anhaftung und Agglomeration von Lötrückständen innerhalb der Kapillare überwacht und somit einen Indikator für ein Kapillarversagen bereitstellt. Dabei wurde während 2000 aufeinanderfolgenden Experimenten keine Anzeichen einer thermischen Schädigung der Kapillare identifiziert.

Darüber hinaus hat der entwickelte Prozess nicht nur aus ingenieurwissenschaftlicher, sondern auch aus akademischer Sicht einige interessante Aspekte. Durch die Messung des genauen Zeitraums zwischen dem Beginn des Laserpulses und der Ablösung des Tropfens von der Kapillare kann das System auch zur Quantifizierung der Energiebilanzen von laserbasierten Prozessen verwendet werden. Darüber hinaus lässt sich mit dem Versuchsaufbau auch eine indirekte Quantifizierung der Absorption einer Metalllegierung realisieren. Dazu ist einzig die Messung der Pulsdauer, also der Dauer von Beginn der Bestrahlung bis zur Ablösung des Lottropfens von der Kapillare, notwendig. Es wurde dabei im Rahmen der Untersuchungen festgestellt, dass eine Verringerung der Pulsleistung um 23% zu einer Erhöhung des kumulierten thermischen Energieverlustes um mehr als 200% führt. Diese Verluste umfassen dabei thermische Energieverluste durch Konvektion, Wärmeleitung und -strahlung. Diese Beobachtung ist insbesondere deshalb interessant, da bereits bei vergleichsweise geringer Reduktion der Pulsleistung der Verlust von Wärmeenergie durch oben genannte Effekte den Einfluss der hohen Reflektivität von Cu-Basis Legierungen bereits zu dominieren scheint. Das entwickelte analytische Modell ergab dabei für die untersuchte Legierung eine Absorption von 28%. Der mittels Ulbrichtkugel gemessene Referenzwert betrug 32%, was eine überraschend hohe Korrelation darstellt, insbesondere wenn man berücksichtigt, dass der Wert der Absorption indirekt durch eine Messung der Laserpulsdauer erfolgt ist. Da die Prozesseffizienz letztendlich durch Energieverluste sowohl bei der Energieeinkoppelung in die Oberfläche als auch durch Wärmeleitungseffekte definiert wird ist es denkbar, dass dieser Ansatz in Zukunft für viele laserbasierte Prozesse zur Optimierung und Effizienzsteigerung genutzt werden kann um beispielsweise Metalle zu charakterisieren, die für das Laserstrahlschweißen oder laserbasierte additive Fertigungsprozesse relevant sind.

14 Bibliography

[1] Apostolos, F., Alexios, P., Georgios, P., Panagiotis, S., and George, C., "Energy efficiency of manufacturing processes: a critical review", *Forty Sixth CIRP Conference on Manufacturing Systems 2013*, Vol. 7 (2013): 628–633.

[2] O'Brien, C., "Sustainable production – a new paradigm for a new millennium", *International Journal of Production Economics*, Volumes 60-61 (1999): 1–7.

[3] Klein, B., *Leichtbau-Konstruktion,* 10th ed. Wiesbaden, Germany: Springer Vieweg, 2013.

[4] Neugebauer, R., ed., *Energieeffiziente Produkt- und Prozessinnovationen in der Produktionstechnik.* Auerbach, Germany: Verl. Wiss. Scripten, 2010.

[5] Siebenpfeiffer, W., *Leichtbau-Technologien im Automobilbau.* Wiesbaden, Germany: Springer Vieweg, 2014.

[6] Hufenbach, W.A., Gude, M., Heber, M., Weber, T., Schmidt, M., and Held, C., *Proceedings of CRC/Transregio 39* (Nuremberg, Germany, 2013).

[7] Friedrich, H.E., *Leichtbau in der Fahrzeugtechnik.* Wiesbaden, Germany: Springer Vieweg, 2013.

[8] Hau, E., *Windkraftanlagen,* 4th ed. Berlin, Germany: Springer, 2008.

[9] Stauber, R., "Werkstoffe und Technologien für Den Automobil Leichtbau", in: *Verbundwerkstoffe.* Wiley-VCH, 2009: 12–26.

[10] Koko, T.S., Akpan, U.O., Berry, A., Masson, P., Besslin, O., Szabo, J., and Sponagle, N., "Vibration Control in Ship Structures", *Encyclopedia of Smart Materials.* John Wiley & Sons, Inc, 2002.

[11] Härter, S., Franke, J., and Beer, D., "Untersuchung des Selbstzentriereffektes mittels AOI zur gesicherten Verarbeitung von 01005-Bauelementen", *Plus*, Vol. 3 (2015): 567–573.

[12] Irschik, H., Krommer, M., and Vetyukov, Y., "On the Use of Piezo electric Sensors in Structural Mechanics: Some Novel Strategies", *Sensors*, Vol. 10 (2010): 5626–5641.

[13] Rübner, M., Körner, C., and Singer, R.F., "Integrating sensors in castings made of aluminum – new approaches for direct sensor integration in gravity die casting", *Advances in Science and Technology*, Vol. 56 (2008): 170–175.

[14] Albert, F., Pfeiffer, C., Schmidt, M., Geiger, M., Flössel, M., and Michaelis, A., "Laser Soldering and Laser Droplet Joining for Mechanical and Electrical Contacting of LTCC/PZT Laminates", *JLMN-Journal of Laser Micro/Nanoengineering Vol. 6, No. 1* (2011)*:* 75–80.

[15] Flössel M., Gebhardt S., Schonecker A., and Michaelis A., "Development of a Novel Sensor-Actuator-Module with Ceramic Multilayer Technology" *Journal of Ceramic Science and Technology*, Vol. 1, No. 1 (2010): 55–58.

[16] Jones, W. K., Liu, Y., Larsen, B., Wang, P., and Zampino, M., *Proceedings - SPIE the international society for optical engineering* (2000): 669–674.

[17] Heraeus Advanced Materials, HeraLock Tape HL2000 CL91-82-42 material datasheet (Hanau, Germany: Heraeus Electronics), https://www.heraeus.com/media/media/het/doc_het/products_and_solutions_het_docments/thick_film/thick_film_data_sheets/passive_components/ltcc/LTCC_Materials_HL2000.pdf.

[18] DuPont Microcircuit Materials, LTCC Green Tape material datasheet and design and layout guidelines (DuPont: 2009), http://www.dupont.com/content/dam/assets/products-and-services/electronic-electrical-materials/assets/datasheets/prodlib/LTCC_DesignGuide.pdf.

[19] DuPont, 9K7 Green Tape low temperature co-fired ceramic system - material datasheet (DuPont, 2015) https:// www.dupont.com/content/dam/dupont/amer/us/en/products/ei-transformation/documents/9K7_SelectorGuide.pdf.

[20] Gebhardt, S., Ernst, D., Bramlage, B., Flössel, M., and Schönecker, A., "Integrated Piezoelectrics for Smart Microsystems - A Teamwork of Substrate and Piezo", *Advances in Science and Technology*, Vol. 77 (2012): 1–10.

[21] Heraeus Advanced Materials, Co-Firing Silver Conductor TC0306.

[22] Heraeus Advanced Materials, TC0308 Co-Firing Silver Via Fill datasheet.

[23] Nowak, K.M., Baker, H.J., and Hall, D.R., *Appl. Phys. A*, Vol. 84 (2006): 267-270.

[24] Flössel, M., Gebhardt, S., Schönecker, A., Michaelis, A., "Investigation on LTCC/PZT interface in a novel sensor-actuator-module for metal die casting", *Proceedings of ISAF 2011* (Vancouver, July 2011): 25-27.

[25] Brunhuber, E., *Praxis der Druckgussfertigung.* Berlin, Germany: Schiele & Schön, 1991.

[26] Nogowizin, B., *Theorie und Praxis des Druckgusses.* Berlin, Germany: Schiele & Schön, 2011.

[27] Batchelor, G.K., *An introduction to fluid dynamics,* 14th ed. Cambridge, UK: Cambridge University Press, 2013.

[28] Schürmann, H., *Konstruieren mit Faser-Kunststoff-Verbunden,* 2nd ed. Berlin, Heidelberg, New York: Springer, 2007.

[29] Winkler A., and Modler N., "Online Poling of Thermoplastic-Compatible Piezoceramic Modules during the Manufacturing Process of Active Fiber-Reinforced Composites", *20th Symposium on Composites, Materials Science Forum* (2015): 825-826, 787–794.

[30] Holeczek, K., Starke, E., Winkler, A., Dannemann, M., and Modler, N., "Numerical and Experimental Characterization of Fiber-Reinforced Thermoplastic Composite Structures with Embedded Piezoelectric Sensor-Actuator Arrays for Ultrasonic Applications", *Applied Sciences*, Vol. 6(3) (2016): 55.

[31] Hufenbach, W.A., Modler, N., Winkler, A., Ilg, J., and Rupitsch, S.J., *Smart Mater. Struct. Smart Materials and Structures*, Vol. 23(2) (2014), 025011.

[32] Winkler, A., *Seriengerechte Bauweisen und Fertigungstechnologien für funktionsintegrative thermoplastische Faserverbundbauteile mit eingebetteten Piezokeramik-Modulen, Dissertation* (Dresden, 2016).

[33] Weinhold, S., Ebert, R., and Exner, H., *Laser-Magazin; ISSN 0945-8875*, 5 (2015): 20–21.

[34] Prabhu, K., Bali, R., and Ranjan, R., "Effect of substrate surface texture and flux coating on the evolution of microstructure during solidification of lead-free Sn–3.5 Ag solder alloy", *Materials & Design*, Vol. 25 (2004): 447–449.

[35] Schmidt, M., *Prozessregelung für das Laserstrahl-Punktschweissen in der Elektronikproduktion, Dissertation (*Meisenbach, Bamberg, 2002).

[36] Harman, G.G., *Wire bonding in microelectronics,* 3rd ed. New York: McGraw-Hill, 2010.

[37] Heiermann, W., *Entwicklung mikroelektronischer Kontaktierungsmethoden für Hochtemperatur-Anwendungen über 250°C, Dissertation,* (Duisburg, Germany: Universitätsbibliothek Duisburg-Essen, 2014).

[38] Zakel, E., Titerle, L., Oppert, T., and Blankenhorn, R.G., "Parametric investigation of solder bumping for assembly of optical components", *Proceedings of the International Conference on Electronics Packaging* (2002).

[39] Wang, C.-H., Hwang, W.-S., Chen, W.-M., Tsai, H.-L., and Wu, C.-H., *MATERIALS TRANSACTIONS*, Vol. 57 (2016): 797–804.

[40] Rheinschmitt, L., Burkhardt, T., Nagel, J.A., Beckert, E., Gengenbach, U., and Bretthauer, G., " Investigation of the use of Solderjet Bumping for joining the thin-walled glass package of a complex mechatronic lens implant", *Biomedical Engineering / Biomedizinische Technik*, Vol. 57 (2012).

[41] Yang, L., Liu, W., Wang, C., & Tian, Y., ed., "Development of a three-dimensional integrated solder ball bumping & bonding method for MEMS devices*"* (IEEE, 2011): 1-4.

[42] Azdasht, G., and Titerle, L., 2010. Method and device for applying a solder to a substrate, US Patent US20070257090A1, filed November 8 2007, and issued May 18 2010.

[43] Azdasht, G., Belötungsvorrichtung,1994, German Patent DE4320055A1, filed June 17 1993, and issued December 22 1994.

[44] Burkhardt, T., Goy, M., Hornaff, M., Appelfelder, M., and Reinlein, C., *Physics Procedia*, Vol. 83 (2016): 540–548.

[45] Ribes, P., Burkhardt T., Hornaff, M., Kousar, S., Burkhardt, D., Beckert, E., Gilaberte, M., Guilhot, D., Montes, M. Galan3, S. Ferrando3,4, R. Eberhardt, and A. Tünnermann, "Solderjet Bumping as a Versatile Tool for the Integration of Piezoelectric Deformable Mirrors", *The 2nd. Laser Ignition Conference (LIC'14)* (Yokohama, Japan, April 2014): 22–24.

[46] Ribes-Pleguezuelo, P., Inza, A.M., Basset, M.G., Rodríguez, P., Rodríguez, G., Laudisio, M., Galan, M., Hornaff, M., Beckert, E., Eberhardt, R., and Tünnermann, A., "Assembly processes comparison for a miniaturized laser used for the Exomars European Space Agency mission", *Opt. Eng Optical Engineering*, Vol. 55 (2016): 116107.

[47] Kessling, O.S., Schussler, F., Feldmann, K., and Lueth, T.C., eds., "A New process for Flip-chip Interconnections with Variable Stand-offs", *10th Electronics Packaging Technology Conference* (IEEE, 2008): 620-625.

[48] Luo, Z., Wang, X., Wang, L., Sun, D., and Li, Z., "Fabrication and evaluation of calcium alginate/ calcium polyphosphate composite", Materials Letters, Vol. 180 (October 2016): 184–187.

[49] Vekselman, V., Sande, L., and Kornev, K.G., *Journal of Applied Physics*, Vol. 118 (2015): 224902.

[50] Zhang, L., Zhu, Y., Cheng, X., Wang, C., Gu, J.W., Chen, X.L., and Liu, E.H., "The Simulation Study of Fluid Physical Properties on Drop Formation of Drop-on-demand Inkjet Printing", *MATEC Web of Conferences*, Vol. 25, 03011 (2015).

[51] Maekawa, K., Yamasaki, K., Niizeki, T., Mita, M., Matsuba, Y., Terada, N., and Saito, H., "Drop-on-Demand Laser Sintering With Silver Nanoparticles for Electronics Packaging", *IEEE Trans. Compon., Packag. Manufact. Technol. IEEE Transactions on Components, Packaging and Manufacturing Technology*, Vol. 2 (IEEE, 2012): 868–877.

[52] Luo, Z., Zheng, G., and Wang, L., "A Study on the Influence of the Nozzle Lead Angle on the Performance of Liquid Metal Electromagnetic Micro-Jetting", Vol. 7 (2016).

[53] Ditterich, J., Stollenwerk, J., Kogel-Hollacher, M., Traub, M., and Schnitzler, C., "Coaxial Laser Brazing Head", *Proceedings of the Fifth Intemational WLT-Conference on Lasers in Manufacturing* (2009): 251-256.

[54] Kastens, M., and Schmidt, M., "Laser droplet welding - bonding on thin substrates", *Proceedings of the 5th LANE* (2007): 271–284.

[55] Jahrsdoerfer, B., Esser, G., Geiger, M., and Govekar, E., eds., *Laser droplet weld: an innovative joining technology opens new application possibilities,* 4977th ed. (SPIE, 2003): 12.

[56] Kuznetsov, A., Jeromen, A., and Govekar, E., "Droplet detachment regimes in annular laser beam droplet generation from a metal wire", *CIRP Annals - Manufacturing Technology*, Vol. 63 (2014): 225–228.

[57] Deutsches Kupfer-Institut, Werkstoffdatenblatt: Cu-ETP, http://www.abmkupral.hu/letoltes/certec/Cu-ETP.pdf.

[58] Ashcroft, N., and Mermin, D., *Solid State Physics: Revised Edition* (Singapore: Cengage Learning Asia, 2016): 872.

[59] Straschill, M., *Neuzeitliches Beizen von Metallen.* Leuze, Bad Saulgau, Germany, 1962.

[60] Deutsches Kupfer-Institut Düsseldorf, Kupfer-Zinn-Knetlegierungen (Zinnbronzen), https://www.kupferinstitut.de/fileadmin/user_upload/kupferinstitut.de/de/Documents/Shop/Verlag/Downloads/Werkstoffe/i1015.pdf.

[61] Deutsches Kupfer-Institut Berlin, West, DKI Werkstoff-Datenblätter - CuSn12, http://www.abmkupral.hu/letoltes/carocast/CuSn12-C.pdf.

[62] Bargel, H.-J., and Schulze, G., *Werkstoffkunde,* 11th ed. Berlin, Germany: Springer, 2012.

[63] Dura-Bar Metal Services, Cu89Sn11 High Tin Bronze Specifications and physical properties, www.dura-barms.com.

[64] Cook, M., and Tallis, W.G., "The physical properties and Annealing Characteristics of Standard Phosphor-Bronze Alloys", *Journal of the Institute of Metals*, Vol. 67 (1941): 49–65.

[65] Oettel, H., and Schumann, H., *Metallografie,* 15th ed. Weinheim: Wiley-VCH, 2011.

[66] Dorn, L., *Hartlöten und Hochtemperaturlöten.* Renningen: expert-Verl.2007.

[67] Effenberg, G., and Ilyenko, S., "Ag-Cu-Sn (Silver-Copper-Tin)", Effenberg, G., and Ilyenko, S., Eds., *Non-Ferrous Metal Systems. Part 3,* (Berlin, Heidelberg: Springer Berlin Heidelberg, 2007): 47–62.

[68] CUSn12-C, DKI Werkstoff-Datenblätter, http://www.abmkupral.hu/letoltes/carocast/CuSn12-C.pdf (2005).

[69] Weast, R.C., *CRC Handbook of chemistry and physics,* (Cleveland, Ohio: CRC Press, 1974).

[70] Müller, W., *Metallische Lotwerkstoffe.* Düsseldorf, Germany: DVS-Verlag, 1990.

[71] Kou, S., *Welding metallurgy,* 2nd ed. Hoboken, New Jersey: Wiley-Interscience, 2003.

[72] Deng, X., Koopman, M., Chawla, N., and Chawla, K.K., "Young's modulus of (Cu, Ag)-Sn intermetallics measured by nanoindentation", *Materials Science and Engineering: A*, Vol. 364 (2004): 240–243.

[73] Israelachvili, J., *Intermolecular and surface forces,* 3rd ed. Burlington, MA: Academic Press, 2011.

[74] Görlich, J., Oberdorfer, C., Baither, D., Schmitz, G., Reinke, C., and Wilke, U., "The role of oxide layers in solder joints", *Journal of Alloys and Compounds*, Vol. 490 (2010): 336–341.

[75] Kepets GmbH, Technical specification SENO 2001 Deox, https://www.buerklin.com/medias/sys_master/download/download/hab/hb5/8893358768158.pdf.

[76] Mäusezahl, M., Hornaff, M., Burkhardt, T., and Beckert, E., "Mechanical Properties of Laser-jetted SAC305 Solder on Coated Optical Surfaces", *Physics Procedia*, Vol. 83 (2016): 532–539.

[77] Zhai, W., Wang, W.L., Geng, D.L., and Wei, B., "A DSC analysis of thermodynamic properties and solidification characteristics for binary Cu–Sn alloys", *Acta Materialia*, Vol. 60 (2012): 6518–6527.

[78] IPG Photonics, Single Mode Fiber Lasers Brochure, http://german.ipgphotonics.com/Collateral/Documents/English-US/sm_ipgbrochure.pdf (accessed November 21 2012).

[79] Jeromen, A., Held, C., Govekar, E., Roth, S., and Schmidt, M., "Modelling of droplet detachment in the laser droplet brazing process", *Journal of Materials Processing Technology*, Vol. 214 (2014): 737–749.

[80] First Sensor pressure sensor HMA B001 U Z7 H5, DS Standard-HMA datasheet, https://www.first-sensor.com/cms/upload/datasheets/DS_Standard-HMA_E_11697.pdf.

[81] Bibus Matrix Elektromagnet-Ventile Serie 720, https://www.bibus.de/produkte-loesungen/pneumatik/schnellschaltventile/matrix-serie-720.

[82] Liu, P., Tong, L., Wang, J., Shi, L., and Tang, H., "Challenges and developments of copper wire bonding technology", *Microelectronics Reliability*, Vol. 52 (2012): 1092–1098.

[83] Boettcher, T., Rother, M., Liedtke, S., Ullrich, M., Bollmann, M., Pinkernelle, A., Gruber, D., Funke, H.-J., Kaiser, M., Lee, K., Li, M., Leung, K., Li, T., Farrugia, M.L., O'Halloran, O., Petzold, M., Marz, B., and Klengel, R., "On the intermetallic corrosion of Cu-Al wire bonds", *IEEE 12th Electronics Packaging Technology Conference*, Vol. 12 (2010): 585–590.

[84] Curiotto, S., and Chatain, D., "Solid/liquid interfacial energy and wetting of Cu at Co surfaces and grain boundaries", *Scripta Materialia*, Vol. 60 (2009): 40–43.

[85] Stein, S., Heberle, J., Gürtler, F.J., Cvecek, K., Roth, S., and Schmidt, M., " Influences of Nozzle Material on Laser Droplet Brazing Joints with Cu89Sn11 Preforms", *Physics Procedia,* 709–719, 2014.

[86] Stein, S., Dobler, M., Radel, T., Strauß, M., Breitschwerdt, H., Hugger, F., Roth, S., and Schmidt, M., *Prod. Eng. Res. Devel.*, Vol. 26, 1455, 2017.

[87] Hashida, M., Mishima, H., Tokita, S., and Sakabe, "Non-thermal ablation of expanded polytetrafluoroethylene with an intense femtosecond-pulse laser", S., *Optics Express*, Vol. 17, Issue 15 (2009): 13116–13121.

[88] Dirscherl, M., *Ultrakurzpulslaser.* Erlangen: BLZ Bayerisches Laserzentrum, 2005.

[89] Chichkov, B. N., Momma, C., Nolte, S., Alvensleben, F. von, and Tünnermann, A., "Femtosecond, picosecond and nanosecond laser ablation of solids", *Applied Physics A*, Vol. 63, Issue 2 (2996): 109–115.

[90] Brown, M.S., and Arnold, C.B., *Fundamentals of laser-material interaction and application to multiscale surface modification.* Springer Berlin Heidelberg, 2010.

[91] Dausinger, F., *Strahlwerkzeug Laser,* Forschungsberichte des IFSW. Stuttgart, Germany: Teubner, 1995.

[92] Graf, T., and Hügel, H., *Laser in der Fertigung; Strahlquellen, Systeme, Fertigungsverfahren,* 2nd ed. (Wiesbaden, Germany: Vieweg+Teubner Verlag / GWV Fachverlage, 2009).

[93] Poprawe, R., Boucke, K., and Hoffman, D., *Tailored light.* Berlin, Germany: Springer, 2011.

[94] Hecht, E., *Optics,* 4th ed. Reading, Mass: Addison-Wesley, 2002.

[95] Eichler, J., and Eichler, H.-J., *Laser,* 7th ed. Springer Berlin Heidelberg, 2010.

[96] Hügel, H., Dausinger, F., and Graf, T., *Laser in der Fertigung,* 2nd ed. Wiesbaden: Teubner, 2007.

[97] Poprawe, R., *Lasertechnik für die Fertigung*. Springer Berlin Heidelberg, 2005.

[98] Stein, S., Dippert, J., Roth, S., and Schmidt, M., "Laser Drop on Demand Micro Joining for High Temperature Wire Bonding Applications – System Technology And Mechanical Joint Performance", *Journal of Laser Micro/Nanoengineering*, Vol. 12 (2017): 239–247.

[99] Stein, S., Heberle, J., Suchy, M., Tenner, F., Hugger, F., Roth, S., and Schmidt, M., "High Temperature Laser Based Drop on Demand Micro Joining of Thin Metallic Layers or Foils using Bronze Braze Preforms", *JLMN Journal of Laser Micro/Nanoengineering*, Vol. 11 (2106): 111–116.

[100] Huang, C. P., "Removal of Phosphate by Powdered Aluminum Oxide Adsorption", *Journal of the Water Pollution Control Federation*, Vol. 49 (1977): 1811–1817.

[101] Dobler, M., Schmidt, M., Otto, A., and Leitz, K.-H., "Simulation of process dynamics in laser beam brazing", *Icaleo Conference Proceedings 2013* (2013): 85–90.

[102] Gürtler, F.J., Karg, M., Leitz, K.-H., and Michael Schmidt, "Simulation of laser beam melting of steel powders using the three-dimensional volume of fluid method", *Physics Procedia*, Vol. 41 (2013): 881–886.

[103] Engel, T.K., "The heat capacities of Al203, U02 and PuO2 From 300 To 1100 °K", *Journal of Nuclear Materials*, Vol. 31 Issue 2 (1969): 211–214.

[104] Kingery, W.D., Francl, J., Coble, R.L., and Vasilos, T., "Thermal Conductivity: X, Data for Several Pure Oxide Materials Corrected to Zero Porosity", *Journal of the American Ceramic Society*, Vol. 37 No. 2 (1954): 107-110.

[105] Vitos, L., Ruban, A., and Skriver, H.L., "The surface energy of metals", *Surface Science*, Vol. 411, No. 1-2 (1998), 186–202.

[106] Brooks, R., Egry, I., Seetharaman, S., and Grant, D., "Reliable data for high-temperature viscosity and surface tension: Results from a European project", *High Temperatures - High Pressures*, Vol. 33(6) (2001), 631–637.

[107] Hirt, C.W., and Nichols, B.D., "Volume of Fluid (VOF) Method for the Dynamics of Free Boundaries", *YJCPH: Journal of Computational Physics*, Vol. 39 (1981): 201–225.

[108] Lafaurie, B., Nardone, C., Scardovelli, R., Zaleski, S., and Zanetti, G., "Modelling Merging and Fragmentation in Multiphase Flows with SURFER", *Journal of Computational Physics*, Vol. 113 Issue 1 (1994): 134–147.

[109] Gatzen, M., Radel, T., Thomy, C., and Vollertsen, F., "Wetting behaviour of eutectic Al-Si droplets on zinc coated steel substrates", *Journal of Materials Processing Technology*, Vol. 214 (2014): 123–131.

[110] Dobrovinskaya, E.R., Litvinov, L.A., and Pishchik, V.V., *Sapphire*. New York: Springer, 2009.

[111] Reitz, R.D., and Bracco, F.V., "Mechanism of atomization of a liquid jet", *Physics of Fluids*, Vol. 25 (1982): 1730–1742.

[112] Suganuma, K., Miyamoto, Y., and Koizumi, M., "Joining of Ceramics and Metals", *Annual Review of Material Science*, Vol. 18 (1988): 47–73.

[113] Chien-Hsun Wang, Ho-Lin Tsai, Yu-Che Wu, and Weng-Sing Hwang, "Investigation of molten metal droplet deposition and solidification for 3D printing techniques", *Journal of Micromechanics and Microengineering*, Vol. 26 Number 9 (2016): 095012.

[114] Mata, S., and Taechajedcadarungsri, S., "The effects of capillary tip geometry on solder jetting accuracy in laser solder ball jetting process", *Asia-Pacific Journal of Science and Technology*, Vol. 16 (2011): 596–611.

[115] Ghassemieh, E., Versteeg, H.K., and Acar, M., "The effect of nozzle geometry on the flow characteristics of small water jets", *Journal of Mechanical Engineering Science: Proceedings of the Institution of Mechanical Engineers, Part C*, Vol. 220 Issue 12 (2006:) 1739–1753.

[116] Häfner, T., Hofmann, L., and Eiselen, S., „Einsatz der Simulation zur Optimierung der Abtragsrate beim Strukturieren mittels Pikosekundenlaser", *Tagungsband Laser in der Elektronikproduktion und Feinwerktechnik* (2013): 51–55.

[117] Vision Research Inc., Manual: Phantom v1210, https://www.phantom-highspeed.com/Products/High-Speed-Cameras/v1210.

[118] Zhang, Z., "A flexible new technique for camera calibration", *IEEE Transactions on Pattern Analysis and Machine Intelligence*, Vol. 22 (2000): 1330–1334.

[119] Heikkila, J., and Silven, O., "A four-step camera calibration procedure with implicit image correction*", Proceedings of IEEE Computer Society Conference on Computer Vision and Pattern Recognition* (1997): 1106-1112.

[120] Stein, S., Zhao, W., Hentschel, O., Bickmann, C., Roth, S., Frick, T., and Schmidt, M., Flight trajectory analysis of CuSn-droplets generated by laser drop on demand jetting, using stereoscopic high-speed imaging", *Opt. Express*, Vol. 26, Issue 8 (2018): 10968–10980.

[121] Stein, S., Wedler, J., Rhein, S., Schmidt, M., Körner, C., Michaelis, A., and Gebhardt, S., " A process chain for integrating piezoelectric transducers into aluminum die castings to generate smart lightweight structures", *Results in Physics,* 7 *(*2017): 2534-2539.

[122] Kim, J.-W., and Jung, S.-B., "Re-examination of the solder ball shear test for evaluation of the mechanical joint strength", *International Journal of Solids and Structures*, Vol. 43 Issues 7-8 (2006): 1928–1945.

[123] Lancaster, J.F., *Metallurgy of Welding.* Elsevier Science, 1999.

[124] Uday, M.B., Ahmad-Fauzi, M.N., Alias, M.N., and Srithar, R., *Current Issues and Problems in the Joining of Ceramic to Metal.* IntechOpen, 2016.

[125] Stein, S., Schaumberger, K., Frick, T., Roth, S., and Schmidt, M., "Laser Drop on Demand Micro Joining – Analytic Process Model to Quantify Braze Absorptance and Cumulative Energy Balance", *Advanced Engineering Materials*, Volume 20 Issue 12 (2018): 1800421.

[126] Simon, N. J., Drexler, E. S., Reed, R. P., International Copper Association., and National Institute of Standards and Technology, *Properties of copper and copper alloys at cryogenic temperatures,* U.S. Dept. of

Commerce, Technology Administration, National Institute of Standards and Technology (Boulder, CO, Washington, D.C., 1992).

[127] Stein, S., Roth, S., Modler, N., Gude, M., Weber, T., and Winkler, A., "Investigations on the process chain for the integration of piezoelectric ceramics into die casted aluminum structures", *Proceedings of 5th Scientific Symposium "Lightweight Design by Integrating Functions"* (Dresden, Germany, September 14-16, 2015.

[128] Fleurial, J.-P., "Thermoelectric Power Generation Materials: Technology and Application Opportunities", *The Journal of The Minerals, Metals & Materials Society*, Vol. 61(4) (2009): 79-85.

[129] Snyder, G.J., and Toberer, E.S., "Complex thermoelectric materials", *Nature materials*, Vol. 7 (2008): 105–114.

[130] Carslaw H. S., and Jaeger J. C., *"Conduction of Heat in Solids"*, Second edition, Oxford University Press, Oxford, UK, (1959)

Own publications referring to this work:

2014 Stein, S., Heberle, J., Gürtler, F. J., Cvecek, K., Roth, S., Schmidt, M., "Influences of Nozzle Material on Laser Droplet Brazing Joints with CuSn12 Preforms", 8th International Conference on Laser Assisted Net Shape Engineering LANE 2014, *Physics Procedia* 56 *(*2014): S. 709–19

2015 Stein, S., Roth, S., Modler, N., Gude, M., Weber, T., Winkler, A., "Investigations on laser based joining of novel thermo-plastic compatible piezoceramic modules", *Proceedings of 5th Scientific Symposium,* "Lightweight Design by Integrating Functions" (September 14-16, 2015), Dresden, Germany

2015 Stein, S., Schmidt, M., Wedler, J., Körner, C., Rhein, S.; Gebhardt, S., Michaelis, A., "Investigations on the process chain for the integration of piezoelectric ceramics into die casted aluminum structures", *Proceedings of 5th Scientific Symposium* "Lightweight Design by Integrating Functions" (September 14-16, 2015), Dresden, Germany.

2016 Stein, S., Heberle, J., Suchy, M., Tenner, F., Hugger, F., Roth, S., Schmidt, M., "High Temperature Laser Based Drop on Demand Micro Joining of Thin Metallic Layers or Foils using Bronze Braze Preforms", *JLMN Journal of Laser Micro/Nanoengineering* 11 (2016) 1: 111–16

2017 Stein, S., Wedler, J., Rhein, S., Schmidt, M., Körner, C., Michaelis, A., Gebhardt, S., "A process chain for integrating piezoelectric transducers into aluminum die castings to generate smart lightweight structures", *Results in Physics* (2017) 7C: 2534-2539.

2017 Stein, S., Dippert, J., Roth, S., Schmidt, M., "Laser Drop on Demand Micro Joining for High Temperature Wire Bonding Applications – System Technology and Mechanical Joint Performance", *Journal of Laser Micro/Nanoengineering* 12 (2017) 3: 239–47.

2017 Stein, S., Dobler, M., Radel, T., Strauß, M., Breitschwerdt, H., Hugger, F., Roth, S., Schmidt, M., "Experimental and numerical investigations regarding laser drop on demand jetting of Cu alloys", *WGP Journal Production Engineering* 26 (2017) 12: 1455.

2018 Stein, S., Zhao, W., Hentschel, O., Bickmann, C., Roth, S., Frick, T., Schmidt, M., "Flight trajectory analysis of CuSn-droplets generated by laser drop on demand jetting, using stereoscopic high-speed imaging", *Optics Express*, ISSN: 1094-4087

2018 Stein, S., Schaumberger, K., Frick, T., Roth, S., Schmidt, M, "Laser drop on demand micro joining for high temperature wire bonding applications – analytic process model to quantify braze absorptance and cumulative energy balance", *Advanced Engineering Materials,* ISSN: 1527-2648

Reihenübersicht

Koordination der Reihe (Stand 2021):
Geschäftsstelle Maschinenbau, Dr.-Ing. Oliver Kreis, www.mb.fau.de/diss/

Im Rahmen der Reihe sind bisher die nachfolgenden Bände erschienen.

Band 1 – 52
Fertigungstechnik – Erlangen
ISSN 1431-6226
Carl Hanser Verlag, München

Band 53 – 307
Fertigungstechnik – Erlangen
ISSN 1431-6226
Meisenbach Verlag, Bamberg

ab Band 308
FAU Studien aus dem Maschinenbau
ISSN 2625-9974
FAU University Press, Erlangen

Die Zugehörigkeit zu den jeweiligen Lehrstühlen ist wie folgt gekennzeichnet:

Lehrstühle:

FAPS	Lehrstuhl für Fertigungsautomatisierung und Produktionssystematik
FMT	Lehrstuhl für Fertigungsmesstechnik
KTmfk	Lehrstuhl für Konstruktionstechnik
LFT	Lehrstuhl für Fertigungstechnologie
LPT	Lehrstuhl für Photonische Technologien
REP	Lehrstuhl für Ressourcen- und Energieeffiziente Produktionsmaschinen

Band 1: Andreas Hemberger
Innovationspotentiale in der rechnerintegrierten Produktion durch wissensbasierte Systeme
FAPS, 208 Seiten, 107 Bilder. 1988.
ISBN 3-446-15234-2.

Band 2: Detlef Classe
Beitrag zur Steigerung der Flexibilität automatisierter Montagesysteme durch Sensorintegration und erweiterte Steuerungskonzepte
FAPS, 194 Seiten, 70 Bilder. 1988.
ISBN 3-446-15529-5.

Band 3: Friedrich-Wilhelm Nolting
Projektierung von Montagesystemen
FAPS, 201 Seiten, 107 Bilder, 1 Tab. 1989.
ISBN 3-446-15541-4.

Band 4: Karsten Schlüter
Nutzungsgradsteigerung von Montagesystemen durch den Einsatz der Simulationstechnik
FAPS, 177 Seiten, 97 Bilder. 1989.
ISBN 3-446-15542-2.

Band 5: Shir-Kuan Lin
Aufbau von Modellen zur Lageregelung von Industrierobotern
FAPS, 168 Seiten, 46 Bilder. 1989.
ISBN 3-446-15546-5.

Band 6: Rudolf Nuss
Untersuchungen zur Bearbeitungsqualität im Fertigungssystem Laserstrahlschneiden
LFT, 206 Seiten, 115 Bilder, 6 Tab. 1989.
ISBN 3-446-15783-2.

Band 7: Wolfgang Scholz
Modell zur datenbankgestützten Planung automatisierter Montageanlagen
FAPS, 194 Seiten, 89 Bilder. 1989.
ISBN 3-446-15825-1.

Band 8: Hans-Jürgen Wißmeier
Beitrag zur Beurteilung des Bruchverhaltens von Hartmetall-Fließpreßmatrizen
LFT, 179 Seiten, 99 Bilder, 9 Tab. 1989.
ISBN 3-446-15921-5.

Band 9: Rainer Eisele
Konzeption und Wirtschaftlichkeit von Planungssystemen in der Produktion
FAPS, 183 Seiten, 86 Bilder. 1990.
ISBN 3-446-16107-4.

Band 10: Rolf Pfeiffer
Technologisch orientierte Montageplanung am Beispiel der Schraubtechnik
FAPS, 216 Seiten, 102 Bilder, 16 Tab. 1990.
ISBN 3-446-16161-9.

Band 11: Herbert Fischer
Verteilte Planungssysteme zur Flexibilitätssteigerung der rechnerintegrierten Teilefertigung
FAPS, 201 Seiten, 82 Bilder. 1990.
ISBN 3-446-16105-8.

Band 12: Gerhard Kleineidam
CAD/CAP: Rechnergestützte Montagefeinplanung
FAPS, 203 Seiten, 107 Bilder. 1990.
ISBN 3-446-16112-0.

Band 13: Frank Vollertsen
Pulvermetallurgische Verarbeitung eines übereutektoiden verschleißfesten Stahls
LFT, XIII u. 217 Seiten, 67 Bilder, 34 Tab. 1990. ISBN 3-446-16133-3.

Band 14: Stephan Biermann
Untersuchungen zur Anlagen- und Prozeßdiagnostik für das Schneiden mit CO_2-Hochleistungslasern
LFT, VIII u. 170 Seiten, 93 Bilder, 4 Tab. 1991. ISBN 3-446-16269-0.

Band 15: Uwe Geißler
Material- und Datenfluß in einer flexiblen Blechbearbeitungszelle
LFT, 124 Seiten, 41 Bilder, 7 Tab. 1991.
ISBN 3-446-16358-1.

Band 16: Frank Oswald Hake
Entwicklung eines rechnergestützten Diagnosesystems für automatisierte Montagezellen
FAPS, XIV u. 166 Seiten, 77 Bilder. 1991.
ISBN 3-446-16428-6.

Band 17: Herbert Reichel
Optimierung der Werkzeugbereitstellung durch rechnergestützte Arbeitsfolgenbestimmung
FAPS, 198 Seiten, 73 Bilder, 2 Tab. 1991.
ISBN 3-446-16453-7.

Band 18: Josef Scheller
Modellierung und Einsatz von Softwaresystemen für rechnergeführte Montagezellen
FAPS, 198 Seiten, 65 Bilder. 1991.
ISBN 3-446-16454-5.

Band 19: Arnold vom Ende
Untersuchungen zum Biegeumforme mit elastischer Matrize
LFT, 166 Seiten, 55 Bilder, 13 Tab. 1991.
ISBN 3-446-16493-6.

Band 20: Joachim Schmid
Beitrag zum automatisierten Bearbeiten von Keramikguß mit Industrierobotern
FAPS, XIV u. 176 Seiten, 111 Bilder, 6 Tab. 1991. ISBN 3-446-16560-6.

Band 21: Egon Sommer
Multiprozessorsteuerung für kooperierende Industrieroboter in Montagezellen
FAPS, 188 Seiten, 102 Bilder. 1991.
ISBN 3-446-17062-6.

Band 22: Georg Geyer
Entwicklung problemspezifischer Verfahrensketten in der Montage
FAPS, 192 Seiten, 112 Bilder. 1991.
ISBN 3-446-16552-5.

Band 23: Rainer Flohr
Beitrag zur optimalen Verbindungstechnik in der Oberflächenmontage (SMT)
FAPS, 186 Seiten, 79 Bilder. 1991.
ISBN 3-446-16568-1.

Band 24: Alfons Rief
Untersuchungen zur Verfahrensfolge Laserstrahlschneiden und -schweißen in der Rohkarosseriefertigung
LFT, VI u. 145 Seiten, 58 Bilder, 5 Tab. 1991. ISBN 3-446-16593-2.

Band 25: Christoph Thim
Rechnerunterstützte Optimierung von Materialflußstrukturen in der Elektronikmontage durch Simulation
FAPS, 188 Seiten, 74 Bilder. 1992.
ISBN 3-446-17118-5.

Band 26: Roland Müller
CO_2 -Laserstrahlschneiden von kurzglasverstärkten Verbundwerkstoffen
LFT, 141 Seiten, 107 Bilder, 4 Tab. 1992.
ISBN 3-446-17104-5.

Band 27: Günther Schäfer
Integrierte Informationsverarbeitung bei der Montageplanung
FAPS, 195 Seiten, 76 Bilder. 1992.
ISBN 3-446-17117-7.

Band 28: Martin Hoffmann
Entwicklung einer CAD/CAM-Prozeßkette für die Herstellung von Blechbiegeteilen
LFT, 149 Seiten, 89 Bilder. 1992.
ISBN 3-446-17154-1.

Band 29: Peter Hoffmann
Verfahrensfolge Laserstrahlschneiden und –schweißen: Prozeßführung und Systemtechnik in der 3D-Laserstrahlbearbeitung von Blechformteilen
LFT, 186 Seiten, 92 Bilder, 10 Tab. 1992.
ISBN 3-446-17153-3.

Band 30: Olaf Schrödel
Flexible Werkstattsteuerung mit objektorientierten Softwarestrukturen
FAPS, 180 Seiten, 84 Bilder. 1992.
ISBN 3-446-17242-4.

Band 31: Hubert Reinisch
Planungs- und Steuerungswerkzeuge zur impliziten Geräteprogrammierung in Roboterzellen
FAPS, XI u. 212 Seiten, 112 Bilder. 1992.
ISBN 3-446-17380-3.

Band 32: Brigitte Bärnreuther
Ein Beitrag zur Bewertung des Kommunikationsverhaltens von Automatisierungsgeräten in flexiblen Produktionszellen
FAPS, XI u. 179 Seiten, 71 Bilder. 1992.
ISBN 3-446-17451-6.

Band 33: Joachim Hutfless
Laserstrahlregelung und Optikdiagnostik in der Strahlführung einer CO_2-Hochleistungslaseranlage
LFT, 175 Seiten, 70 Bilder, 17 Tab. 1993.
ISBN 3-446-17532-6.

Band 34: Uwe Günzel
Entwicklung und Einsatz eines Simulationsverfahrens für operative und strategische Probleme der Produktionsplanung und –steuerung
FAPS, XIV u. 170 Seiten, 66 Bilder, 5 Tab. 1993. ISBN 3-446-17604-7.

Band 35: Bertram Ehmann
Operatives Fertigungscontrolling durch Optimierung auftragsbezogener Bearbeitungsabläufe in der Elektronikfertigung
FAPS, XV u. 167 Seiten, 114 Bilder. 1993.
ISBN 3-446-17658-6.

Band 36: Harald Kolléra
Entwicklung eines benutzerorientierten Werkstattprogrammiersystems für das Laserstrahlschneiden
LFT, 129 Seiten, 66 Bilder, 1 Tab. 1993.
ISBN 3-446-17719-1.

Band 37: Stephanie Abels
Modellierung und Optimierung von Montageanlagen in einem integrierten Simulationssystem
FAPS, 188 Seiten, 88 Bilder. 1993.
ISBN 3-446-17731-0.

Band 38: Robert Schmidt-Hebbel
Laserstrahlbohren durchflußbestimmender Durchgangslöcher
LFT, 145 Seiten, 63 Bilder, 11 Tab. 1993.
ISBN 3-446-17778-7.

Band 39: Norbert Lutz
Oberflächenfeinbearbeitung keramischer Werkstoffe mit XeCl-Excimerlaserstrahlung
LFT, 187 Seiten, 98 Bilder, 29 Tab. 1994.
ISBN 3-446-17970-4.

Band 40: Konrad Grampp
Rechnerunterstützung bei Test und Schulung an Steuerungssoftware von SMD-Bestücklinien
FAPS, 178 Seiten, 88 Bilder. 1995.
ISBN 3-446-18173-3.

Band 41: Martin Koch
Wissensbasierte Unterstützung der Angebotsbearbeitung in der Investitionsgüterindustrie
FAPS, 169 Seiten, 68 Bilder. 1995.
ISBN 3-446-18174-1.

Band 42: Armin Gropp
Anlagen- und Prozeßdiagnostik beim Schneiden mit einem gepulsten Nd:YAG-Laser
LFT, 160 Seiten, 88 Bilder, 7 Tab. 1995.
ISBN 3-446-18241-1.

Band 43: Werner Heckel
Optische 3D-Konturerfassung und on-line Biegewinkelmessung mit dem Lichtschnittverfahren
LFT, 149 Seiten, 43 Bilder, 11 Tab. 1995.
ISBN 3-446-18243-8.

Band 44: Armin Rothhaupt
Modulares Planungssystem zur Optimierung der Elektronikfertigung
FAPS, 180 Seiten, 101 Bilder. 1995.
ISBN 3-446-18307-8.

Band 45: Bernd Zöllner
Adaptive Diagnose in der Elektronikproduktion
FAPS, 195 Seiten, 74 Bilder, 3 Tab. 1995.
ISBN 3-446-18308-6.

Band 46: Bodo Vormann
Beitrag zur automatisierten Handhabungsplanung komplexer Blechbiegeteile
LFT, 126 Seiten, 89 Bilder, 3 Tab. 1995.
ISBN 3-446-18345-0.

Band 47: Peter Schnepf
Zielkostenorientierte Montageplanung
FAPS, 144 Seiten, 75 Bilder. 1995.
ISBN 3-446-18397-3.

Band 48: Rainer Klotzbücher
Konzept zur rechnerintegrierten Materialversorgung in flexiblen Fertigungssystemen
FAPS, 156 Seiten, 62 Bilder. 1995.
ISBN 3-446-18412-0.

Band 49: Wolfgang Greska
Wissensbasierte Analyse und Klassifizierung von Blechteilen
LFT, 144 Seiten, 96 Bilder. 1995.
ISBN 3-446-18462-7.

Band 50: Jörg Franke
Integrierte Entwicklung neuer Produkt- und Produktionstechnologien für räumliche spritzgegossene Schaltungsträger (3-D MID)
FAPS, 196 Seiten, 86 Bilder, 4 Tab. 1995.
ISBN 3-446-18448-1.

Band 51: Franz-Josef Zeller
Sensorplanung und schnelle Sensorregelung für Industrieroboter
FAPS, 190 Seiten, 102 Bilder, 9 Tab. 1995.
ISBN 3-446-18601-8.

Band 52: Michael Solvie
Zeitbehandlung und Multimedia-Unterstützung in Feldkommunikationssystemen
FAPS, 200 Seiten, 87 Bilder, 35 Tab. 1996.
ISBN 3-446-18607-7.

Band 53: Robert Hopperdietzel
Reengineering in der Elektro- und Elektronikindustrie
FAPS, 180 Seiten, 109 Bilder, 1 Tab. 1996.
ISBN 3-87525-070-2.

Band 54: Thomas Rebhahn
Beitrag zur Mikromaterialbearbeitung mit Excimerlasern - Systemkomponenten und Verfahrensoptimierungen
LFT, 148 Seiten, 61 Bilder, 10 Tab. 1996.
ISBN 3-87525-075-3.

Band 55: Henning Hanebuth
Laserstrahlhartlöten mit Zweistrahltechnik
LFT, 157 Seiten, 58 Bilder, 11 Tab. 1996.
ISBN 3-87525-074-5.

Band 56: Uwe Schönherr
Steuerung und Sensordatenintegration für flexible Fertigungszellen mit kooperierenden Robotern
FAPS, 188 Seiten, 116 Bilder, 3 Tab. 1996.
ISBN 3-87525-076-1.

Band 57: Stefan Holzer
Berührungslose Formgebung mit Laserstrahlung
LFT, 162 Seiten, 69 Bilder, 11 Tab. 1996.
ISBN 3-87525-079-6.

Band 58: Markus Schultz
Fertigungsqualität beim 3D-Laserstrahlschweißen von Blechformteilen
LFT, 165 Seiten, 88 Bilder, 9 Tab. 1997.
ISBN 3-87525-080-X.

Band 59: Thomas Krebs
Integration elektromechanischer CA-Anwendungen über einem STEP-Produktmodell
FAPS, 198 Seiten, 58 Bilder, 8 Tab. 1997.
ISBN 3-87525-081-8.

Band 60: Jürgen Sturm
Prozeßintegrierte Qualitätssicherung in der Elektronikproduktion
FAPS, 167 Seiten, 112 Bilder, 5 Tab. 1997.
ISBN 3-87525-082-6.

Band 61: Andreas Brand
Prozesse und Systeme zur Bestückung räumlicher elektronischer Baugruppen (3D-MID)
FAPS, 182 Seiten, 100 Bilder. 1997.
ISBN 3-87525-087-7.

Band 62: Michael Kauf
Regelung der Laserstrahlleistung und der Fokusparameter einer CO_2-Hochleistungslaseranlage
LFT, 140 Seiten, 70 Bilder, 5 Tab. 1997.
ISBN 3-87525-083-4.

Band 63: Peter Steinwasser
Modulares Informationsmanagement in der integrierten Produkt- und Prozeßplanung
FAPS, 190 Seiten, 87 Bilder. 1997.
ISBN 3-87525-084-2.

Band 64: Georg Liedl
Integriertes Automatisierungskonzept für den flexiblen Materialfluß in der Elektronikproduktion
FAPS, 196 Seiten, 96 Bilder, 3 Tab. 1997.
ISBN 3-87525-086-9.

Band 65: Andreas Otto
Transiente Prozesse beim Laserstrahlschweißen
LFT, 132 Seiten, 62 Bilder, 1 Tab. 1997.
ISBN 3-87525-089-3.

Band 66: Wolfgang Blöchl
Erweiterte Informationsbereitstellung an offenen CNC-Steuerungen zur Prozeß- und Programmoptimierung
FAPS, 168 Seiten, 96 Bilder. 1997.
ISBN 3-87525-091-5.

Band 67: Klaus-Uwe Wolf
Verbesserte Prozeßführung und Prozeßplanung zur Leistungs- und Qualitätssteigerung beim Spulenwickeln
FAPS, 186 Seiten, 125 Bilder. 1997.
ISBN 3-87525-092-3.

Band 68: Frank Backes
Technologieorientierte Bahnplanung für die 3D-Laserstrahlbearbeitung
LFT, 138 Seiten, 71 Bilder, 2 Tab. 1997.
ISBN 3-87525-093-1.

Band 69: Jürgen Kraus
Laserstrahlumformen von Profilen
LFT, 137 Seiten, 72 Bilder, 8 Tab. 1997.
ISBN 3-87525-094-X.

Band 70: Norbert Neubauer
Adaptive Strahlführungen für CO_2-Laseranlagen
LFT, 120 Seiten, 50 Bilder, 3 Tab. 1997.
ISBN 3-87525-095-8.

Band 71: Michael Steber
Prozeßoptimierter Betrieb flexibler Schraubstationen in der automatisierten Montage
FAPS, 168 Seiten, 78 Bilder, 3 Tab. 1997.
ISBN 3-87525-096-6.

Band 72: Markus Pfestorf
Funktionale 3D-Oberflächenkenngrößen in der Umformtechnik
LFT, 162 Seiten, 84 Bilder, 15 Tab. 1997.
ISBN 3-87525-097-4.

Band 73: Volker Franke
Integrierte Planung und Konstruktion von Werkzeugen für die Biegebearbeitung
LFT, 143 Seiten, 81 Bilder. 1998.
ISBN 3-87525-098-2.

Band 74: Herbert Scheller
Automatisierte Demontagesysteme und recyclinggerechte Produktgestaltung elektronischer Baugruppen
FAPS, 184 Seiten, 104 Bilder, 17 Tab. 1998.
ISBN 3-87525-099-0.

Band 75: Arthur Meßner
Kaltmassivumformung metallischer Kleinstteile – Werkstoffverhalten, Wirkflächenreibung, Prozeßauslegung
LFT, 164 Seiten, 92 Bilder, 14 Tab. 1998.
ISBN 3-87525-100-8.

Band 76: Mathias Glasmacher
Prozeß- und Systemtechnik zum Laserstrahl-Mikroschweißen
LFT, 184 Seiten, 104 Bilder, 12 Tab. 1998.
ISBN 3-87525-101-6.

Band 77: Michael Schwind
Zerstörungsfreie Ermittlung mechanischer Eigenschaften von Feinblechen mit dem Wirbelstromverfahren
LFT, 124 Seiten, 68 Bilder, 8 Tab. 1998.
ISBN 3-87525-102-4.

Band 78: Manfred Gerhard
Qualitätssteigerung in der Elektronikproduktion durch Optimierung der Prozeßführung beim Löten komplexer Baugruppen
FAPS, 179 Seiten, 113 Bilder, 7 Tab. 1998.
ISBN 3-87525-103-2.

Band 79: Elke Rauh
Methodische Einbindung der Simulation in die betrieblichen Planungs- und Entscheidungsabläufe
FAPS, 192 Seiten, 114 Bilder, 4 Tab. 1998.
ISBN 3-87525-104-0.

Band 80: Sorin Niederkorn
Meßeinrichtung zur Untersuchung der Wirkflächenreibung bei umformtechnischen Prozessen
LFT, 99 Seiten, 46 Bilder, 6 Tab. 1998.
ISBN 3-87525-105-9.

Band 81: Stefan Schuberth
Regelung der Fokuslage beim Schweißen mit CO_2-Hochleistungslasern unter Einsatz von adaptiven Optiken
LFT, 140 Seiten, 64 Bilder, 3 Tab. 1998.
ISBN 3-87525-106-7.

Band 82: Armando Walter Colombo
Development and Implementation of Hierarchical Control Structures of Flexible Production Systems Using High Level Petri Nets
FAPS, 216 Seiten, 86 Bilder. 1998.
ISBN 3-87525-109-1.

Band 83: Otto Meedt
Effizienzsteigerung bei Demontage und Recycling durch flexible Demontagetechnologien und optimierte Produktgestaltung
FAPS, 186 Seiten, 103 Bilder. 1998.
ISBN 3-87525-108-3.

Band 84: Knuth Götz
Modelle und effiziente Modellbildung zur Qualitätssicherung in der Elektronikproduktion
FAPS, 212 Seiten, 129 Bilder, 24 Tab. 1998.
ISBN 3-87525-112-1.

Band 85: Ralf Luchs
Einsatzmöglichkeiten leitender Klebstoffe zur zuverlässigen Kontaktierung elektronischer Bauelemente in der SMT
FAPS, 176 Seiten, 126 Bilder, 30 Tab. 1998.
ISBN 3-87525-113-7.

Band 86: Frank Pöhlau
Entscheidungsgrundlagen zur Einführung räumlicher spritzgegossener Schaltungsträger (3-D MID)
FAPS, 144 Seiten, 99 Bilder. 1999.
ISBN 3-87525-114-8.

Band 87: Roland T. A. Kals
Fundamentals on the miniaturization of sheet metal working processes
LFT, 128 Seiten, 58 Bilder, 11 Tab. 1999.
ISBN 3-87525-115-6.

Band 88: Gerhard Luhn
Implizites Wissen und technisches Handeln am Beispiel der Elektronikproduktion
FAPS, 252 Seiten, 61 Bilder, 1 Tab. 1999.
ISBN 3-87525-116-4.

Band 89: Axel Sprenger
Adaptives Streckbiegen von Aluminium-Strangpreßprofilen
LFT, 114 Seiten, 63 Bilder, 4 Tab. 1999.
ISBN 3-87525-117-2.

Band 90: Hans-Jörg Pucher
Untersuchungen zur Prozeßfolge Umformen, Bestücken und Laserstrahllöten von Mikrokontakten
LFT, 158 Seiten, 69 Bilder, 9 Tab. 1999.
ISBN 3-87525-119-9.

Band 91: Horst Arnet
Profilbiegen mit kinematischer Gestalterzeugung
LFT, 128 Seiten, 67 Bilder, 7 Tab. 1999.
ISBN 3-87525-120-2.

Band 92: Doris Schubart
Prozeßmodellierung und Technologieentwicklung beim Abtragen mit CO_2-Laserstrahlung
LFT, 133 Seiten, 57 Bilder, 13 Tab. 1999.
ISBN 3-87525-122-9.

Band 93: Adrianus L. P. Coremans
Laserstrahlsintern von Metallpulver - Prozeßmodellierung, Systemtechnik, Eigenschaften laserstrahlgesinterter Metallkörper
LFT, 184 Seiten, 108 Bilder, 12 Tab. 1999.
ISBN 3-87525-124-5.

Band 94: Hans-Martin Biehler
Optimierungskonzepte für Qualitätsdatenverarbeitung und Informationsbereitstellung in der Elektronikfertigung
FAPS, 194 Seiten, 105 Bilder. 1999.
ISBN 3-87525-126-1.

Band 95: Wolfgang Becker
Oberflächenausbildung und tribologische Eigenschaften excimerlaserstrahlbearbeiteter Hochleistungskeramiken
LFT, 175 Seiten, 71 Bilder, 3 Tab. 1999.
ISBN 3-87525-127-X.

Band 96: Philipp Hein
Innenhochdruck-Umformen von Blechpaaren: Modellierung, Prozeßauslegung und Prozeßführung
LFT, 129 Seiten, 57 Bilder, 7 Tab. 1999.
ISBN 3-87525-128-8.

Band 97: Gunter Beitinger
Herstellungs- und Prüfverfahren für thermoplastische Schaltungsträger
FAPS, 169 Seiten, 92 Bilder, 20 Tab. 1999.
ISBN 3-87525-129-6.

Band 98: Jürgen Knoblach
Beitrag zur rechnerunterstützten verursachungsgerechten Angebotskalkulation von Blechteilen mit Hilfe wissensbasierter Methoden
LFT, 155 Seiten, 53 Bilder, 26 Tab. 1999.
ISBN 3-87525-130-X.

Band 99: Frank Breitenbach
Bildverarbeitungssystem zur Erfassung der Anschlußgeometrie elektronischer SMT-Bauelemente
LFT, 147 Seiten, 92 Bilder, 12 Tab. 2000.
ISBN 3-87525-131-8.

Band 100: Bernd Falk
Simulationsbasierte Lebensdauervorhersage für Werkzeuge der Kaltmassivumformung
LFT, 134 Seiten, 44 Bilder, 15 Tab. 2000.
ISBN 3-87525-136-9.

Band 101: Wolfgang Schlögl
Integriertes Simulationsdaten-Management für Maschinenentwicklung und Anlagenplanung
FAPS, 169 Seiten, 101 Bilder, 20 Tab. 2000.
ISBN 3-87525-137-7.

Band 102: Christian Hinsel
Ermüdungsbruchversagen hartstoffbeschichteter Werkzeugstähle in der Kaltmassivumformung
LFT, 130 Seiten, 80 Bilder, 14 Tab. 2000.
ISBN 3-87525-138-5.

Band 103: Stefan Bobbert
Simulationsgestützte Prozessauslegung für das Innenhochdruck-Umformen von Blechpaaren
LFT, 123 Seiten, 77 Bilder. 2000.
ISBN 3-87525-145-8.

Band 104: Harald Rottbauer
Modulares Planungswerkzeug zum Produktionsmanagement in der Elektronikproduktion
FAPS, 166 Seiten, 106 Bilder. 2001.
ISBN 3-87525-139-3.

Band 105: Thomas Hennige
Flexible Formgebung von Blechen durch Laserstrahlumformen
LFT, 119 Seiten, 50 Bilder. 2001.
ISBN 3-87525-140-7.

Band 106: Thomas Menzel
Wissensbasierte Methoden für die rechnergestützte Charakterisierung und Bewertung innovativer Fertigungsprozesse
LFT, 152 Seiten, 71 Bilder. 2001.
ISBN 3-87525-142-3.

Band 107: Thomas Stöckel
Kommunikationstechnische Integration der Prozeßebene in Produktionssysteme durch Middleware-Frameworks
FAPS, 147 Seiten, 65 Bilder, 5 Tab. 2001.
ISBN 3-87525-143-1.

Band 108: Frank Pitter
Verfügbarkeitssteigerung von Werkzeugmaschinen durch Einsatz mechatronischer Sensorlösungen
FAPS, 158 Seiten, 131 Bilder, 8 Tab. 2001.
ISBN 3-87525-144-X.

Band 109: Markus Korneli
Integration lokaler CAP-Systeme in einen globalen Fertigungsdatenverbund
FAPS, 121 Seiten, 53 Bilder, 11 Tab. 2001.
ISBN 3-87525-146-6.

Band 110: Burkhard Müller
Laserstrahljustieren mit Excimer-Lasern - Prozeßparameter und Modelle zur Aktorkonstruktion
LFT, 128 Seiten, 36 Bilder, 9 Tab. 2001.
ISBN 3-87525-159-8.

Band 111: Jürgen Göhringer
Integrierte Telediagnose via Internet zum effizienten Service von Produktionssystemen
FAPS, 178 Seiten, 98 Bilder, 5 Tab. 2001.
ISBN 3-87525-147-4.

Band 112: Robert Feuerstein
Qualitäts- und kosteneffiziente Integration neuer Bauelementetechnologien in die Flachbaugruppenfertigung
FAPS, 161 Seiten, 99 Bilder, 10 Tab. 2001.
ISBN 3-87525-151-2.

Band 113: Marcus Reichenberger
Eigenschaften und Einsatzmöglichkeiten alternativer Elektroniklote in der Oberflächenmontage (SMT)
FAPS, 165 Seiten, 97 Bilder, 18 Tab. 2001.
ISBN 3-87525-152-0.

Band 114: Alexander Huber
Justieren vormontierter Systeme mit dem Nd:YAG-Laser unter Einsatz von Aktoren
LFT, 122 Seiten, 58 Bilder, 5 Tab. 2001.
ISBN 3-87525-153-9.

Band 115: Sami Krimi
Analyse und Optimierung von Montagesystemen in der Elektronikproduktion
FAPS, 155 Seiten, 88 Bilder, 3 Tab. 2001.
ISBN 3-87525-157-1.

Band 116: Marion Merklein
Laserstrahlumformen von Aluminiumwerkstoffen - Beeinflussung der Mikrostruktur und der mechanischen Eigenschaften
LFT, 122 Seiten, 65 Bilder, 15 Tab. 2001.
ISBN 3-87525-156-3.

Band 117: Thomas Collisi
Ein informationslogistisches Architekturkonzept zur Akquisition simulationsrelevanter Daten
FAPS, 181 Seiten, 105 Bilder, 7 Tab. 2002.
ISBN 3-87525-164-4.

Band 118: Markus Koch
Rationalisierung und ergonomische Optimierung im Innenausbau durch den Einsatz moderner Automatisierungstechnik
FAPS, 176 Seiten, 98 Bilder, 9 Tab. 2002.
ISBN 3-87525-165-2.

Band 119: Michael Schmidt
Prozeßregelung für das Laserstrahl-Punktschweißen in der Elektronikproduktion
LFT, 152 Seiten, 71 Bilder, 3 Tab. 2002.
ISBN 3-87525-166-0.

Band 120: Nicolas Tiesler
Grundlegende Untersuchungen zum Fließpressen metallischer Kleinstteile
LFT, 126 Seiten, 78 Bilder, 12 Tab. 2002.
ISBN 3-87525-175-X.

Band 121: Lars Pursche
Methoden zur technologieorientierten Programmierung für die 3D-Lasermikrobearbeitung
LFT, 111 Seiten, 39 Bilder, 0 Tab. 2002.
ISBN 3-87525-183-0.

Band 122: Jan-Oliver Brassel
Prozeßkontrolle beim Laserstrahl-Mikroschweißen
LFT, 148 Seiten, 72 Bilder, 12 Tab. 2002.
ISBN 3-87525-181-4.

Band 123: Mark Geisel
Prozeßkontrolle und -steuerung beim Laserstrahlschweißen mit den Methoden der nichtlinearen Dynamik
LFT, 135 Seiten, 46 Bilder, 2 Tab. 2002.
ISBN 3-87525-180-6.

Band 124: Gerd Eßer
Laserstrahlunterstützte Erzeugung metallischer Leiterstrukturen auf Thermoplastsubstraten für die MID-Technik
LFT, 148 Seiten, 60 Bilder, 6 Tab. 2002.
ISBN 3-87525-171-7.

Band 125: Marc Fleckenstein
Qualität laserstrahl-gefügter Mikroverbindungen elektronischer Kontakte
LFT, 159 Seiten, 77 Bilder, 7 Tab. 2002.
ISBN 3-87525-170-9.

Band 126: Stefan Kaufmann
Grundlegende Untersuchungen zum Nd:YAG- Laserstrahlfügen von Silizium für Komponenten der Optoelektronik
LFT, 159 Seiten, 100 Bilder, 6 Tab. 2002.
ISBN 3-87525-172-5.

Band 127: Thomas Fröhlich
Simultanes Löten von Anschlußkontakten elektronischer Bauelemente mit Diodenlaserstrahlung
LFT, 143 Seiten, 75 Bilder, 6 Tab. 2002.
ISBN 3-87525-186-5.

Band 128: Achim Hofmann
Erweiterung der Formgebungsgrenzen beim Umformen von Aluminiumwerkstoffen durch den Einsatz prozessangepasster Platinen
LFT, 113 Seiten, 58 Bilder, 4 Tab. 2002.
ISBN 3-87525-182-2.

Band 129: Ingo Kriebitzsch
3 - D MID Technologie in der Automobilelektronik
FAPS, 129 Seiten, 102 Bilder, 10 Tab. 2002.
ISBN 3-87525-169-5.

Band 130: Thomas Pohl
Fertigungsqualität und Umformbarkeit laserstrahlgeschweißter Formplatinen aus Aluminiumlegierungen
LFT, 133 Seiten, 93 Bilder, 12 Tab. 2002.
ISBN 3-87525-173-3.

Band 131: Matthias Wenk
Entwicklung eines konfigurierbaren Steuerungssystems für die flexible Sensorführung von Industrierobotern
FAPS, 167 Seiten, 85 Bilder, 1 Tab. 2002.
ISBN 3-87525-174-1.

Band 132: Matthias Negendanck
Neue Sensorik und Aktorik für Bearbeitungsköpfe zum Laserstrahlschweißen
LFT, 116 Seiten, 60 Bilder, 14 Tab. 2002.
ISBN 3-87525-184-9.

Band 133: Oliver Kreis
Integrierte Fertigung - Verfahrensintegration durch Innenhochdruck-Umformen, Trennen und Laserstrahlschweißen in einem Werkzeug sowie ihre tele- und multimediale Präsentation
LFT, 167 Seiten, 90 Bilder, 43 Tab. 2002.
ISBN 3-87525-176-8.

Band 134: Stefan Trautner
Technische Umsetzung produktbezogener Instrumente der Umweltpolitik bei Elektro- und Elektronikgeräten
FAPS, 179 Seiten, 92 Bilder, 11 Tab. 2002.
ISBN 3-87525-177-6.

Band 135: Roland Meier
Strategien für einen produktorientierten Einsatz räumlicher spritzgegossener Schaltungsträger (3-D MID)
FAPS, 155 Seiten, 88 Bilder, 14 Tab. 2002.
ISBN 3-87525-178-4.

Band 136: Jürgen Wunderlich
Kostensimulation - Simulationsbasierte Wirtschaftlichkeitsregelung komplexer Produktionssysteme
FAPS, 202 Seiten, 119 Bilder, 17 Tab. 2002.
ISBN 3-87525-179-2.

Band 137: Stefan Novotny
Innenhochdruck-Umformen von Blechen aus Aluminium- und Magnesiumlegierungen bei erhöhter Temperatur
LFT, 132 Seiten, 82 Bilder, 6 Tab. 2002.
ISBN 3-87525-185-7.

Band 138: Andreas Licha
Flexible Montageautomatisierung zur Komplettmontage flächenhafter Produktstrukturen durch kooperierende Industrieroboter
FAPS, 158 Seiten, 87 Bilder, 8 Tab. 2003.
ISBN 3-87525-189-X.

Band 139: Michael Eisenbarth
Beitrag zur Optimierung der Aufbau- und Verbindungstechnik für mechatronische Baugruppen
FAPS, 207 Seiten, 141 Bilder, 9 Tab. 2003.
ISBN 3-87525-190-3.

Band 140: Frank Christoph
Durchgängige simulationsgestützte Planung von Fertigungseinrichtungen der Elektronikproduktion
FAPS, 187 Seiten, 107 Bilder, 9 Tab. 2003.
ISBN 3-87525-191-1.

Band 141: Hinnerk Hagenah
Simulationsbasierte Bestimmung der zu erwartenden Maßhaltigkeit für das Blechbiegen
LFT, 131 Seiten, 36 Bilder, 26 Tab. 2003.
ISBN 3-87525-192-X.

Band 142: Ralf Eckstein
Scherschneiden und Biegen metallischer Kleinstteile - Materialeinfluss und Materialverhalten
LFT, 148 Seiten, 71 Bilder, 19 Tab. 2003.
ISBN 3-87525-193-8.

Band 143: Frank H. Meyer-Pittroff
Excimerlaserstrahlbiegen dünner metallischer Folien mit homogener Lichtlinie
LFT, 138 Seiten, 60 Bilder, 16 Tab. 2003.
ISBN 3-87525-196-2.

Band 144: Andreas Kach
Rechnergestützte Anpassung von Laserstrahlschneidbahnen an Bauteilabweichungen
LFT, 139 Seiten, 69 Bilder, 11 Tab. 2004.
ISBN 3-87525-197-0.

Band 145: Stefan Hierl
System- und Prozeßtechnik für das simultane Löten mit Diodenlaserstrahlung von elektronischen Bauelementen
LFT, 124 Seiten, 66 Bilder, 4 Tab. 2004.
ISBN 3-87525-198-9.

Band 146: Thomas Neudecker
Tribologische Eigenschaften keramischer Blechumformwerkzeuge- Einfluss einer Oberflächenendbearbeitung mittels Excimerlaserstrahlung
LFT, 166 Seiten, 75 Bilder, 26 Tab. 2004.
ISBN 3-87525-200-4.

Band 147: Ulrich Wenger
Prozessoptimierung in der Wickeltechnik durch innovative maschinenbauliche und regelungstechnische Ansätze
FAPS, 132 Seiten, 88 Bilder, 0 Tab. 2004.
ISBN 3-87525-203-9.

Band 148: Stefan Slama
Effizienzsteigerung in der Montage durch marktorientierte Montagestrukturen und erweiterte Mitarbeiterkompetenz
FAPS, 188 Seiten, 125 Bilder, 0 Tab. 2004.
ISBN 3-87525-204-7.

Band 149: Thomas Wurm
Laserstrahljustieren mittels Aktoren-Entwicklung von Konzepten und Methoden für die rechnerunterstützte Modellierung und Optimierung von komplexen Aktorsystemen in der Mikrotechnik
LFT, 122 Seiten, 51 Bilder, 9 Tab. 2004.
ISBN 3-87525-206-3.

Band 150: Martino Celeghini
Wirkmedienbasierte Blechumformung: Grundlagenuntersuchungen zum Einfluss von Werkstoff und Bauteilgeometrie
LFT, 146 Seiten, 77 Bilder, 6 Tab. 2004.
ISBN 3-87525-207-1.

Band 151: Ralph Hohenstein
Entwurf hochdynamischer Sensor- und Regelsysteme für die adaptive Laserbearbeitung
LFT, 282 Seiten, 63 Bilder, 16 Tab. 2004.
ISBN 3-87525-210-1.

Band 152: Angelika Hutterer
Entwicklung prozessüberwachender Regelkreise für flexible Formgebungsprozesse
LFT, 149 Seiten, 57 Bilder, 2 Tab. 2005.
ISBN 3-87525-212-8.

Band 153: Emil Egerer
Massivumformen metallischer Kleinstteile bei erhöhter Prozesstemperatur
LFT, 158 Seiten, 87 Bilder, 10 Tab. 2005.
ISBN 3-87525-213-6.

Band 154: Rüdiger Holzmann
Strategien zur nachhaltigen Optimierung von Qualität und Zuverlässigkeit in der Fertigung hochintegrierter Flachbaugruppen
FAPS, 186 Seiten, 99 Bilder, 19 Tab. 2005.
ISBN 3-87525-217-9.

Band 155: Marco Nock
Biegeumformen mit Elastomerwerkzeugen Modellierung, Prozessauslegung und Abgrenzung des Verfahrens am Beispiel des Rohrbiegens
LFT, 164 Seiten, 85 Bilder, 13 Tab. 2005.
ISBN 3-87525-218-7.

Band 156: Frank Niebling
Qualifizierung einer Prozesskette zum Laserstrahlsintern metallischer Bauteile
LFT, 148 Seiten, 89 Bilder, 3 Tab. 2005.
ISBN 3-87525-219-5.

Band 157: Markus Meiler
Großserientauglichkeit trockenschmierstoffbeschichteter Aluminiumbleche im Presswerk Grundlegende Untersuchungen zur Tribologie, zum Umformverhalten und Bauteilversuche
LFT, 104 Seiten, 57 Bilder, 21 Tab. 2005.
ISBN 3-87525-221-7.

Band 158: Agus Sutanto
Solution Approaches for Planning of Assembly Systems in Three-Dimensional Virtual Environments
FAPS, 169 Seiten, 98 Bilder, 3 Tab. 2005.
ISBN 3-87525-220-9.

Band 159: Matthias Boiger
Hochleistungssysteme für die Fertigung elektronischer Baugruppen auf der Basis flexibler Schaltungsträger
FAPS, 175 Seiten, 111 Bilder, 8 Tab. 2005.
ISBN 3-87525-222-5.

Band 160: Matthias Pitz
Laserunterstütztes Biegen höchstfester Mehrphasenstähle
LFT, 120 Seiten, 73 Bilder, 11 Tab. 2005.
ISBN 3-87525-223-3.

Band 161: Meik Vahl
Beitrag zur gezielten Beeinflussung des Werkstoffflusses beim Innenhochdruck-Umformen von Blechen
LFT, 165 Seiten, 94 Bilder, 15 Tab. 2005.
ISBN 3-87525-224-1.

Band 162: Peter K. Kraus
Plattformstrategien - Realisierung einer varianz- und kostenoptimierten Wertschöpfung
FAPS, 181 Seiten, 95 Bilder, 0 Tab. 2005.
ISBN 3-87525-226-8.

Band 163: Adrienn Cser
Laserstrahlschmelzabtrag - Prozessanalyse und -modellierung
LFT, 146 Seiten, 79 Bilder, 3 Tab. 2005.
ISBN 3-87525-227-6.

Band 164: Markus C. Hahn
Grundlegende Untersuchungen zur Herstellung von Leichtbauverbundstrukturen mit Aluminiumschaumkern
LFT, 143 Seiten, 60 Bilder, 16 Tab. 2005.
ISBN 3-87525-228-4.

Band 165: Gordana Michos
Mechatronische Ansätze zur Optimierung von Vorschubachsen
FAPS, 146 Seiten, 87 Bilder, 17 Tab. 2005.
ISBN 3-87525-230-6.

Band 166: Markus Stark
Auslegung und Fertigung hochpräziser Faser-Kollimator-Arrays
LFT, 158 Seiten, 115 Bilder, 11 Tab. 2005.
ISBN 3-87525-231-4.

Band 167: Yurong Zhou
Kollaboratives Engineering Management in der integrierten virtuellen Entwicklung der Anlagen für die Elektronikproduktion
FAPS, 156 Seiten, 84 Bilder, 6 Tab. 2005.
ISBN 3-87525-232-2.

Band 168: Werner Enser
Neue Formen permanenter und lösbarer elektrischer Kontaktierungen für mechatronische Baugruppen
FAPS, 190 Seiten, 112 Bilder, 5 Tab. 2005.
ISBN 3-87525-233-0.

Band 169: Katrin Melzer
Integrierte Produktpolitik bei elektrischen und elektronischen Geräten zur Optimierung des Product-Life-Cycle
FAPS, 155 Seiten, 91 Bilder, 17 Tab. 2005.
ISBN 3-87525-234-9.

Band 170: Alexander Putz
Grundlegende Untersuchungen zur Erfassung der realen Vorspannung von armierten Kaltfließpresswerkzeugen mittels Ultraschall
LFT, 137 Seiten, 71 Bilder, 15 Tab. 2006.
ISBN 3-87525-237-3.

Band 171: Martin Prechtl
Automatisiertes Schichtverfahren für metallische Folien - System- und Prozesstechnik
LFT, 154 Seiten, 45 Bilder, 7 Tab. 2006.
ISBN 3-87525-238-1.

Band 172: Markus Meidert
Beitrag zur deterministischen Lebensdauerabschätzung von Werkzeugen der Kaltmassivumformung
LFT, 131 Seiten, 78 Bilder, 9 Tab. 2006.
ISBN 3-87525-239-X.

Band 173: Bernd Müller
Robuste, automatisierte Montagesysteme durch adaptive Prozessführung und montageübergreifende Fehlerprävention am Beispiel flächiger Leichtbauteile
FAPS, 147 Seiten, 77 Bilder, 0 Tab. 2006.
ISBN 3-87525-240-3.

Band 174: Alexander Hofmann
Hybrides Laserdurchstrahlschweißen von Kunststoffen
LFT, 136 Seiten, 72 Bilder, 4 Tab. 2006.
ISBN 978-3-87525-243-9.

Band 175: Peter Wölflick
Innovative Substrate und Prozesse mit feinsten Strukturen für bleifreie Mechatronik-Anwendungen
FAPS, 177 Seiten, 148 Bilder, 24 Tab. 2006.
ISBN 978-3-87525-246-0.

Band 176: Attila Komlodi
Detection and Prevention of Hot Cracks during Laser Welding of Aluminium Alloys Using Advanced Simulation Methods
LFT, 155 Seiten, 89 Bilder, 14 Tab. 2006.
ISBN 978-3-87525-248-4.

Band 177: Uwe Popp
Grundlegende Untersuchungen zum Laserstrahlstrukturieren von Kaltmassivumformwerkzeugen
LFT, 140 Seiten, 67 Bilder, 16 Tab. 2006.
ISBN 978-3-87525-249-1.

Band 178: Veit Rückel
Rechnergestützte Ablaufplanung und Bahngenerierung Für kooperierende Industrieroboter
FAPS, 148 Seiten, 75 Bilder, 7 Tab. 2006.
ISBN 978-3-87525-250-7.

Band 179: Manfred Dirscherl
Nicht-thermische Mikrojustiertechnik mittels ultrakurzer Laserpulse
LFT, 154 Seiten, 69 Bilder, 10 Tab. 2007.
ISBN 978-3-87525-251-4.

Band 180: Yong Zhuo
Entwurf eines rechnergestützten integrierten Systems für Konstruktion und Fertigungsplanung räumlicher spritzgegossener Schaltungsträger (3D-MID)
FAPS, 181 Seiten, 95 Bilder, 5 Tab. 2007.
ISBN 978-3-87525-253-8.

Band 181: Stefan Lang
Durchgängige Mitarbeiterinformation zur Steigerung von Effizienz und Prozesssicherheit in der Produktion
FAPS, 172 Seiten, 93 Bilder. 2007.
ISBN 978-3-87525-257-6.

Band 182: Hans-Joachim Krauß
Laserstrahlinduzierte Pyrolyse präkeramischer Polymere
LFT, 171 Seiten, 100 Bilder. 2007.
ISBN 978-3-87525-258-3.

Band 183: Stefan Junker
Technologien und Systemlösungen für die flexibel automatisierte Bestückung permanent erregter Läufer mit oberflächenmontierten Dauermagneten
FAPS, 173 Seiten, 75 Bilder. 2007.
ISBN 978-3-87525-259-0.

Band 184: Rainer Kohlbauer
Wissensbasierte Methoden für die simulationsgestützte Auslegung wirkmedienbasierter Blechumformprozesse
LFT, 135 Seiten, 50 Bilder. 2007.
ISBN 978-3-87525-260-6.

Band 185: Klaus Lamprecht
Wirkmedienbasierte Umformung tiefgezogener Vorformen unter besonderer Berücksichtigung maßgeschneiderter Halbzeuge
LFT, 137 Seiten, 81 Bilder. 2007.
ISBN 978-3-87525-265-1.

Band 186: Bernd Zolleiß
Optimierte Prozesse und Systeme für die Bestückung mechatronischer Baugruppen
FAPS, 180 Seiten, 117 Bilder. 2007.
ISBN 978-3-87525-266-8.

Band 187: Michael Kerausch
Simulationsgestützte Prozessauslegung für das Umformen lokal wärmebehandelter Aluminiumplatinen
LFT, 146 Seiten, 76 Bilder, 7 Tab. 2007.
ISBN 978-3-87525-267-5.

Band 188: Matthias Weber
Unterstützung der Wandlungsfähigkeit von Produktionsanlagen durch innovative Softwaresysteme
FAPS, 183 Seiten, 122 Bilder, 3 Tab. 2007.
ISBN 978-3-87525-269-9.

Band 189: Thomas Frick
Untersuchung der prozessbestimmenden Strahl-Stoff-Wechselwirkungen beim Laserstrahlschweißen von Kunststoffen
LFT, 104 Seiten, 62 Bilder, 8 Tab. 2007.
ISBN 978-3-87525-268-2.

Band 190: Joachim Hecht
Werkstoffcharakterisierung und Prozessauslegung für die wirkmedienbasierte Doppelblech-Umformung von Magnesiumlegierungen
LFT, 107 Seiten, 91 Bilder, 2 Tab. 2007.
ISBN 978-3-87525-270-5.

Band 191: Ralf Völkl
Stochastische Simulation zur Werkzeuglebensdaueroptimierung und Präzisionsfertigung in der Kaltmassivumformung
LFT, 178 Seiten, 75 Bilder, 12 Tab. 2008.
ISBN 978-3-87525-272-9.

Band 192: Massimo Tolazzi
Innenhochdruck-Umformen verstärkter Blech-Rahmenstrukturen
LFT, 164 Seiten, 85 Bilder, 7 Tab. 2008.
ISBN 978-3-87525-273-6.

Band 193: Cornelia Hoff
Untersuchung der Prozesseinflussgrößen beim Presshärten des höchstfesten Vergütungsstahls 22MnB5
LFT, 133 Seiten, 92 Bilder, 5 Tab. 2008.
ISBN 978-3-87525-275-0.

Band 194: Christian Alvarez
Simulationsgestützte Methoden zur effizienten Gestaltung von Lötprozessen in der Elektronikproduktion
FAPS, 149 Seiten, 86 Bilder, 8 Tab. 2008.
ISBN 978-3-87525-277-4.

Band 195: Andreas Kunze
Automatisierte Montage von makromechatronischen Modulen zur flexiblen Integration in hybride Pkw-Bordnetzsysteme
FAPS, 160 Seiten, 90 Bilder, 14 Tab. 2008.
ISBN 978-3-87525-278-1.

Band 196: Wolfgang Hußnätter
Grundlegende Untersuchungen zur experimentellen Ermittlung und zur Modellierung von Fließortkurven bei erhöhten Temperaturen
LFT, 152 Seiten, 73 Bilder, 21 Tab. 2008.
ISBN 978-3-87525-279-8.

Band 197: Thomas Bigl
Entwicklung, angepasste Herstellungsverfahren und erweiterte Qualitätssicherung von einsatzgerechten elektronischen Baugruppen
FAPS, 175 Seiten, 107 Bilder, 14 Tab. 2008.
ISBN 978-3-87525-280-4.

Band 198: Stephan Roth
Grundlegende Untersuchungen zum Excimerlaserstrahl-Abtragen unter Flüssigkeitsfilmen
LFT, 113 Seiten, 47 Bilder, 14 Tab. 2008.
ISBN 978-3-87525-281-1.

Band 199: Artur Giera
Prozesstechnische Untersuchungen zum Rührreibschweißen metallischer Werkstoffe
LFT, 179 Seiten, 104 Bilder, 36 Tab. 2008.
ISBN 978-3-87525-282-8.

Band 200: Jürgen Lechler
Beschreibung und Modellierung des Werkstoffverhaltens von presshärtbaren Bor-Manganstählen
LFT, 154 Seiten, 75 Bilder, 12 Tab. 2009.
ISBN 978-3-87525-286-6.

Band 201: Andreas Blankl
Untersuchungen zur Erhöhung der Prozessrobustheit bei der Innenhochdruck-Umformung von flächigen Halbzeugen mit vor- bzw. nachgeschalteten Laserstrahlfügeoperationen
LFT, 120 Seiten, 68 Bilder, 9 Tab. 2009.
ISBN 978-3-87525-287-3.

Band 202: Andreas Schaller
Modellierung eines nachfrageorientierten Produktionskonzeptes für mobile Telekommunikationsgeräte
FAPS, 120 Seiten, 79 Bilder, 0 Tab. 2009.
ISBN 978-3-87525-289-7.

Band 203: Claudius Schimpf
Optimierung von Zuverlässigkeitsuntersuchungen, Prüfabläufen und Nacharbeitsprozessen in der Elektronikproduktion
FAPS, 162 Seiten, 90 Bilder, 14 Tab. 2009.
ISBN 978-3-87525-290-3.

Band 204: Simon Dietrich
Sensoriken zur Schwerpunktslagebestimmung der optischen Prozessemissionen beim Laserstrahltiefschweißen
LFT, 138 Seiten, 70 Bilder, 5 Tab. 2009.
ISBN 978-3-87525-292-7.

Band 205: Wolfgang Wolf
Entwicklung eines agentenbasierten Steuerungssystems zur Materialflussorganisation im wandelbaren Produktionsumfeld
FAPS, 167 Seiten, 98 Bilder. 2009.
ISBN 978-3-87525-293-4.

Band 206: Steffen Polster
Laserdurchstrahlschweißen transparenter Polymerbauteile
LFT, 160 Seiten, 92 Bilder, 13 Tab. 2009.
ISBN 978-3-87525-294-1.

Band 207: Stephan Manuel Dörfler
Rührreibschweißen von walzplattiertem Halbzeug und Aluminiumblech zur Herstellung flächiger Aluminiumschaum-Sandwich-Verbundstrukturen
LFT, 190 Seiten, 98 Bilder, 5 Tab. 2009.
ISBN 978-3-87525-295-8.

Band 208: Uwe Vogt
Seriennahe Auslegung von Aluminium Tailored Heat Treated Blanks
LFT, 151 Seiten, 68 Bilder, 26 Tab. 2009.
ISBN 978-3-87525-296-5.

Band 209: Till Laumann
Qualitative und quantitative Bewertung der Crashtauglichkeit von höchstfesten Stählen
LFT, 117 Seiten, 69 Bilder, 7 Tab. 2009.
ISBN 978-3-87525-299-6.

Band 210: Alexander Diehl
Größeneffekte bei Biegeprozessen- Entwicklung einer Methodik zur Identifikation und Quantifizierung
LFT, 180 Seiten, 92 Bilder, 12 Tab. 2010.
ISBN 978-3-87525-302-3.

Band 211: Detlev Staud
Effiziente Prozesskettenauslegung für das Umformen lokal wärmebehandelter und geschweißter Aluminiumbleche
LFT, 164 Seiten, 72 Bilder, 12 Tab. 2010.
ISBN 978-3-87525-303-0.

Band 212: Jens Ackermann
Prozesssicherung beim Laserdurchstrahlschweißen thermoplastischer Kunststoffe
LPT, 129 Seiten, 74 Bilder, 13 Tab. 2010.
ISBN 978-3-87525-305-4.

Band 213: Stephan Weidel
Grundlegende Untersuchungen zum Kontaktzustand zwischen Werkstück und Werkzeug bei umformtechnischen Prozessen unter tribologischen Gesichtspunkten
LFT, 144 Seiten, 67 Bilder, 11 Tab. 2010.
ISBN 978-3-87525-307-8.

Band 214: Stefan Geißdörfer
Entwicklung eines mesoskopischen Modells zur Abbildung von Größeneffekten in der Kaltmassivumformung mit Methoden der FE-Simulation
LFT, 133 Seiten, 83 Bilder, 11 Tab. 2010.
ISBN 978-3-87525-308-5.

Band 215: Christian Matzner
Konzeption produktspezifischer Lösungen zur Robustheitssteigerung elektronischer Systeme gegen die Einwirkung von Betauung im Automobil
FAPS, 165 Seiten, 93 Bilder, 14 Tab. 2010.
ISBN 978-3-87525-309-2.

Band 216: Florian Schüßler
Verbindungs- und Systemtechnik für thermisch hochbeanspruchte und miniaturisierte elektronische Baugruppen
FAPS, 184 Seiten, 93 Bilder, 18 Tab. 2010.
ISBN 978-3-87525-310-8.

Band 217: Massimo Cojutti
Strategien zur Erweiterung der Prozessgrenzen bei der Innhochdruck-Umformung von Rohren und Blechpaaren
LFT, 125 Seiten, 56 Bilder, 9 Tab. 2010.
ISBN 978-3-87525-312-2.

Band 218: Raoul Plettke
Mehrkriterielle Optimierung komplexer Aktorsysteme für das Laserstrahljustieren
LFT, 152 Seiten, 25 Bilder, 3 Tab. 2010.
ISBN 978-3-87525-315-3.

Band 219: Andreas Dobroschke
Flexible Automatisierungslösungen für die Fertigung wickeltechnischer Produkte
FAPS, 184 Seiten, 109 Bilder, 18 Tab. 2011.
ISBN 978-3-87525-317-7.

Band 220: Azhar Zam
Optical Tissue Differentiation for Sensor-Controlled Tissue-Specific Laser Surgery
LPT, 99 Seiten, 45 Bilder, 8 Tab. 2011.
ISBN 978-3-87525-318-4.

Band 221: Michael Rösch
Potenziale und Strategien zur Optimierung des Schablonendruckprozesses in der Elektronikproduktion
FAPS, 192 Seiten, 127 Bilder, 19 Tab. 2011.
ISBN 978-3-87525-319-1.

Band 222: Thomas Rechtenwald
Quasi-isothermes Laserstrahlsintern von Hochtemperatur-Thermoplasten - Eine Betrachtung werkstoff-prozessspezifischer Aspekte am Beispiel PEEK
LPT, 150 Seiten, 62 Bilder, 8 Tab. 2011.
ISBN 978-3-87525-320-7.

Band 223: Daniel Craiovan
Prozesse und Systemlösungen für die SMT-Montage optischer Bauelemente auf Substrate mit integrierten Lichtwellenleitern
FAPS, 165 Seiten, 85 Bilder, 8 Tab. 2011.
ISBN 978-3-87525-324-5.

Band 224: Kay Wagner
Beanspruchungsangepasste Kaltmassivumformwerkzeuge durch lokal optimierte Werkzeugoberflächen
LFT, 147 Seiten, 103 Bilder, 17 Tab. 2011.
ISBN 978-3-87525-325-2.

Band 225: Martin Brandhuber
Verbesserung der Prognosegüte des Versagens von Punktschweißverbindungen bei höchstfesten Stahlgüten
LFT, 155 Seiten, 91 Bilder, 19 Tab. 2011.
ISBN 978-3-87525-327-6.

Band 226: Peter Sebastian Feuser
Ein Ansatz zur Herstellung von pressgehärteten Karosseriekomponenten mit maßgeschneiderten mechanischen Eigenschaften: Temperierte Umformwerkzeuge. Prozessfenster, Prozesssimuation und funktionale Untersuchung
LFT, 195 Seiten, 97 Bilder, 60 Tab. 2012.
ISBN 978-3-87525-328-3.

Band 227: Murat Arbak
Material Adapted Design of Cold Forging Tools Exemplified by Powder Metallurgical Tool Steels and Ceramics
LFT, 109 Seiten, 56 Bilder, 8 Tab. 2012.
ISBN 978-3-87525-330-6.

Band 228: Indra Pitz
Beschleunigte Simulation des Laserstrahlumformens von Aluminiumblechen
LPT, 137 Seiten, 45 Bilder, 27 Tab. 2012.
ISBN 978-3-87525-333-7.

Band 229: Alexander Grimm
Prozessanalyse und -überwachung des Laserstrahlhartlötens mittels optischer Sensorik
LPT, 125 Seiten, 61 Bilder, 5 Tab. 2012.
ISBN 978-3-87525-334-4.

Band 230: Markus Kaupper
Biegen von höhenfesten Stahlblechwerkstoffen - Umformverhalten und Grenzen der Biegbarkeit
LFT, 160 Seiten, 57 Bilder, 10 Tab. 2012.
ISBN 978-3-87525-339-9.

Band 231: Thomas Kroiß
Modellbasierte Prozessauslegung für die Kaltmassivumformung unter Brücksichtigung der Werkzeug- und Pressenauffederung
LFT, 169 Seiten, 50 Bilder, 19 Tab. 2012.
ISBN 978-3-87525-341-2.

Band 232: Christian Goth
Analyse und Optimierung der Entwicklung und Zuverlässigkeit räumlicher Schaltungsträger (3D-MID)
FAPS, 176 Seiten, 102 Bilder, 22 Tab. 2012.
ISBN 978-3-87525-340-5.

Band 233: Christian Ziegler
Ganzheitliche Automatisierung mechatronischer Systeme in der Medizin am Beispiel Strahlentherapie
FAPS, 170 Seiten, 71 Bilder, 19 Tab. 2012.
ISBN 978-3-87525-342-9.

Band 234: Florian Albert
Automatisiertes Laserstrahllöten und -reparaturlöten elektronischer Baugruppen
LPT, 127 Seiten, 78 Bilder, 11 Tab. 2012.
ISBN 978-3-87525-344-3.

Band 235: Thomas Stöhr
Analyse und Beschreibung des mechanischen Werkstoffverhaltens von presshärtbaren Bor-Manganstählen
LFT, 118 Seiten, 74 Bilder, 18 Tab. 2013.
ISBN 978-3-87525-346-7.

Band 236: Christian Kägeler
Prozessdynamik beim Laserstrahlschweißen verzinkter Stahlbleche im Überlappstoß
LPT, 145 Seiten, 80 Bilder, 3 Tab. 2013.
ISBN 978-3-87525-347-4.

Band 237: Andreas Sulzberger
Seriennahe Auslegung der Prozesskette zur wärmeunterstützten Umformung von Aluminiumblechwerkstoffen
LFT, 153 Seiten, 87 Bilder, 17 Tab. 2013.
ISBN 978-3-87525-349-8.

Band 238: Simon Opel
Herstellung prozessangepasster Halbzeuge mit variabler Blechdicke durch die Anwendung von Verfahren der Blechmassivumformung
LFT, 165 Seiten, 108 Bilder, 27 Tab. 2013.
ISBN 978-3-87525-350-4.

Band 239: Rajesh Kanawade
In-vivo Monitoring of Epithelium Vessel and Capillary Density for the Application of Detection of Clinical Shock and Early Signs of Cancer Development
LPT, 124 Seiten, 58 Bilder, 15 Tab. 2013.
ISBN 978-3-87525-351-1.

Band 240: Stephan Busse
Entwicklung und Qualifizierung eines Schneidclinchverfahrens
LFT, 119 Seiten, 86 Bilder, 20 Tab. 2013.
ISBN 978-3-87525-352-8.

Band 241: Karl-Heinz Leitz
Mikro- und Nanostrukturierung mit kurz und ultrakurz gepulster Laserstrahlung
LPT, 154 Seiten, 71 Bilder, 9 Tab. 2013.
ISBN 978-3-87525-355-9.

Band 242: Markus Michl
Webbasierte Ansätze zur ganzheitlichen technischen Diagnose
FAPS, 182 Seiten, 62 Bilder, 20 Tab. 2013.
ISBN 978-3-87525-356-6.

Band 243: Vera Sturm
Einfluss von Chargenschwankungen auf die Verarbeitungsgrenzen von Stahlwerkstoffen
LFT, 113 Seiten, 58 Bilder, 9 Tab. 2013.
ISBN 978-3-87525-357-3.

Band 244: Christian Neudel
Mikrostrukturelle und mechanisch-technologische Eigenschaften widerstandspunktgeschweißter Aluminium-Stahl-Verbindungen für den Fahrzeugbau
LFT, 178 Seiten, 171 Bilder, 31 Tab. 2014.
ISBN 978-3-87525-358-0.

Band 245: Anja Neumann
Konzept zur Beherrschung der Prozessschwankungen im Presswerk
LFT, 162 Seiten, 68 Bilder, 15 Tab. 2014.
ISBN 978-3-87525-360-3.

Band 246: Ulf-Hermann Quentin
Laserbasierte Nanostrukturierung mit optisch positionierten Mikrolinsen
LPT, 137 Seiten, 89 Bilder, 6 Tab. 2014.
ISBN 978-3-87525-361-0.

Band 247: Erik Lamprecht
Der Einfluss der Fertigungsverfahren auf die Wirbelstromverluste von Stator-Einzelzahnblechpaketen für den Einsatz in Hybrid- und Elektrofahrzeugen
FAPS, 148 Seiten, 138 Bilder, 4 Tab. 2014.
ISBN 978-3-87525-362-7.

Band 248: Sebastian Rösel
Wirkmedienbasierte Umformung von Blechhalbzeugen unter Anwendung magnetorheologischer Flüssigkeiten als kombiniertes Wirk- und Dichtmedium
LFT, 148 Seiten, 61 Bilder, 12 Tab. 2014.
ISBN 978-3-87525-363-4.

Band 249: Paul Hippchen
Simulative Prognose der Geometrie indirekt pressgehärteter Karosseriebauteile für die industrielle Anwendung
LFT, 163 Seiten, 89 Bilder, 12 Tab. 2014.
ISBN 978-3-87525-364-1.

Band 250: Martin Zubeil
Versagensprognose bei der Prozess simulation von Biegeumform- und Falzverfahren
LFT, 171 Seiten, 90 Bilder, 5 Tab. 2014.
ISBN 978-3-87525-365-8.

Band 251: Alexander Kühl
Flexible Automatisierung der Statorenmontage mit Hilfe einer universellen ambidexteren Kinematik
FAPS, 142 Seiten, 60 Bilder, 26 Tab. 2014.
ISBN 978-3-87525-367-2.

Band 252: Thomas Albrecht
Optimierte Fertigungstechnologien für Rotoren getriebeintegrierter PM-Synchronmotoren von Hybridfahrzeugen
FAPS, 198 Seiten, 130 Bilder, 38 Tab. 2014.
ISBN 978-3-87525-368-9.

Band 253: Florian Risch
Planning and Production Concepts for Contactless Power Transfer Systems for Electric Vehicles
FAPS, 185 Seiten, 125 Bilder, 13 Tab. 2014.
ISBN 978-3-87525-369-6.

Band 254: Markus Weigl
Laserstrahlschweißen von Mischverbindungen aus austenitischen und ferritischen korrosionsbeständigen Stahlwerkstoffen
LPT, 184 Seiten, 110 Bilder, 6 Tab. 2014.
ISBN 978-3-87525-370-2.

Band 255: Johannes Noneder
Beanspruchungserfassung für die Validierung von FE-Modellen zur Auslegung von Massivumformwerkzeugen
LFT, 161 Seiten, 65 Bilder, 14 Tab. 2014.
ISBN 978-3-87525-371-9.

Band 256: Andreas Reinhardt
Ressourceneffiziente Prozess- und Produktionstechnologie für flexible Schaltungsträger
FAPS, 123 Seiten, 69 Bilder, 19 Tab. 2014.
ISBN 978-3-87525-373-3.

Band 257: Tobias Schmuck
Ein Beitrag zur effizienten Gestaltung globaler Produktions- und Logistiknetzwerke mittels Simulation
FAPS, 151 Seiten, 74 Bilder. 2014.
ISBN 978-3-87525-374-0.

Band 258: Bernd Eichenhüller
Untersuchungen der Effekte und Wechselwirkungen charakteristischer Einflussgrößen auf das Umformverhalten bei Mikroumformprozessen
LFT, 127 Seiten, 29 Bilder, 9 Tab. 2014.
ISBN 978-3-87525-375-7.

Band 259: Felix Lütteke
Vielseitiges autonomes Transportsystem basierend auf Weltmodellerstellung mittels Datenfusion von Deckenkameras und Fahrzeugsensoren
FAPS, 152 Seiten, 54 Bilder, 20 Tab. 2014.
ISBN 978-3-87525-376-4.

Band 260: Martin Grüner
Hochdruck-Blechumformung mit formlos festen Stoffen als Wirkmedium
LFT, 144 Seiten, 66 Bilder, 29 Tab. 2014.
ISBN 978-3-87525-379-5.

Band 261: Christian Brock
Analyse und Regelung des Laserstrahltiefschweißprozesses durch Detektion der Metalldampffackelposition
LPT, 126 Seiten, 65 Bilder, 3 Tab. 2015.
ISBN 978-3-87525-380-1.

Band 262: Peter Vatter
Sensitivitätsanalyse des 3-Rollen-Schubbiegens auf Basis der Finite Elemente Methode
LFT, 145 Seiten, 57 Bilder, 26 Tab. 2015.
ISBN 978-3-87525-381-8.

Band 263: Florian Klämpfl
Planung von Laserbestrahlungen durch simulationsbasierte Optimierung
LPT, 169 Seiten, 78 Bilder, 32 Tab. 2015.
ISBN 978-3-87525-384-9.

Band 264: Matthias Domke
Transiente physikalische Mechanismen bei der Laserablation von dünnen Metallschichten
LPT, 133 Seiten, 43 Bilder, 3 Tab. 2015.
ISBN 978-3-87525-385-6.

Band 265: Johannes Götz
Community-basierte Optimierung des Anlagenengineerings
FAPS, 177 Seiten, 80 Bilder, 30 Tab. 2015.
ISBN 978-3-87525-386-3.

Band 266: Hung Nguyen
Qualifizierung des Potentials von Verfestigungseffekten zur Erweiterung des Umformvermögens aushärtbarer Aluminiumlegierungen
LFT, 137 Seiten, 57 Bilder, 16 Tab. 2015.
ISBN 978-3-87525-387-0.

Band 267: Andreas Kuppert
Erweiterung und Verbesserung von Versuchs- und Auswertetechniken für die Bestimmung von Grenzformänderungskurven
LFT, 138 Seiten, 82 Bilder, 2 Tab. 2015.
ISBN 978-3-87525-388-7.

Band 268: Kathleen Klaus
Erstellung eines Werkstofforientierten Fertigungsprozessfensters zur Steigerung des Formgebungsvermögens von Aluminiumlegierungen unter Anwendung einer zwischengeschalteten Wärmebehandlung
LFT, 154 Seiten, 70 Bilder, 8 Tab. 2015.
ISBN 978-3-87525-391-7.

Band 269: Thomas Svec
Untersuchungen zur Herstellung von funktionsoptimierten Bauteilen im partiellen Presshärtprozess mittels lokal unterschiedlich temperierter Werkzeuge
LFT, 166 Seiten, 87 Bilder, 15 Tab. 2015.
ISBN 978-3-87525-392-4.

Band 270: Tobias Schrader
Grundlegende Untersuchungen zur Verschleißcharakterisierung beschichteter Kaltmassivumformwerkzeuge
LFT, 164 Seiten, 55 Bilder, 11 Tab. 2015.
ISBN 978-3-87525-393-1.

Band 271: Matthäus Brela
Untersuchung von Magnetfeld-Messmethoden zur ganzheitlichen Wertschöpfungsoptimierung und Fehlerdetektion an magnetischen Aktoren
FAPS, 170 Seiten, 97 Bilder, 4 Tab. 2015.
ISBN 978-3-87525-394-8.

Band 272: Michael Wieland
Entwicklung einer Methode zur Prognose adhäsiven Verschleißes an Werkzeugen für das direkte Presshärten
LFT, 156 Seiten, 84 Bilder, 9 Tab. 2015.
ISBN 978-3-87525-395-5.

Band 273: René Schramm
Strukturierte additive Metallisierung durch kaltaktives Atmosphärendruckplasma
FAPS, 136 Seiten, 62 Bilder, 15 Tab. 2015.
ISBN 978-3-87525-396-2.

Band 274: Michael Lechner
Herstellung beanspruchungsangepasster Aluminiumblechhalbzeuge durch eine maßgeschneiderte Variation der Abkühlgeschwindigkeit nach Lösungsglühen
LFT, 136 Seiten, 62 Bilder, 15 Tab. 2015.
ISBN 978-3-87525-397-9.

Band 275: Kolja Andreas
Einfluss der Oberflächenbeschaffenheit auf das Werkzeugeinsatzverhalten beim Kaltfließpressen
LFT, 169 Seiten, 76 Bilder, 4 Tab. 2015.
ISBN 978-3-87525-398-6.

Band 276: Marcus Baum
Laser Consolidation of ITO Nanoparticles for the Generation of Thin Conductive Layers on Transparent Substrates
LPT, 158 Seiten, 75 Bilder, 3 Tab. 2015.
ISBN 978-3-87525-399-3.

Band 277: Thomas Schneider
Umformtechnische Herstellung dünnwandiger Funktionsbauteile aus Feinblech durch Verfahren der Blechmassivumformung
LFT, 188 Seiten, 95 Bilder, 7 Tab. 2015.
ISBN 978-3-87525-401-3.

Band 278: Jochen Merhof
Sematische Modellierung automatisierter Produktionssysteme zur Verbesserung der IT-Integration zwischen Anlagen-Engineering und Steuerungsebene
FAPS, 157 Seiten, 88 Bilder, 8 Tab. 2015.
ISBN 978-3-87525-402-0.

Band 279: Fabian Zöller
Erarbeitung von Grundlagen zur Abbildung des tribologischen Systems in der Umformsimulation
LFT, 126 Seiten, 51 Bilder, 3 Tab. 2016.
ISBN 978-3-87525-403-7.

Band 280: Christian Hezler
Einsatz technologischer Versuche zur Erweiterung der Versagensvorhersage bei Karosseriebauteilen aus höchstfesten Stählen
LFT, 147 Seiten, 63 Bilder, 44 Tab. 2016.
ISBN 978-3-87525-404-4.

Band 281: Jochen Bönig
Integration des Systemverhaltens von Automobil-Hochvoltleitungen in die virtuelle Absicherung durch strukturmechanische Simulation
FAPS, 177 Seiten, 107 Bilder, 17 Tab. 2016.
ISBN 978-3-87525-405-1.

Band 282: Johannes Kohl
Automatisierte Datenerfassung für diskret ereignisorientierte Simulationen in der energieflexibelen Fabrik
FAPS, 160 Seiten, 80 Bilder, 27 Tab. 2016.
ISBN 978-3-87525-406-8.

Band 283: Peter Bechtold
Mikroschockwellenumformung mittels ultrakurzer Laserpulse
LPT, 155 Seiten, 59 Bilder, 10 Tab. 2016.
ISBN 978-3-87525-407-5.

Band 284: Stefan Berger
Laserstrahlschweißen thermoplastischer Kohlenstofffaserverbundwerkstoffe mit spezifischem Zusatzdraht
LPT, 118 Seiten, 68 Bilder, 9 Tab. 2016.
ISBN 978-3-87525-408-2.

Band 285: Martin Bornschlegl
Methods-Energy Measurement - Eine Methode zur Energieplanung für Fügeverfahren im Karosseriebau
FAPS, 136 Seiten, 72 Bilder, 46 Tab. 2016.
ISBN 978-3-87525-409-9.

Band 286: Tobias Rackow
Erweiterung des Unternehmenscontrollings um die Dimension Energie
FAPS, 164 Seiten, 82 Bilder, 29 Tab. 2016.
ISBN 978-3-87525-410-5.

Band 287: Johannes Koch
Grundlegende Untersuchungen zur Herstellung zyklisch-symmetrischer Bauteile mit Nebenformelementen durch Blechmassivumformung
LFT, 125 Seiten, 49 Bilder, 17 Tab. 2016.
ISBN 978-3-87525-411-2.

Band 288: Hans Ulrich Vierzigmann
Beitrag zur Untersuchung der tribologischen Bedingungen in der Blechmassivumformung - Bereitstellung von tribologischen Modellversuchen und Realisierung von Tailored Surfaces
LFT, 174 Seiten, 102 Bilder, 34 Tab. 2016.
ISBN 978-3-87525-412-9.

Band 289: Thomas Senner
Methodik zur virtuellen Absicherung der formgebenden Operation des Nasspressprozesses von Gelege-Mehrschichtverbunden
LFT, 156 Seiten, 96 Bilder, 21 Tab. 2016.
ISBN 978-3-87525-414-3.

Band 290: Sven Kreitlein
Der grundoperationsspezifische Mindestenergiebedarf als Referenzwert zur Bewertung der Energieeffizienz in der Produktion
FAPS, 185 Seiten, 64 Bilder, 30 Tab. 2016.
ISBN 978-3-87525-415-0.

Band 291: Christian Roos
Remote-Laserstrahlschweißen verzinkter Stahlbleche in Kehlnahtgeometrie
LPT, 123 Seiten, 52 Bilder, 0 Tab. 2016.
ISBN 978-3-87525-416-7.

Band 292: Alexander Kahrimanidis
Thermisch unterstützte Umformung von Aluminiumblechen
LFT, 165 Seiten, 103 Bilder, 18 Tab. 2016.
ISBN 978-3-87525-417-4.

Band 293: Jan Tremel
Flexible Systems for Permanent Magnet Assembly and Magnetic Rotor Measurement / Flexible Systeme zur Montage von Permanentmagneten und zur Messung magnetischer Rotoren
FAPS, 152 Seiten, 91 Bilder, 12 Tab. 2016.
ISBN 978-3-87525-419-8.

Band 294: Ioannis Tsoupis
Schädigungs- und Versagensverhalten hochfester Leichtbauwerkstoffe unter Biegebeanspruchung
LFT, 176 Seiten, 51 Bilder, 6 Tab. 2017.
ISBN 978-3-87525-420-4.

Band 295: Sven Hildering
Grundlegende Untersuchungen zum Prozessverhalten von Silizium als Werkzeugwerkstoff für das Mikroscherschneiden metallischer Folien
LFT, 177 Seiten, 74 Bilder, 17 Tab. 2017.
ISBN 978-3-87525-422-8.

Band 296: Sasia Mareike Hertweck
Zeitliche Pulsformung in der Lasermikromaterialbearbeitung – Grundlegende Untersuchungen und Anwendungen
LPT, 146 Seiten, 67 Bilder, 5 Tab. 2017.
ISBN 978-3-87525-423-5.

Band 297: Paryanto
Mechatronic Simulation Approach for the Process Planning of Energy-Efficient Handling Systems
FAPS, 162 Seiten, 86 Bilder, 13 Tab. 2017.
ISBN 978-3-87525-424-2.

Band 298: Peer Stenzel
Großserientaugliche Nadelwickeltechnik für verteilte Wicklungen im Anwendungsfall der E-Traktionsantriebe
FAPS, 239 Seiten, 147 Bilder, 20 Tab. 2017.
ISBN 978-3-87525-425-9.

Band 299: Mario Lušić
Ein Vorgehensmodell zur Erstellung montageführender Werkerinformationssysteme simultan zum Produktentstehungsprozess
FAPS, 174 Seiten, 79 Bilder, 22 Tab. 2017.
ISBN 978-3-87525-426-6.

Band 300: Arnd Buschhaus
Hochpräzise adaptive Steuerung und Regelung robotergeführter Prozesse
FAPS, 202 Seiten, 96 Bilder, 4 Tab. 2017.
ISBN 978-3-87525-427-3.

Band 301: Tobias Laumer
Erzeugung von thermoplastischen Werkstoffverbunden mittels simultanem, intensitätsselektivem Laserstrahlschmelzen
LPT, 140 Seiten, 82 Bilder, 0 Tab. 2017.
ISBN 978-3-87525-428-0.

Band 302: Nora Unger
Untersuchung einer thermisch unterstützten Fertigungskette zur Herstellung umgeformter Bauteile aus der höherfesten Aluminiumlegierung EN AW-7020
LFT, 142 Seiten, 53 Bilder, 8 Tab. 2017.
ISBN 978-3-87525-429-7.

Band 303: Tommaso Stellin
Design of Manufacturing Processes for the Cold Bulk Forming of Small Metal Components from Metal Strip
LFT, 146 Seiten, 67 Bilder, 7 Tab. 2017.
ISBN 978-3-87525-430-3.

Band 304: Bassim Bachy

Experimental Investigation, Modeling, Simulation and Optimization of Molded Interconnect Devices (MID) Based on Laser Direct Structuring (LDS) / Experimentelle Untersuchung, Modellierung, Simulation und Optimierung von Molded Interconnect Devices (MID) basierend auf Laser Direktstrukturierung (LDS)

FAPS, 168 Seiten, 120 Bilder, 26 Tab. 2017.

ISBN 978-3-87525-431-0.

Band 305: Michael Spahr

Automatisierte Kontaktierungsverfahren für flachleiterbasierte Pkw-Bordnetzsysteme

FAPS, 197 Seiten, 98 Bilder, 17 Tab. 2017.

ISBN 978-3-87525-432-7.

Band 306: Sebastian Suttner

Charakterisierung und Modellierung des spannungszustandsabhängigen Werkstoffverhaltens der Magnesiumlegierung AZ31B für die numerische Prozessauslegung

LFT, 150 Seiten, 84 Bilder, 19 Tab. 2017.

ISBN 978-3-87525-433-4.

Band 307: Bhargav Potdar

A reliable methodology to deduce thermo-mechanical flow behaviour of hot stamping steels

LFT, 203 Seiten, 98 Bilder, 27 Tab. 2017.

ISBN 978-3-87525-436-5.

Band 308: Maria Löffler

Steuerung von Blechmassivumformprozessen durch maßgeschneiderte tribologische Systeme

LFT, viii u. 166 Seiten, 90 Bilder, 5 Tab. 2018. ISBN 978-3-96147-133-1.

Band 309: Martin Müller

Untersuchung des kombinierten Trenn- und Umformprozesses beim Fügen artungleicher Werkstoffe mittels Schneidclinchverfahren

LFT, xi u. 149 Seiten, 89 Bilder, 6 Tab. 2018. ISBN: 978-3-96147-135-5.

Band 310: Christopher Kästle

Qualifizierung der Kupfer-Drahtbondtechnologie für integrierte Leistungsmodule in harschen Umgebungsbedingungen

FAPS, xii u. 167 Seiten, 70 Bilder, 18 Tab. 2018. ISBN 978-3-96147-145-4.

Band 311: Daniel Vipavc

Eine Simulationsmethode für das 3-Rollen-Schubbiegen

LFT, xiii u. 121 Seiten, 56 Bilder, 17 Tab. 2018. ISBN 978-3-96147-147-8.

Band 312: Christina Ramer

Arbeitsraumüberwachung und autonome Bahnplanung für ein sicheres und flexibles Roboter-Assistenzsystem in der Fertigung

FAPS, xiv u. 188 Seiten, 57 Bilder, 9 Tab. 2018. ISBN 978-3-96147-153-9.

Band 313: Miriam Rauer

Der Einfluss von Poren auf die Zuverlässigkeit der Lötverbindungen von Hochleistungs-Leuchtdioden

FAPS, xii u. 209 Seiten, 108 Bilder, 21 Tab. 2018. ISBN 978-3-96147-157-7.

Band 314: Felix Tenner

Kamerabasierte Untersuchungen der Schmelze und Gasströmungen beim Laserstrahlschweißen verzinkter Stahlbleche

LPT, xxiii u. 184 Seiten, 94 Bilder, 7 Tab.
2018. ISBN 978-3-96147-160-7.

Band 315: Aarief Syed-Khaja

Diffusion Soldering for High-temperature Packaging of Power Electronics

FAPS, x u. 202 Seiten, 144 Bilder, 32 Tab.
2018. ISBN 978-3-87525-162-1.

Band 316: Adam Schaub

Grundlagenwissenschaftliche Untersuchung der kombinierten Prozesskette aus Umformen und Additive Fertigung

LFT, xi u. 192 Seiten, 72 Bilder, 27 Tab.
2019. ISBN 978-3-96147-166-9.

Band 317: Daniel Gröbel

Herstellung von Nebenformelementen unterschiedlicher Geometrie an Blechen mittels Fließpressverfahren der Blechmassivumformung

LFT, x u. 165 Seiten, 96 Bilder, 13 Tab.
2019. ISBN 978-3-96147-168-3.

Band 318: Philipp Hildenbrand

Entwicklung einer Methodik zur Herstellung von Tailored Blanks mit definierten Halbzeugeigenschaften durch einen Taumelprozess

LFT, ix u. 153 Seiten, 77 Bilder, 4 Tab.
2019. ISBN 978-3-96147-174-4.

Band 319: Tobias Konrad

Simulative Auslegung der Spann- und Fixierkonzepte im Karosserierohbau: Bewertung der Baugruppenmaßhaltigkeit unter Berücksichtigung schwankender Einflussgrößen

LFT, x u. 203 Seiten, 134 Bilder, 32 Tab.
2019. ISBN 978-3-96147-176-8.

Band 320: David Meinel

Architektur applikationsspezifischer Multi-Physics-Simulationskonfiguratoren am Beispiel modularer Triebzüge

FAPS, xii u. 166 Seiten, 82 Bilder, 25 Tab.
2019. ISBN 978-3-96147-184-3.

Band 321: Andrea Zimmermann

Grundlegende Untersuchungen zum Einfluss fertigungsbedingter Eigenschaften auf die Ermüdungsfestigkeit kaltmassivumgeformter Bauteile

LFT, ix u. 160 Seiten, 66 Bilder, 5 Tab.
2019. ISBN 978-3-96147-190-4.

Band 322: Christoph Amann

Simulative Prognose der Geometrie nassgepresster Karosseriebauteile aus Gelege-Mehrschichtverbunden

LFT, xvi u. 169 Seiten, 80 Bilder, 13 Tab.
2019. ISBN 978-3-96147-194-2.

Band 323: Jennifer Tenner

Realisierung schmierstofffreier Tiefziehprozesse durch maßgeschneiderte Werkzeugoberflächen

LFT, x u. 187 Seiten, 68 Bilder, 13 Tab.
2019. ISBN 978-3-96147-196-6.

Band 324: Susan Zöller

Mapping Individual Subjective Values to Product Design

KTmfk, xi u. 223 Seiten, 81 Bilder, 25 Tab.
2019. ISBN 978-3-96147-202-4.

Band 325: Stefan Lutz
Erarbeitung einer Methodik zur semiempirischen Ermittlung der Umwandlungskinetik durchhärtender Wälzlagerstähle für die Wärmebehandlungssimulation
LFT, xiv u. 189 Seiten, 75 Bilder, 32 Tab.
2019. ISBN 978-3-96147-209-3.

Band 326: Tobias Gnibl
Modellbasierte Prozesskettenabbildung rührreibgeschweißter Aluminiumhalbzeuge zur umformtechnischen Herstellung höchstfester Leichtbaustrukturteile
LFT, xii u. 167 Seiten, 68 Bilder, 17 Tab.
2019. ISBN 978-3-96147-217-8.

Band 327: Johannes Bürner
Technisch-wirtschaftliche Optionen zur Lastflexibilisierung durch intelligente elektrische Wärmespeicher
FAPS, xiv u. 233 Seiten, 89 Bilder, 27 Tab.
2019. ISBN 978-3-96147-219-2.

Band 328: Wolfgang Böhm
Verbesserung des Umformverhaltens von mehrlagigen Aluminiumblechwerkstoffen mit ultrafeinkörnigem Gefüge
LFT, ix u. 160 Seiten, 88 Bilder, 14 Tab.
2019. ISBN 978-3-96147-227-7.

Band 329: Stefan Landkammer
Grundsatzuntersuchungen, mathematische Modellierung und Ableitung einer Auslegungsmethodik für Gelenkantriebe nach dem Spinnenbeinprinzip
LFT, xii u. 200 Seiten, 83 Bilder, 13 Tab.
2019. ISBN 978-3-96147-229-1.

Band 330: Stephan Rapp
Pump-Probe-Ellipsometrie zur Messung transienter optischer Materialeigenschaften bei der Ultrakurzpuls-Lasermaterialbearbeitung
LPT, xi u. 143 Seiten, 49 Bilder, 2 Tab.
2019. ISBN 978-3-96147-235-2.

Band 331: Michael Scholz
Intralogistics Execution System mit integrierten autonomen, servicebasierten Transportentitäten
FAPS, xi u. 195 Seiten, 55 Bilder, 11 Tab.
2019. ISBN 978-3-96147-237-6.

Band 332: Eva Bogner
Strategien der Produktindividualisierung in der produzierenden Industrie im Kontext der Digitalisierung
FAPS, ix u. 201 Seiten, 55 Bilder, 28 Tab.
2019. ISBN 978-3-96147-246-8.

Band 333: Daniel Benjamin Krüger
Ein Ansatz zur CAD-integrierten muskuloskelettalen Analyse der Mensch-Maschine-Interaktion
KTmfk, x u. 217 Seiten, 102 Bilder, 7 Tab.
2019. ISBN 978-3-96147-250-5.

Band 334: Thomas Kuhn
Qualität und Zuverlässigkeit laserdirektstrukturierter mechatronisch integrierter Baugruppen (LDS-MID)
FAPS, ix u. 152 Seiten, 69 Bilder, 12 Tab.
2019. ISBN: 978-3-96147-252-9.

Band 335: Hans Fleischmann
Modellbasierte Zustands- und Prozessüberwachung auf Basis sozio-cyber-physischer Systeme
FAPS, xi u. 214 Seiten, 111 Bilder, 18 Tab.
2019. ISBN: 978-3-96147-256-7.

Band 336: Markus Michalski
Grundlegende Untersuchungen zum Prozess- und Werkstoffverhalten bei schwingungsüberlagerter Umformung
LFT, xii u. 197 Seiten, 93 Bilder, 11 Tab.
2019. ISBN: 978-3-96147-270-3.

Band 337: Markus Brandmeier
Ganzheitliches ontologiebasiertes Wissensmanagement im Umfeld der industriellen Produktion
FAPS, xi u. 255 Seiten, 77 Bilder, 33 Tab.
2020. ISBN: 978-3-96147-275-8.

Band 338: Stephan Purr
Datenerfassung für die Anwendung lernender Algorithmen bei der Herstellung von Blechformteilen
LFT, ix u. 165 Seiten, 48 Bilder, 4 Tab.
2020. ISBN: 978-3-96147-281-9.

Band 339: Christoph Kiener
Kaltfließpressen von gerad- und schrägverzahnten Zahnrädern
LFT, viii u. 151 Seiten, 81 Bilder, 3 Tab.
2020. ISBN 978-3-96147-287-1.

Band 340: Simon Spreng
Numerische, analytische und empirische Modellierung des Heißcrimpprozesses
FAPS, xix u. 204 Seiten, 91 Bilder, 27 Tab.
2020. ISBN 978-3-96147-293-2.

Band 341: Patrik Schwingenschlögl
Erarbeitung eines Prozessverständnisses zur Verbesserung der tribologischen Bedingungen beim Presshärten
LFT, x u. 177 Seiten, 81 Bilder, 8 Tab.
2020. ISBN 978-3-96147-297-0.

Band 342: Emanuela Affronti
Evaluation of failure behaviour of sheet metals
LFT, ix u. 136 Seiten, 57 Bilder, 20 Tab.
2020. ISBN 978-3-96147-303-8.

Band 343: Julia Degner
Grundlegende Untersuchungen zur Herstellung hochfester Aluminiumblechbauteile in einem kombinierten Umform- und Abschreckprozess
LFT, x u. 172 Seiten, 61 Bilder, 9 Tab.
2020. ISBN 978-3-96147-307-6.

Band 344: Maximilian Wagner
Automatische Bahnplanung für die Aufteilung von Prozessbewegungen in synchrone Werkstück- und Werkzeugbewegungen mittels Multi-Roboter-Systemen
FAPS, xxi u. 181 Seiten, 111 Bilder, 15 Tab.
2020. ISBN 978-3-96147-309-0.

Band 345: Stefan Härter
Qualifizierung des Montageprozesses hochminiaturisierter elektronischer Bauelemente
FAPS, ix u. 194 Seiten, 97 Bilder, 28 Tab.
2020. ISBN 978-3-96147-314-4.

Band 346: Toni Donhauser
Ressourcenorientierte Auftragsregelung in einer hybriden Produktion mittels betriebsbegleitender Simulation
FAPS, xix u. 242 Seiten, 97 Bilder, 17 Tab.
2020. ISBN 978-3-96147-316-8.

Band 347: Philipp Amend
Laserbasiertes Schmelzkleben von Thermoplasten mit Metallen
LPT, xv u. 154 Seiten, 67 Bilder.
2020. ISBN 978-3-96147-326-7.

Band 348: Matthias Ehlert
Simulationsunterstützte funktionale Grenzlagenabsicherung
KTmfk, xvi u. 300 Seiten, 101 Bilder,
73 Tab. 2020. ISBN 978-3-96147-328-1.

Band 349: Thomas Sander
Ein Beitrag zur Charakterisierung und Auslegung des Verbundes von Kunststoffsubstraten mit harten Dünnschichten
KTmfk, xiv u. 178 Seiten, 88 Bilder, 21 Tab. 2020. ISBN 978-3-96147-330-4.

Band 350: Florian Pilz
Fließpressen von Verzahnungselementen an Blechen
LFT, x u. 170 Seiten, 103Bilder, 4 Tab.
2020. ISBN 978-3-96147-332-8.

Band 351: Sebastian Josef Katona
Evaluation und Aufbereitung von Produktsimulationen mittels abweichungsbehafteter Geometriemodelle
KTmfk, ix u. 147 Seiten, 73 Bilder, 11 Tab.
2020. ISBN 978-3-96147-336-6.

Band 352: Jürgen Herrmann
Kumulatives Walzplattieren. Bewertung der Umformeigenschaften mehrlagiger Blechwerkstoffe der ausscheidungshärtbaren Legierung AA6014
LFT, x u. 157 Seiten, 64 Bilder, 5 Tab.
2020. ISBN 978-3-96147-344-1.

Band 353: Christof Küstner
Assistenzsystem zur Unterstützung der datengetriebenen Produktentwicklung
KTmfk, xii u. 219 Seiten, 63 Bilder, 14 Tab.
2020. ISBN 978-3-96147-348-9.

Band 354: Tobias Gläßel
Prozessketten zum Laserstrahlschweißen von flachleiterbasierten Formspulenwicklungen für automobile Traktionsantriebe
FAPS, xiv u. 206 Seiten, 89 Bilder, 11 Tab.
2020. ISBN 978-3-96147-356-4.

Band 355: Andreas Meinel
Experimentelle Untersuchung der Auswirkungen von Axialschwingungen auf Reibung und Verschleiß in Zylinderrollenlagern
KTmfk, xii u. 162 Seiten, 56 Bilder, 7 Tab.
2020. ISBN 978-3-96147-358-8.

Band 356: Hannah Riedle
Haptische, generische Modelle weicher anatomischer Strukturen für die chirurgische Simulation
FAPS, xxx u. 179 Seiten, 82 Bilder, 35 Tab.
2020. ISBN 978-3-96147-367-0.

Band 357: Maximilian Landgraf
Leistungselektronik für den Einsatz dielektrischer Elastomere in aktorischen, sensorischen und integrierten sensomotorischen Systemen
FAPS, xxiii u. 166 Seiten, 71 Bilder, 10 Tab.
2020. ISBN 978-3-96147-380-9.

Band 358: Alireza Esfandyari
Multi-Objective Process Optimization for Overpressure Reflow Soldering in Electronics Production
FAPS, xviii u. 175 Seiten, 57 Bilder, 23 Tab.
2020. ISBN 978-3-96147-382-3.

Band 359: Christian Sand
Prozessübergreifende Analyse komplexer Montageprozessketten mittels Data Mining
FAPS, XV u. 168 Seiten, 61 Bilder, 12 Tab. 2021. ISBN 978-3-96147-398-4.

Band 360: Ralf Merkl
Closed-Loop Control of a Storage-Supported Hybrid Compensation System for Improving the Power Quality in Medium Voltage Networks
FAPS, xxvii u. 200 Seiten, 102 Bilder, 2 Tab. 2021. ISBN 978-3-96147-402-8.

Band 361: Thomas Reitberger
Additive Fertigung polymerer optischer Wellenleiter im Aerosol-Jet-Verfahren
FAPS, xix u. 141 Seiten, 65 Bilder, 11 Tab. 2021. ISBN 978-3-96147-400-4.

Band 362: Marius Christian Fechter
Modellierung von Vorentwürfen in der virtuellen Realität mit natürlicher Fingerinteraktion
KTmfk, x u. 188 Seiten, 67 Bilder, 19 Tab. 2021. ISBN 978-3-96147-404-2.

Band 363: Franziska Neubauer
Oberflächenmodifizierung und Entwicklung einer Auswertemethodik zur Verschleißcharakterisierung im Presshärteprozess
LFT, ix u. 177 Seiten, 42 Bilder, 6 Tab. 2021. ISBN 978-3-96147-406-6.

Band 364: Eike Wolfram Schäffer
Web- und wissensbasierter Engineering-Konfigurator für roboterzentrierte Automatisierungslösungen
FAPS, xxiv u. 195 Seiten, 108 Bilder, 25 Tab. 2021. ISBN 978-3-96147-410-3.

Band 365: Daniel Gross
Untersuchungen zur kohlenstoffdioxidbasierten kryogenen Minimalmengenschmierung
REP, xii u. 184 Seiten, 56 Bilder, 18 Tab. 2021. ISBN 978-3-96147-412-7.

Band 366: Daniel Junker
Qualifizierung laser-additiv gefertigter Komponenten für den Einsatz im Werkzeugbau der Massivumformung
LFT, vii u. 142 Seiten, 62 Bilder, 5 Tab. 2021. ISBN 978-3-96147-416-5.

Band 367: Tallal Javied
Totally Integrated Ecology Management for Resource Efficient and Eco-Friendly Production
FAPS, xv u. 160 Seiten, 60 Bilder, 13 Tab. 2021. ISBN 978-3-96147-418-9.

Band 368: David Marco Hochrein
Wälzlager im Beschleunigungsfeld – Eine Analysestrategie zur Bestimmung des Reibungs-, Axialschub- und Temperaturverhaltens von Nadelkränzen –
KTmfk, xiii u. 279 Seiten, 108 Bilder, 39 Tab. 2021. ISBN 978-3-96147-420-2.

Band 369: Daniel Gräf
Funktionalisierung technischer Oberflächen mittels prozessüberwachter aerosolbasierter Drucktechnologie
FAPS, xxii u. 175 Seiten, 97 Bilder, 6 Tab.
2021. ISBN 978-3-96147-433-2.

Band 370: Andreas Gröschl
Hochfrequent fokusabstandsmodulierte Konfokalsensoren für die Nanokoordinatenmesstechnik
FMT, x u. 144 Seiten, 98 Bilder, 6 Tab.
2021. ISBN 978-3-96147-435-6.

Band 371: Johann Tüchsen
Konzeption, Entwicklung und Einführung des Assistenzsystems D-DAS für die Produktentwicklung elektrischer Motoren
KTmfk, xii u. 178 Seiten, 92 Bilder, 12 Tab.
2021. ISBN 978-3-96147-437-0.

Band 372: Max Marian
Numerische Auslegung von Oberflächenmikrotexturen für geschmierte tribologische Kontakte
KTmfk, xviii u. 276 Seiten, 85 Bilder, 45 Tab. 2021. ISBN 978-3-96147-439-4.

Band 373: Johannes Strauß
Die akustooptische Strahlformung in der Lasermaterialbearbeitung
LPT, xvi u. 113 Seiten, 48 Bilder.
2021. ISBN 978-3-96147-441-7.

Band 374: Martin Hohmann
Machine learning and hyper spectral imaging: Multi Spectral Endoscopy in the Gastro Intestinal Tract towards Hyper Spectral Endoscopy
LPT, x u. 137 Seiten, 62 Bilder, 29 Tab.
2021. ISBN 978-3-96147-445-5.

Band 375: Timo Kordaß
Lasergestütztes Verfahren zur selektiven Metallisierung von epoxidharzbasierten Duromeren zur Steigerung der Integrationsdichte für dreidimensionale mechatronische Package-Baugruppen
FAPS, xviii u. 198 Seiten, 92 Bilder, 24 Tab. 2021. ISBN 978-3-96147-443-1.

Band 376: Philipp Kestel
Assistenzsystem für den wissensbasierten Aufbau konstruktionsbegleitender Finite-Elemente-Analysen
KTmfk, xviii u. 209 Seiten, 57 Bilder, 17 Tab. 2021. ISBN 978-3-96147-457-8.

Band 377: Martin Lerchen
Messverfahren für die pulverbettbasierte additive Fertigung zur Sicherstellung der Konformität mit geometrischen Produktspezifikationen
FMT, x u. 150 Seiten, 60 Bilder, 9 Tab.
2021. ISBN 978-3- 96147-463-9.

Band 378: Michael Schneider
Inline-Prüfung der Permeabilität in weichmagnetischen Komponenten
FAPS, xxii u. 189 Seiten, 79 Bilder, 14 Tab.
2021. ISBN 978-3-96147-465-3.

Band 379: Tobias Sprügel

Sphärische Detektorflächen als Unterstützung der Produktentwicklung zur Datenanalyse im Rahmen des Digital Engineering

KTmfk, xiii u. 213 Seiten, 84 Bilder, 33 Tab. 2021. ISBN 978-3-96147-475-2.

Band 380: Tom Häfner

Multipulseffekte beim Mikro-Materialabtrag von Stahllegierungen mit Pikosekunden-Laserpulsen

LPT, xxviii u. 159 Seiten, 57 Bilder, 13 Tab. 2021. ISBN 978-3-96147-479-0.

Band 381: Björn Heling

Einsatz und Validierung virtueller Absicherungsmethoden für abweichungsbehaftete Mechanismen im Kontext des Robust Design

KTmfk, xi u. 169 Seiten, 63 Bilder, 27 Tab. 2021. ISBN 978-3-96147-487-5.

Band 382: Tobias Kolb

Laserstrahl-Schmelzen von Metallen mit einer Serienanlage – Prozesscharakterisierung und Erweiterung eines Überwachungssystems

LPT, xv u. 170 Seiten, 128 Bilder, 16 Tab. 2021. ISBN 978-3-96147-491-2.

Band 383: Mario Meinhardt

Widerstandselementschweißen mit gestauchten Hilfsfügeelementen - Umformtechnische Wirkzusammenhänge zur Beeinflussung der Verbindungsfestigkeit

LFT, xii u. 189 Seiten, 87 Bilder, 4 Tab. 2022. ISBN 978-3-96147-473-8.

Band 384: Felix Bauer

Ein Beitrag zur digitalen Auslegung von Fügeprozessen im Karosseriebau mit Fokus auf das Remote-Laserstrahlschweißen unter Einsatz flexibler Spanntechnik

LFT, xi u. 185 Seiten, 74 Bilder, 12 Tab. 2022. ISBN 978-3-96147-498-1.

Band 385: Jochen Zeitler

Konzeption eines rechnergestützten Konstruktionssystems für optomechatronische Baugruppen

FAPS, xix u. 172 Seiten, 88 Bilder, 11 Tab. 2022. ISBN 978-3-96147-499-8.

Band 386: Vincent Mann

Einfluss von Strahloszillation auf das Laserstrahlschweißen hochfester Stähle

LPT, xiii u. 172 Seiten, 103 Bilder, 18 Tab. 2022. ISBN 978-3-96147-503-2.

Band 387: Chen Chen

Skin-equivalent opto-/elastofluidic in-vitro microphysiological vascular models for translational studies of optical biopsies

LPT, xx u. 126 Seiten, 60 Bilder, 10 Tab. 2022. ISBN 978-3-96147-505-6.

Band 388: Stefan Stein

Laser drop on demand joining as bonding method for electronics assembly and packaging with high thermal requirements

LPT, x u. 112 Seiten, 54 Bilder, 10 Tab. 2022. ISBN 978-3-96147-507-0

Zusammenfassung

Im Rahmen dieser Arbeit wurde ein neuartiger Fügeprozess entwickelt und sowohl aus anwendungsorientierter als auch aus wissenschaftlicher Sicht untersucht. Bei diesem Verfahren wird mittels Laserstrahlung ein CuSn-Lötformteil aufgeschmolzen, und anschließend mittels Inertgasüberdruck aus einer keramischen Kapillare ausgetrieben. Nach einer Flugphase trifft der Löttropfen auf die Fügefläche und benetzt die Fügepartner, wo er nach der Erstarrung eine metallurgische Verbindung bildet. Dieser Prozess wird als Laser Drop on Demand Joining (LDJ) bezeichnet. Es konnte gezeigt werden, dass die Scherfestigkeit der Verbindungen die Festigkeit von Standardloten auf Zinnbasis um den Faktor zwei übersteigt und die erzeugte Verbindung zudem den Temperaturen und Scherkräften, die während des Al-Druckgussprozesses auftreten widersteht. Darüber hinaus ist durch die Messung des zum Aufschmelzen des Lotformteils notwendigen Zeitraums eine Quantifizierung des Absorptionsgrades von Metallen sowie von Energieverlusten durch Konvektion, Konduktion und Wärmestrahlung möglich.

In the scope of this work, a novel joining process was developed and investigated from both an application-driven and an academic point of view. The process utilises laser radiation to melt a CuSn-braze preform, which is subsequently detached from a ceramic capillary via inert gas overpressure. After a flight phase, the braze droplet impinges on the joining interface and wets the joining partners where it forms a metallurgical bond after solidification. This process is referred to as laser drop on demand joining (LDJ). It was shown that the shear strength of the joints exceeds the strength of standard tin-based solders by a factor of two and the joints are able to withstand the temperatures and forces occurring during an Al-Casting process. In addition, an analytic model was developed, enabling to quantify the absorptance and thermal energy losses by heat convection, conduction, and radiation, by measuring the time required to melt the preform.

ISBN 978-3-96147-507-0

FAU UNIVERSITY PRESS 2022